Investigating the Stoichiometry of RuBisCO Activase by Fluorescence Fluctuation Spectroscopy

by

Manas Chakraborty

A Dissertation Presented in Partial Fulfillment
of the Requirements for the Degree
Doctor of Philosophy

Approved April 2014 by the
Graduate Supervisory Committee:

Marcia Levitus, Chair
Charles Angell
Stuart Lindsay

ARIZONA STATE UNIVERSITY

May 2014

ABSTRACT

Ribulose-1, 5-bisphosphate carboxylase oxygenase, commonly known as RuBisCO, is an enzyme involved in carbon fixation in photosynthetic organisms. The enzyme is subject to a mechanism-based deactivation during its catalytic cycle. RuBisCO activase (Rca), an ancillary enzyme belonging to the AAA+ family of the ATP-ases, rescues RuBisCO by facilitating the removal of the tightly bound sugar phosphates from the active sites of RuBisCO. In this work, we investigated the ATP/ADP dependent oligomerization equilibrium of fluorescently tagged Rca for a wide range of concentrations using fluorescence correlation spectroscopy.

Results show that in the presence of ADP-Mg^{2+}, the oligomerization state of Rca gradually changes in steps of two subunits. The most probable association model supports the dissociation constants (K_d) of ~4, 1, 1 μM for the monomer-dimer, dimer-tetramer, and tetramer-hexamer equlibria, respectively. Rca continues to assemble at higher concentrations which are indicative of the formation of aggregates. In the presence of ATP-Mg^{2+}, a similar stepwise assembly is observed. However, at higher concentrations (30-75 μM), the average oligomeric size remains relatively unchanged around six subunits per oligomer. This is in sharp contrast with observations in ADP-Mg^{2+}, where a marked decrease in the diffusion coefficient of Rca was observed, consistent with the formation of aggregates. The estimated K_d values obtained from the analysis of the FCS decays were similar for the first steps of the assembly process in both ADP-Mg^{2+} and ATP-Mg^{2+}. However, the formation of the hexamer from the tetramer is much more favored in ATP-Mg^{2+}, as evidenced from 20 fold lower K_d associated with

this assembly step. This suggests that the formation of a hexameric ring in the presence of ATP-Mg^{2+}. In addition to that, Rca aggregation is largely suppressed in the presence of ATP-Mg^{2+}, as evidenced from the 1000 fold larger K_d value for the hexamer-24 mer association step.

In essence, a fluorescence-based method was developed to monitor *in vitro* protein oligomerization and was successfully applied with Rca. The results provide a strong hint at the active oligomeric structure of Rca, and this information will hopefully help the ongoing research on the mechanistic enzymology of Rca.

ACKNOWLEDGMENTS

I would like to thank my parents, and my siblings for their constant support. The only reason that I am here is because of all your care and well wishes.

I would like to thank all my teachers, for passing down their knowledge in educating me, and shaping my moral standards.

I would like to thank Prof. Marcia Levitus for giving me the opportunity to join her laboratory, providing financial support, and for her outstanding mentorship. Thank you very much Marcia for guiding me through the hurdles of graduate education. Many thanks to the past and present members of the group: Dr. Kaushik Gurunathan, Dr. Suman Ranjit, Jennifer Binder, Elana Stennet, Monika Ciuba, David Kanno, and Bryan Donaphon for being the coolest lab family. I will miss the cookie walks with Jennifer Binder, and lunch table conversations with the group.

It has been a pleasure to work in collaboration with Dr. Rebekka Wachter and her student Agnieszka Kuriata, and I would like to thank them for all their help. I wish all the luck for Andrew Serban who will be carrying the project forward.

I will thank my friends Souvik Roy, Dinesh Medpalli, and Basab Roy forever for being a like a family to me, because if it weren't for you, I would have hardly survived the grad school.

I would like to thank my committee members Dr. Charles Angell, and Dr. Stuart Lindsay for serving on my committee.

Lastly, I bow to *Devi Saraswati*, the Hindu goddess of learning, for gifting me with the ability to learn and educate others.

TABLE OF CONTENTS

Page

LIST OF TABLES

LIST OF FIGURES

Figure Page

CHAPTER 1

INTRODUCTION

1.1. Symmetry and Protein Function

The majority of soluble and membrane-bound proteins are known to form symmetrical homo-oligomers with two or more identical subunits. More than 80% of proteins found in *E. coli* are oligomeric, and among them 79% of proteins are composed of identical subunits; the remaining 21% are hetero-oligomers [1, 2]. The prevalence of symmetry among protein oligomers has its roots in the selection of a specific chirality of α-carbon in the amino acids over the other. The selection of *L* amino acids over *D* amino acids led to the formation of oligomeric proteins with enantiomorphic symmetry [1].

Evolution of protein function favored the formation of larger proteins with multiple functional sites over the smaller ones. Large oligomeric proteins gain extra stability against denaturation and have significantly less hydration volume compared to several small monomeric proteins. The reduction in the surface area of large proteins protects them against degradation. For example, insulin assumes a compact hexameric structure stabilized by the Zn^{2+} atom that protects it against degradation by proteolytic enzymes [3]. The formation of protein oligomers requires the formation of numerous weak bonding interactions (ΔH), which compensates for the reduction of the conformational freedom (ΔS) and stabilizes the protein against denaturation [4]. Oligomers also have multiple functional sites, which are required for the allosteric and cooperative functions of proteins [5, 6]. Larger proteins are also required for several morphological functions such as actin filaments, microtubules, or the viral hollow capsids - they are much easier

to build from small identical building blocks then to make a large monomeric unit [1]. The cellular protein-making machinery typically makes proteins in the range 30,000-50,000 Daltons [7], which reflects a delicate balance between the need for large proteins and the limit on the size of the polypeptide chains that can be synthesized to reduce translational errors.

Missense errors occur with a frequency of $5*10^{-4}$ per codon [8, 9], hence a protein with nearly 2000 amino acids nearly always has an error. In addition to that, the processivity error occurs at a frequency of $3*10^{-4}$ per codon [8, 9] implies that a protein with 3000 amino acid residues will seldom be translated in full. It is also easy to make multiple copies of the same protein which can be assembled in a much more regulatory way, and this mechanism saves a lot of genetic space [1, 10]. However, the presence of non-coding DNAs argues against this being a significant reason [11]. It is also easy to regulate the assembly and create different patterns as required by the function, such as the case with actin filaments and microtubules [12-14]. For these reasons, homo-oligomers are more abundant then hetero-oligomers and they display a plethora of symmetrical structures.

Oligomers assume symmetrical structures in order to achieve a finite assembly and avoid aggregation. [1] Building a symmetrical structure also maximizes inter-subunit interactions, and it is proposed that symmetrical proteins fold with fewer kinetic barriers [11]. Depending on function, the oligomeric structure of a protein can adopt a specific symmetry group. For example, directionality in protein function would require the formation of rings, tubular structures with cyclic symmetry [1]. Allosteric control of protein functions would be facilitated by more inter-subunit interaction sites, and thus

dihedral symmetry is the choice for these classes of proteins [1, 5, 6]. Cubic symmetries are frequently observed for storage and transport proteins [10, 15] such as viral capsids with icosahedral symmetry. There is also a fourth kind of unbound symmetry observed among structural proteins like the bacterial flagella with helical symmetry [16], and collagen that forms a 3D lattice [17].

1.2. AAA+ ATP-ases

AAA+ ATP-ases are a functionally diverse group of proteins which are known to form symmetrical homo-oligomers [18-20]. The functional oligomers of this group mostly assume cyclic symmetry and most commonly have a hexameric form with C_6 symmetry [18, 21]. In a cyclic arrangement, the active sites are placed at the interfaces of adjacent subunits in the holoenzyme, and the presence of a central hole allows substrate manipulation [18]. The AAA+ ATP-ases convert chemical energy from the hydrolysis of ATP into conformational changes in its structure, which in turn is translated into its substrate proteins as functional work [18, 22, 23].

The general structure of this family of proteins contains a structurally conserved AAA+ domain shown in fig. 1.2.1. [20] Based on the published crystal structures, this domain consist of an N-terminal α, β-Rossman fold, and a C-terminal α helical sub-domain [20]. The AAA+ domain is connected to other domains of the proteins by the N-linker (fig. 1.2.1 A). The N-linker is flexible and is thought to transmit the nucleotide-dependent conformational change of the AAA+ domain to other parts of the protein [24]. The walker B and A motifs are integral to the nucleotide binding site [19]; the conserved p-loop (between β1 and α1) interacts with the phosphates of ATP. The highly conserved

lys (K) reside in the sequence GXXXXGKT/S (where X is any amino acid residue) plays a crucial role in the binding and the hydrolysis of ATP [18]. Mutation of this residue hampers ATP binding and hydrolysis. The acidic residues of hhhhDE (h is any hydrophobic amino acid) in the Walker B motif (the loop between β3 to the start of α3) are central to the ATP-ase activity [18]. The aspartate residue is known to coordinate with Mg^{2+} required for ATP hydrolysis, while the glutamate residue activates water for hydrolysis [18, 20]. Mutation of these residues results in the loss of ATP-ase activity, and can also be utilized to produce substrate traps which can bind but cannot release the substrate [25]. The second region of homology, SRH, (part of β4, α4, and loop to β5) contains two specific structural motifs, sensor 1 and sensor 2.

There is a conserved arg residue in the sensor 1 module which is proposed to coordinate nucleotide hydrolysis and conformational change between subunits [26]. This effect is known as the arginine finger effect [18]. There are two arginine fingers on either side of the SRH; one is found between the loop connecting β4 to α4, and the other is placed in the loop between α4 to β5. In an oligomeric protein, the arginine fingers from one subunit constitute part of the nucleotide binding site of an adjacent subunit. They are known to interact with the γ-phosphate of ATP [26]. The conserved arg residue found in the sensor 2 module (α7) near the C-terminal end also takes part in nucleotide binding through the γ-phosphate of ATP. Mutation of these residues hampers proper function of the protein without compromising their ability to form oligomers [27].

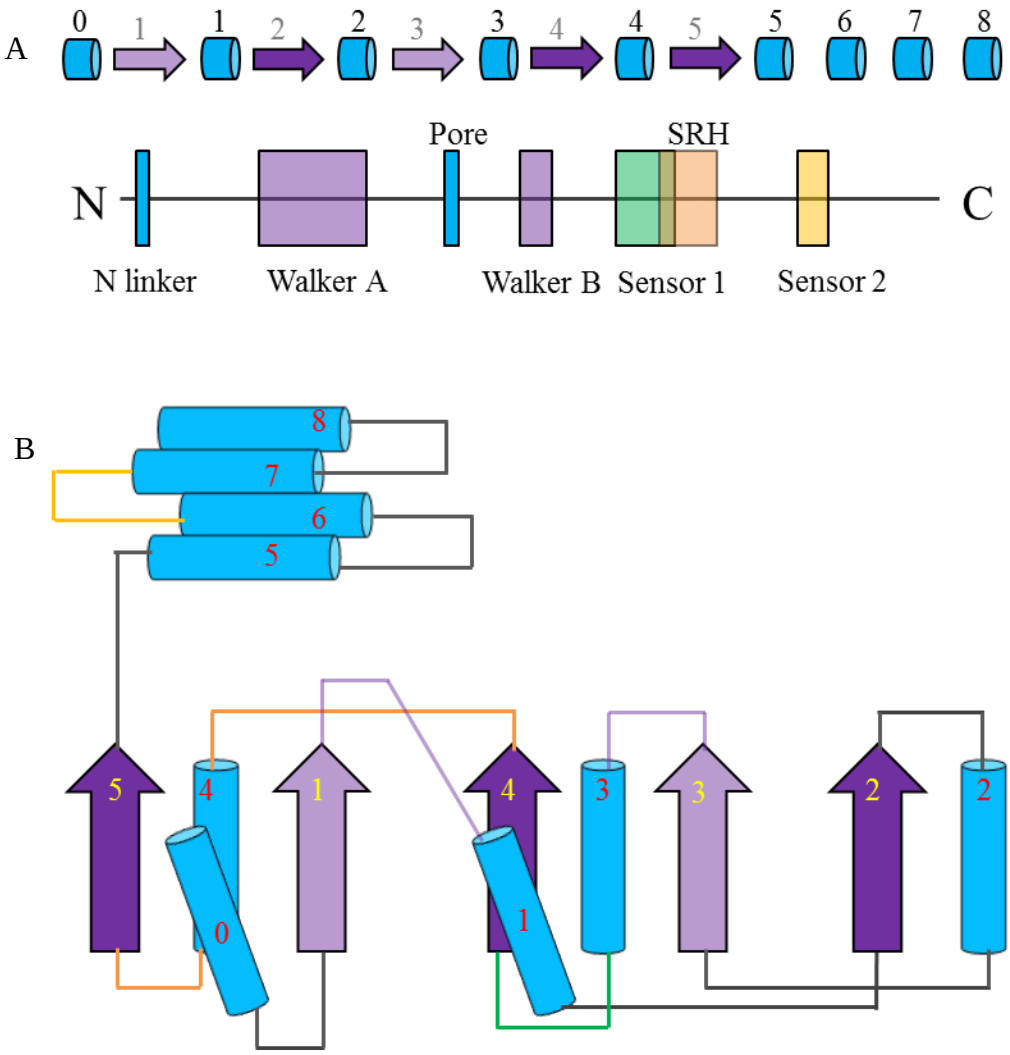

Figure 1.2.1. The General Structure of the AAA+ ATP-ase Domain. A) Linear structure of the AAA+ domain; the α-helices and the β-sheets are represented by the blue cylinders and the purple arrows, respectively. Approximate positions of different structural motifs such as the N-linker, Walker A & B, pore regions, SRH, and sensors 1 and 2 are shown below the linear diagram. B) A general topological diagram of the AAA+ domain. The color scheme is consistent with the linear representation in A). The color of the loops between the α-helices and the β-sheets is consistent with the color of the highlighted domains of the lower panel in part A. The numbering of the structural elements in this figure is done according to ref. [20].

1.3. RuBisCO and RuBisCO Activase

RuBisCO activase, the catalytic chaperone of RuBisCO, belongs to the family of AAA+ ATP-ases [28]. Ribulose-1,5-bisphosphate carboxylase/oxygenase (RuBisCO enzyme) catalyzes the biological carbon assimilation reaction in green plants and photosynthetic organisms [29]. In this reaction, one molecule of a 5-C compound Ribulose 1,5-bisphosphate carboxylase/oxygenase (RuBP) reacts with CO_2 and produces two molecules of a 3-C compound, namely 3-phosphoglycerare (3-PG) [30, 31]. This reaction is the rate-limiting step of the Calvin cycle, therefore slowing photosynthesis. RuBisCO is a complex protein consisting of eight large subunits (~55 kDa) and eight small (~13 kDa) subunits [32]. The active sites of RuBisCO are located within the interface between the large subunits [32].

Catalytically active RuBisCO adopts an open conformation in which these active sites remain accessible to solvent so that it can bind to RuBP. The binding of RuBP must be preceded by the carbamylation of these active sites [33]. After that, the RuBisCO switches to a closed conformation and the solvent accessibility to its substrate-bound active sites becomes restricted. However, if the substrate RuBP binds to the non-carbamylated active sites, it results in the formation of deadlock complexes in which the active sites are closed and are no longer accessible for the solvent [34]. Additionally, due to poor substrate specificity of RuBisCO activase, its active sites are frequently populated by the other inhibitory sugar phosphates such as XuBP, CA1P which results in the formation of inactive RuBisCO complexes [34-37].

In order to overcome this catalytic incompetence, plants tend to express RuBisCO in very high levels, making it the most abundant protein on the Earth [38]. An alternative

mechanism of rescuing inactive RuBisCO complexes has also evolved, and RuBisCO activase was identified as a helper enzyme that rescues deadlock RuBisCO complexes by releasing the inhibitory sugar phosphates from its active site [39]. RuBisCO activase was first identified in the plant *Arabidposis Thaliana*, where it was found to release the inhibition from RuBisCO in an ATP-dependent mechanism [19, 39-43].

Soon after its discovery, numerous research efforts were carried out on the structure and function of Rca. Much of the Rca research is aimed at investigating the potential connection between the thermolability of Rca and the inhibition of photosynthesis at moderate heat stress [44-46]. A recently published crystal structure of Rca from *N. Tabacum* reveals its structure typical to the family of AAA+ATP-ases [47]. It has an N-terminal substrate recognition domain, a central AAA+ module, and a C-terminal regulatory domain. Truncation of the N-terminal domain or mutation of the highly conserved trp residue in this domain abolishes RuBisCO reactivation without affecting the ATP hydrolysis ability of Rca [48, 49]. The AAA+ module is highly conserved; there is ~58% sequence similarity from plants and green algae of the genus *ostreococcus* [32].

Even so, the organization of Rca subunits in solution is not adequately characterized. Biochemical studies show that Rca forms a highly polydisperse solution with oligomers of sizes between 50 and 600 kDa observed, depending on the concentration and buffer condition [50, 51]. A functionally impaired Rca mutant R294A [52] was discovered to form stable 300 kDa hexamers in the presence of a non-hydrolysable ATP analogue, ATP-γ-S [53]. Results from negative stain EM experiments show the same Rca mutant R294A forms complexes of six-fold symmetry in the presence of ATP or ATP-γ-S [47]. There is a positive correlation between the ATP-ase activity and the RuBisCO

reactivation activity, which indicates the connection between its oligomeric state and RuBisCO reactivation activity [47, 51, 54]. However, *in vitro* Rca does not require activation by the substrate to hydrolyze ATP [41]. The ATP-ase activity of spinach Rca was found to increase with the concentration of Rca, with a maximum turnover rate predicted beyond 1 μM [51]. The maximum activity of a Ribulose-P2 bound RuBisCO substrate reactivation by Rca was also found to lie above 1 μM Rca [54].

Studies done with a mixture of wild type and mutant Rca provided evidence that oligomers beyond a hexamer may not be required for RuBisCO reactivation [47]. The central pore of the hexameric complex is ~36 Å wide [47], which suggests extensive interaction involving multiple motifs of the substrate RuBisCO. The role of nucleotides (ATP/ADP) in connection with Rca regulation also remains unclear. It has been shown that high ADP levels downregulate Rca activity in a redox-dependent manner [32]. In plants such as *A. Thaliana* and *O. Sativa,* two isoforms of Rca are expressed, a 42 kDa short isoform and a 46 kDa large isoform. The large isoform has a longer C-terminal extension and is redox regulated by disulfide bond formation in its C-terminal tail. This makes the large isoform susceptible to regulation by ADP [32].

The transient intermediates formed during the assembly of Rca to its active structure are not properly characterized. Whether the assembly pathway of Rca happens through stepwise addition of monomeric subunits or if it involves dimers, trimers, tetramers, etc., and how the proportions of oligomers change in a concentration dependent manner poses a critical research question that needs to be addressed in order to understand the role of Rca in RuBisCO reactivation. At the same time, how this association pathway is

modified by the relative concentration of ATP/ADP would help to understand the regulation of Rca between the light and the dark phases of photosynthesis.

Standard biochemical methods to identify protein oligomers of different sizes such as size exclusion HPLC (SE-HPLC), analytical ultracentrifugation (AUC), and gel electrophoresis methods are extensively used to study quaternary structures of proteins and protein aggregation. However, non-ideal interactions between the protein and the column material for SE-HPLC have been routinely observed [55]. Also, the methods such as AUC and gel electrophoresis rely upon separation of oligomers based on external forces such as gravitation and electric field, and they do not always permit studies under equilibrium conditions. Approaches using SE-HPLC to study Rca oligomerization showed a broad distribution characteristic of a highly polydisperse solution, and with an estimated error of 20-30% (unpublished results). Results obtained from AUC experiments were difficult to fit to a specific model due to the presence of several oligomeric states (unpublished results); several models fit equally well, and distinction among different models is beyond possible.

In the present work, we used a non-invasive fluorescence fluctuation based technique to monitor Rca self-association, and we devised mathematical association models to interpret the data. We investigated the self-association of Rca in a concentration-dependent manner, and we also investigated the role of ATP/ADP in changing the course of association. We are also able to predict the plausible assembly model and estimate relevant thermodynamic constants such as the dissociation coefficients of different oligoemric states. Our results indicate that Rca assembles in steps involving multiple intermediates, and the oligomeric proportions are influenced by the relative concentration

of ATP/ADP in the experimental buffer. Specifically, our data suggest that in presence of 4 mM ADP, Rca predominantly forms aggregates at concentrations above 60 μM, whereas ATP stabilizes oligomers roughly constituting six subunits at 30-75 μM concentration range.

1.4 Fluorescence Correlation Spectroscopy

Fluorescence correlation spectroscopy is a widely used technique to study transport properties of biomolecules diffusing freely in a solution. It is based on correlating spontaneous fluctuations in the fluorescence signal given out by fluorescently tagged molecules. The method was introduced by Magde, Elson, and Webb in the 1970s as a special case of relaxation analysis [56-58]. In theory, any physical processes that give rise to a fluctuation in the fluorescence signal can be accessible by FCS. This method is very well suited for spatio-temporal analysis of low concentrations of biomolecules.

The ultra-high sensitivity of the technique relies on a very small observation volume that is created using a combination of a laser beam tightly focused by a high numerical aperture objective and a micrometer-sized pinhole to reject out of focus light [59, 60]. For one photon excitation, the volume can be approximated by a 3D-Gaussian point spread function [60]. Fluctuations in fluorescence occur as molecules diffuse through the inhomogeneous volume of illumination due to Brownian motion. Fluctuations can also occur if a molecule undergoes any physical or chemical process that can change its fluorescence quantum yield. A temporal correlation of these fluctuations is the ultimate readout of FCS instrument. Hence, an FCS curve would contain information

about all the chemo-physical processes that contributed to fluctuation in the fluorescence signal [61]. Since its inception, FCS has been successfully used to measure conformational dynamics [62, 63], transport properties in vitro and vivo [64-68], and protein oligomerization [69, 70].

One particular application of FCS is studying biomolecular assembly and interactions [71-73]. Such interactions are behind most complex biological functions. The functional form of many proteins is found to be oligomers, and hence the knowledge of the oligomeric state of the protein holds the key to understanding its function. According to the Stokes-Einstein equation (eq. 1.4.1), the diffusion coefficient of any particle is inversely related to its radius of gyration.

$$D = \frac{kT}{6\pi\eta R_{gyr}} \qquad \text{Eq. 1.4.1}$$

Here, kT is the thermal energy, η is the viscosity of the solvent, and R_{gyr} is the radius of gyration of the protein.

Therefore, protein oligomerization can be monitored by measuring the change in its diffusion coefficient, obtained from the measured FCS curve of any fluorescently tagged protein solution. However, most common proteins display a wide range of binding constants, starting from low nM to very high μM concentrations. In other words, a detailed characterization of protein oligomerization would also require conducting experiments at high concentrations. The sensitivity of the FCS technique relies on the fluorescence signal, which is inversely proportional to the concentration of the fluorescently labeled particles (fluctuation $\propto 1/\sqrt{N}$). This imposes an upper limit on the concentration of the fluorescently labeled particles that can be studied using FCS.

Nevertheless, higher concentrations can be accessed by mixing labeled and unlabeled protein while keeping the concentration of the labeled protein at constant low nM concentration. More information regarding this strategy of mixing will be provided later in the results chapter.

FCS Principle: Instrumentation

Fluorescence fluctuation measurements are done using a single molecule confocal setup and carried out in a solution of fluorescently labeled particles. A schematic diagram of the single molecule confocal setup used for collecting FCS data is shown in fig. 1.4.1. In this diagram, an excitation laser beam is tightly focused onto the sample using a high numerical aperture (N.A.) objective. The same objective is used to collect the fluorescence signal upon excitation and is passed on for detection. A dichroic filter in the detection path separates the excitation laser from the fluorescence, and a small 50 μm pinhole is used to reject the out of focus light. The combination of the objective lens and the pinhole restrict the observation volume to the low fL range, and is typically ~3 fL. For one photon excitation, the three dimensional shape of the excitation volume also known as confocal volume can be well approximated by a Gaussian point spread function (eq. 1.4.2) which has the maximum excitation intensity at the center of the volume, and the intensity falls off as the exponential of the square of the distance from the center at any direction.

$$3DG = \left(\frac{1}{2\pi}\right)^{3/2} e^{-2\left(\frac{x^2+y^2}{{r_0}^2}\right)} e^{-2\left(\frac{z^2}{{z_0}^2}\right)} \qquad \text{Eq. 1.4.2}$$

This inhomogeneity in the confocal volume, together with the fluctuation in the number of fluorescent molecules in the confocal volume, gives rise to the fluctuation in the fluorescence signal. The fluorescence signal after the pinhole is subjected to further filtering from background light, before being detected by the avalanche photodiode (point) detectors (APD). These detectors signal the arrival of each single photon and send an amplified electrical signal to the hardware correlator. The hardware correlator then correlates the signals in real time to produce a fluorescence correlation plot. A detail of the instrumentation can be found in the materials and the methods section (Chapter 2). A fluorescence correlation set-up can have multiple detection channels for measurements with more than one type of fluorophores. This allows the calculation of multiple fluorescence correlation curves, as well as cross correlation curves between two independent detectors.

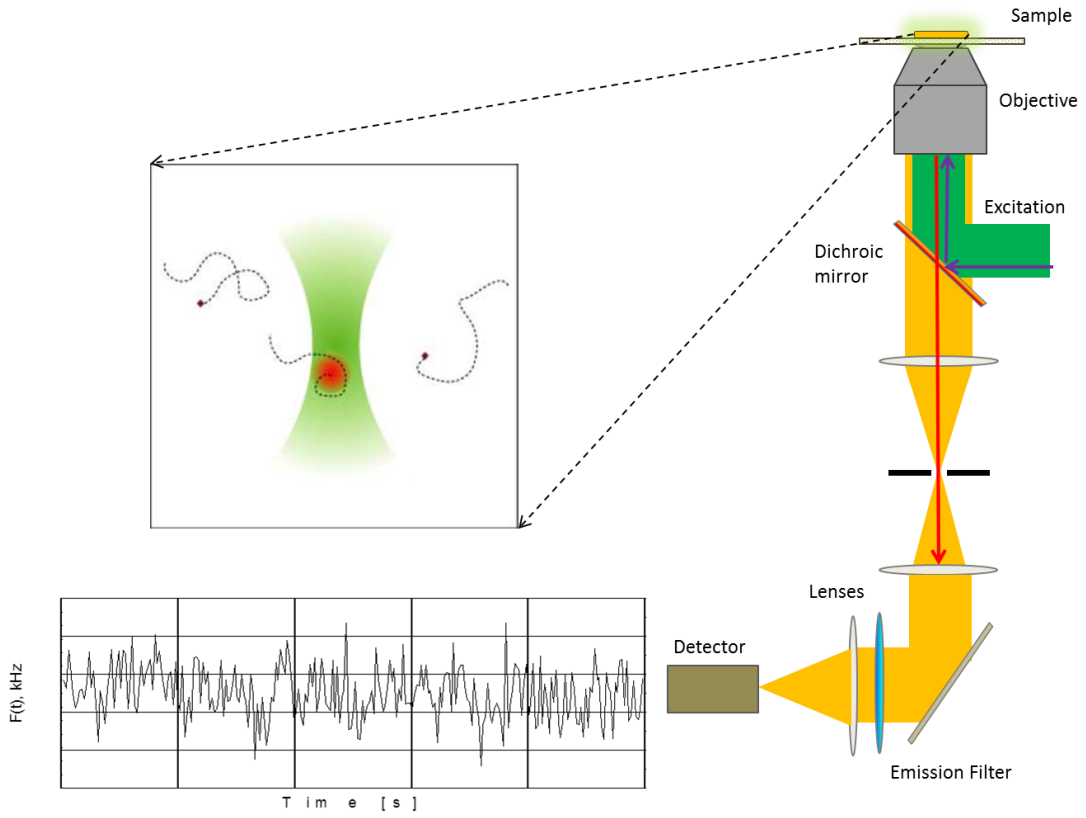

Figure 1.4.1. Schematic Representation of the FCS Setup. (A) The laser and different optical components are labeled in the diagram. (B) A cartoon representation of the excitation volume (~3 fL) is shown as a zoomed-in image. (C) The raw fluorescence fluctuation signals from a freely diffusing TAMRA dye.

FCS Principle: Autocorrelation Analysis

In this method, the recorded fluorescence intensity from a single detector is correlated in time. This is a measure of the similarity between the fluorescence intensities as a function of different lag times and contains specific information regarding time constants of the underlying processes responsible for fluctuation in the signal. Let us consider a simple case of diffusion of fluorescently labeled particles moving in and out of the confocal volume as a result of Brownian motion. In this case, the fluctuation in fluorescence intensity arises due to concentration fluctuation and due to inhomogeneous nature of the illumination profile. These fluctuations can be defined as the deviations of the fluorescence signal from the mean fluorescence intensity. They can be described by eq. 1.4.3.

$$\delta I(t) = I(t) - \langle I(t) \rangle \qquad \text{Eq. 1.4.3}$$

Here, $I(t)$ is the momentary fluorescence intensity at time t and $\langle I(t) \rangle$ is the mean fluorescence intensity. A typical recorded fluorescence intensity trace is shown in fig. 1.4.2.

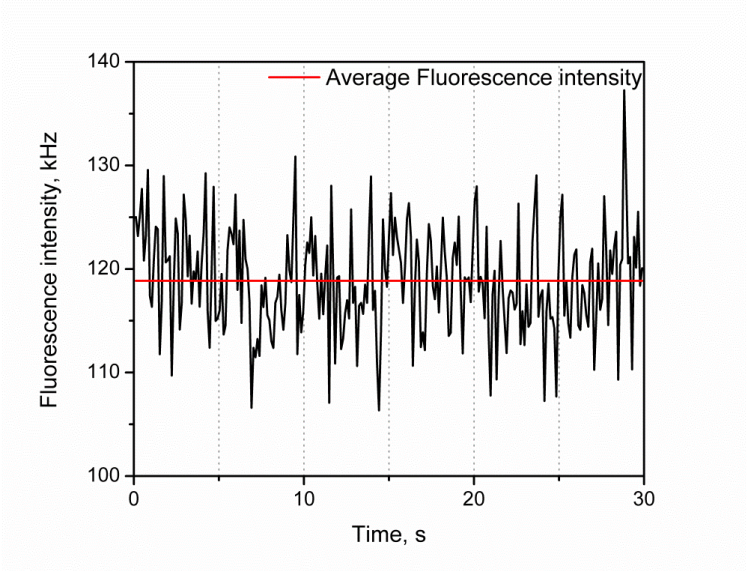

Figure 1.4.2. Fluorescence Intensity Trace. Fluorescence intensity trace recorded as a function of time. The red line represents the mean fluorescence intensity,$\langle I(t)\rangle$. The mean fluorescence intensity is represented as the red line in the plot.

In autocorrelation analysis, the fluorescence intensity recorded in one detector is compared with the same recorded data but shifted by a lag time, τ. The fluorescence autocorrelation function is calculated using eq. 1.4.4.

$$G = \frac{\langle \delta I(t) * \delta I(t+\tau) \rangle}{\langle I(t) \rangle^2} \qquad \text{Eq. 1.4.4}$$

In the equation 1.4.4, the auto correlation function is normalized by the square of the mean intensity. According to this equation, if $\tau \to 0$, G assumes a large value; conversely, when τ grows large, $G \to 0$. In other words, adjacent observations are similar to each other, while the similarity goes down as the observations become more distant in time. For the present case, all of the fluctuations arise from the changes in the local concentration of a single type of fluorescent particle and the analytical solution for equation 1.4.4 is given by equation 1.4.5.

$$G = G(0)\left(1 + \frac{4D\tau}{r_0^2}\right)^{-1}\left(1 + \frac{4D\tau}{{z_0}^2}\right)^{-\frac{1}{2}} = G(0)\left(1 + \frac{\tau}{\tau_D}\right)^{-1}\left(1 + \frac{\tau}{s^2\tau_D}\right)^{-\frac{1}{2}} \quad \text{Eq. 1.4.5}$$

Here, $(0) = \frac{1}{\langle N \rangle}$ is the mean amplitude of the FCS curve and is given by the reciprocal of the mean number of particles ($\langle N \rangle$) inside the confocal volume, r_0, z_0 are the radial and the axial axes of the confocal volume, and D is the diffusion coefficient of the particle. $\tau_D = r_0^2/4D$ is the diffusion time, and $s = z_0/r_0$ is defined as the shape factor of the confocal volume.

Equation 1.4.3 is used to fit experimentally obtained FCS curves to calculate the diffusion coefficient (D) or the diffusion time (τ_D) of particles in a mono-disperse solution. A representative fit for TAMRA dye is shown in Fig. 1.4.3. The confocal volume (V_{conf}) comes from an integration of the 3D-Gaussian equation (eq. 1.4.2) and is given by equation 1.4.6.

$$V_{conf} = \left(\frac{\pi}{2}\right)^{\frac{3}{2}} r_0^2 z_0 \quad \text{Eq. 1.4.6}$$

The PSF volume can also be calculated from the auto correlation amplitude ($G(0)$) and the concentration (C) of the particles using eq. 1.4.7.

$$V_{conf} = \frac{1}{G(0)N_A C} \quad \text{Eq. 1.4.7}$$

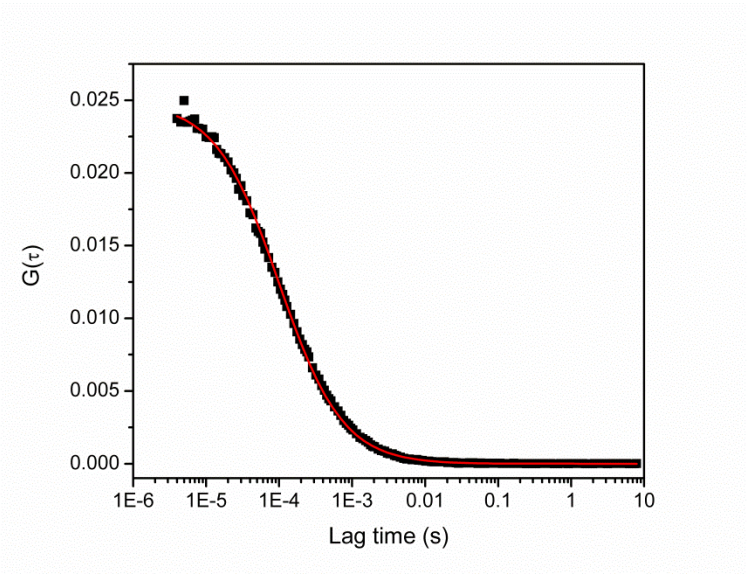

Figure 1.4.3. TMR Auto Correlation Curve: Experimental autocorrelation curve (black scatter) of freely diffusing tetramethyl rhodamine (TMR) in water, and fit (*red line*) according to eq. 1.4.3. The data is fitted with a fixed diffusion coefficient for TMR dye (D = 420 μ^2/s), and fixed axial parameter (z_0 = 10 μm) while optimizing for the radial volume parameter (r_0), and the amplitude ($G(0)$).

The auto-correlation function for n different non-interacting fluorescent species with well-defined diffusion coefficients (D_i) and brightness (ε_i) can be written as equation 1.4.8.

$$G(\tau) = \frac{2^{-3/2}\sum_i^n N_i \varepsilon_i^2 g_i(\tau)}{\left(\sum_{i=1}^n N_i \varepsilon_i\right)^2} \qquad \text{Eq. 1.4.8}$$

Where,

$$g_i = \left(1 + \frac{4D\tau}{r_0^2}\right)^{-1}\left(1 + \frac{4D\tau}{z_0}\right)^{-\frac{1}{2}} \qquad \text{Eq. 1.4.9}$$

Note that in Eq. 1.4.8, individual contributions to the total autocorrelation function from different species in a mixture of species are weighted by the square of their brightness (ε). The brightness term is defined as the photon counts per second per molecule (cpsm). The molecular brightness depends on the properties of the fluorophores such as the

fluorescence quantum yield and other instrumental parameters such as the excitation laser power. It varies among different dyes due to a change in the fluorescence quantum yield and for interacting particles such as fluorescently labeled protein subunits. For example, consider a case of protein oligomerization equilibria involving monomers and dimers in which each protein subunit has been carefully labeled with only one fluorescent tag for FCS measurements. In this case, the dimers will contribute four times as the monomer to the total auto correlation function simply because there are two labeled subunits in a dimeric molecule. This phenomenon of changing brightness upon oligomerization has been nicely utilized in determining the size of a protein oligomer using photon counting histogram (PCH) as explained in the next section.

The sensitivity of the FCS technique to changes in the diffusion coefficient of the fluorescent particles makes it very useful to monitor bio-molecular association processes such as protein oligomerization. One of the methods for labeling protein subunits is to fluorescently tag with organic fluorophores through chemical modification of the solvent exposed cysteine residue [74] on the surface of the protein molecules. The self-association of this protein in solution can then be studied by following the shift in the measured auto correlation curves toward higher time scales as a result of the formation of slower diffusing heavier oligomers, as illustrated in fig. 1.4.4.

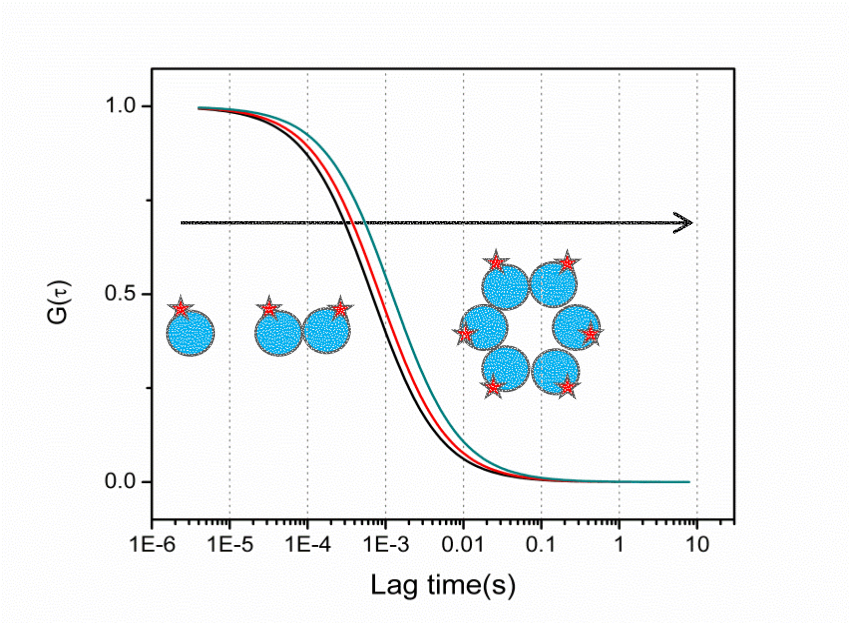

Figure. 1.4.4. Cartoon Representation of Protein Self-Association. Self-association of protein subunits (blue spheres with a red star representing a fluorescent marker), and concomitant shift in the FCS curves toward higher time scales.

1.5 Photon Counting Histogram

PCH provides an alternative way of analyzing fluorescence fluctuations. The difference between FCS and PCH is that the first one depends on the duration of fluctuation and depends less on excitation laser power, while PCH depends on the amplitude of intensity distribution and it independent of time. In practice, the same raw fluorescence data used for calculating FCS can be used to obtain a probability distribution of fluorescence intensities as a function of photon counts. The method was introduced by Chen, Mueller and Gratton in 1999 [75] and Zare [76] at the same time. In theory, the photon counting statistics of identical but independent fluorescently labeled particles depend on two parameters, the number of molecules and the molecular brightness expressed in counts per second per molecule (cpsm) [75]. The average number

of molecules can be obtained from the FCS auto correlation amplitude (eq.1.4.5) and used as a known parameter in the analysis of PCH data. This means PCH offers a way to accurately estimate the molecular brightness of fluorescent particles. Therefore, PCH can distinguish between the particles with the same diffusion coefficient but with different brightness values. The molecular brightness of a biomolecule depends on the number of fluorescent labels per molecule as well as the optical properties of the PCH instrumentation. In other words, at a constant laser power and using identical fluorophores, the molecular brightness of an oligomeric protein that contains one label per subunit and constituting of n subunits will be n-times the brightness of its monomer. Hence, PCH is successfully applied to the study of biomolecular assembly or interaction processes which is accompanied by a change in molecular brightness [77]. A representation of PCH histograms is given in figure 1.5.1.

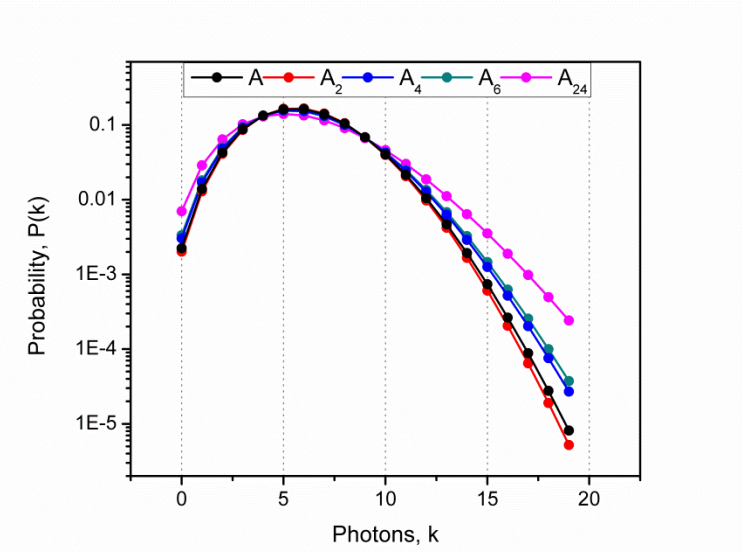

Figure 1.5.1. Theoretical PCH Histograms for Protein Oligomers. Oligomers of different sizes as indicated in the figure legend.

Theory of PCH

The instrumentation for the collection of PCH data is the same as the FCS instrument. The theory of the PCH histograms can be described in steps of a single diffusing particle in a closed volume, to a number of particles in the same volume, and finally a general scenario in an open volume, where the fluctuation in the number of the particles obey the poissonian statistics. Since a point detector in used for collecting the photon data, and since the detector adds shot noise to the data, we must consider the photon detection statistics by the detector. A detector shot noise follows a Poisson distribution even for a light of constant intensity (eq. 1.5.1), and the photon counting statistics, given by Mandel's formula [78] equation 1.5.2.

$$Poi(k,\langle k\rangle) = \frac{(\eta_W W)^k e^{-\eta_W W}}{k!} \qquad \text{Eq. 1.5.1}$$

$$p(k,t,T) = \int_0^\infty \frac{\left(\eta_W W(t)\right)^k e^{-\eta_W W(t)}}{k!} p(W(t))dW(t) \qquad \text{Eq. 1.5.2}$$

Here, $p(k,t,T)$ is the probability of detecting k photoelectron events at time t. The integration time is given by T, η_W is the detector efficiency, and $W(t)$ (eq. 1.5.3) is the integration of the light intensity falling on the detector area A over the time period T.

$$W(t) = \int_t^T \int_A I(r,t)dAdt \qquad \text{Eq. 1.5.3}$$

For a poissonian distribution, the variance $\langle \Delta k^2 \rangle$ is equal to the mean $\langle k \rangle$. Any additional fluctuation will result in a change it the photon counting statistics and will broaden the distribution. This is why the photon counting distribution from fluctuating fluorescence signals are always super poissionian, *i.e.* $\langle \Delta k^2 \rangle$ is greater than the mean $\langle k \rangle$. The photon counting statistics from the fluctuating signal is obtained by replacing W with the intensity I_D in eq. 1.5.2, and is given by eq. 1.5.4.

$$p(k) = \int_0^\infty \frac{(\eta_I I_D)^k e^{-\eta_I I_D}}{k!} p(I_D) dI_D \quad \text{Eq. 1.5.4}$$

This can be done by considering that the intensity I remains constant over the small detector area A, and with a short sampling time, $T = \Delta t$.

Now, considering a 3D-Gaussian (eq. 1.4.2) PSF for a one photon excitation process, we can write the fluorescence intensity I_D at the detector from a fluorophore at position r_0 within the PSF as eq. 1.5.5

$$I_D = I_0^n \beta \overline{PSF}(\vec{r_0}) \quad \text{Eq. 1.5.5}$$

With n = 1 for one photon excitation, I_0 is the excitation intensity, β contains the fluorophore properties such as the absorption cross section, quantum yield, and the instrument parameters. Applying the transformation property of probabilities we can write the probability $p(I_D)$ as,

$$p(I_D) = \int \delta\left(I_D - I_0^n \beta \overline{PSF}(\vec{r_0})\right) p(\vec{r}) dr \quad \text{Eq. 1.5.6}$$

$$\text{Where, } p(\vec{r}) = \begin{cases} \frac{1}{V_0} \; for \; \underset{r}{\rightarrow} \in V_0 \\ 0 \; for \; \underset{r}{\rightarrow} \notin V_0 \end{cases} \quad \text{Eq. 1.5.7}$$

A substitution of $p(I_D)$ from eq. 1.5.6 into eq. 1.5.4 yields

$$p^{(1)}(k; V_0, \varepsilon) = \int_{V_0} \left(Poi(k, \varepsilon \overline{PSF}(\vec{r}))\right) dr \quad \text{Eq. 1.5.8}$$

This the fundamental equation of PCH for a single particle, and where the brightness ε is given by, $\varepsilon = I_0^n \beta \eta_I$. Considering 3D-Gaussian PSF in the eq. 1.5.8 one obtains the PCH for one particle in a closed volume V_0

$$p^{(1)}{}_{3DG}(k; V_0, \varepsilon) = \frac{1}{V_0} \frac{\pi \omega_0^2 z_0}{k1} \int_0^\infty \gamma\left(k, \varepsilon e^{-2x^2}\right) dx, \;\; for \; k > 0 \quad \text{Eq. 1.5.9}$$

The normalization condition gives the value of $k = 0$, and it is given by

$$p^{(1)}{}_{3DG}(0; V_0, \varepsilon) = 1 - \sum_{k=1}^\infty p^{(1)}{}_{3DG}(k; V_0, \varepsilon) \quad \text{Eq. 1.5.10}$$

The PCH for N identical particle in the same closed volume is a convolution of the individual one particle PCH's as expressed as

$$p^{(N)}{}_{3DG}(k;V_0,\varepsilon) = (p^{(1)} \otimes \dots N\ times \dots \otimes p^{(1)})(k;V_0,\varepsilon) \quad \text{Eq. 1.5.11}$$

Finally, the PCH for an open system where the particles are entering and leaving the observation volume is obtained by averaging individual probability functions for N particles $p^{(N)}{}_{3DG}(k;V_0,\varepsilon)$ with the poissionian probability of observing N particles in the observation volume $P_{\#}(N)$.

$$\Pi(k;V_0,\varepsilon) \equiv \sum_{N=0}^{\infty} p^{(N)}{}_{3DG}(k;V_0,\varepsilon)P_{\#}(N). \quad \text{Eq. 1.5.12}$$

The PCH for multiple independent species can be obtained by convoluting the PCH for each individual species (eq 1.5.12) as given in eq. 1.5.13.

$$\Pi(k;\overline{N}_1,\overline{N}_2,..\varepsilon_1,\varepsilon_2..) = \Pi(k;\overline{N}_1,\varepsilon_1) \otimes \Pi(k;\overline{N}_2,\varepsilon_2) \dots \quad \text{Eq. 1.5.13}$$

For monitoring protein oligomerization using this technique, it is important to control the degree of labeling very close to one. The reason is that multiple labeling per protein molecules will result in an increased brightness per subunit, and this would lead to erroneous interpretation of the results, because a protein monomer might appear as a dimer due to second degree labeling. Many proteins also form oligomers at concentrations higher than the single molecule sensitivity regimes, and the use of PCH technique provide little insights into those events. For a mixture, the resolvability of PCH technique is only limited to a mixture of two different non interacting particles [79].

References

1. Goodsell, D.S. and A.J. Olson, *Structural symmetry and protein function.* Annu Rev Biophys Biomol Struct, 2000. **29**: p. 105-53.

2. Hashimoto, K., et al., *Caught in self-interaction: evolutionary and functional mechanisms of protein homooligomerization.* Phys Biol. **8**(3): p. 035007.

3. Blundell, T., et al., *Insulin: The Structure in the Crystal and its Reflection in Chemistry and Biology by*, in *Advances in Protein Chemistry*. 1972, Academic Press. p. 279-402.

4. Lumry, R. and S. Rajender, *Enthalpy-entropy compensation phenomena in water solutions of proteins and small molecules: a ubiquitous property of water.* Biopolymers, 1970. **9**(10): p. 1125-227.

5. Evans, P.R., *Structural aspects of allostery.* Current Opinion in Structural Biology, 1991. **1**(5): p. 773-779.

6. Perutz, M.F., *Mechanisms of cooperativity and allosteric regulation in proteins.* Q Rev Biophys, 1989. **22**(2): p. 139-237.

7. Srere, P.A., *Why are enzymes so big?* Trends in Biochemical Sciences, 1984. **9**(9): p. 387-390.

8. Kurland, C.G., *Translational accuracy and the fitness of bacteria.* Annu Rev Genet, 1992. **26**: p. 29-50.

9. Parker, J., *Errors and alternatives in reading the universal genetic code.* Microbiol Rev, 1989. **53**(3): p. 273-98.

10. Crick, F.H.C. and J.D. Watson, *Virus Structure: General Principles*, in *Ciba Foundation Symposium - Steroid Hormones and Enzymes (Book II of Colloquia on Endocrinology)*. 2008, John Wiley & Sons, Ltd. p. 5-18.

11. Wolynes, P.G., *Symmetry and the energy landscapes of biomolecules.* Proc Natl Acad Sci U S A, 1996. **93**(25): p. 14249-55.

12. Stossel, T.P., *From signal to pseudopod. How cells control cytoplasmic actin assembly.* J Biol Chem, 1989. **264**(31): p. 18261-4.

13. Mitchison, T. and M. Kirschner, *Dynamic instability of microtubule growth.* Nature, 1984. **312**(5991): p. 237-242.

14. Mitchison, T.J., *Microtubule dynamics and kinetochore function in mitosis.* Annu Rev Cell Biol, 1988. **4**: p. 527-49.

15. Crick, F.H.C. and J.D. Watson, *Structure of Small Viruses.* Nature, 1956. **177**(4506): p. 473-475.

16. Cohen-Krausz, S. and S. Trachtenberg, *The Flagellar Filament Structure of the Extreme Acidothermophile Sulfolobus shibatae B12 Suggests that Archaeabacterial Flagella have a Unique and Common Symmetry and Design.* Journal of Molecular Biology, 2008. **375**(4): p. 1113-1124.

17. Hulmes, D.J., *The collagen superfamily--diverse structures and assemblies.* Essays Biochem, 1992. **27**: p. 49-67.

18. Hanson, P.I. and S.W. Whiteheart, *AAA+ proteins: have engine, will work.* Nat Rev Mol Cell Biol, 2005. **6**(7): p. 519-529.

19. Neuwald, A.F., et al., *AAA+: A class of chaperone-like ATPases associated with the assembly, operation, and disassembly of protein complexes.* Genome Res, 1999. **9**(1): p. 27-43.

20. Iyer, L.M., et al., *Evolutionary history and higher order classification of AAA+ ATPases.* J Struct Biol, 2004. **146**(1-2): p. 11-31.

21. Vale, R.D., *AAA proteins. Lords of the ring.* J Cell Biol, 2000. **150**(1): p. F13-9.

22. Erdmann, R., *AAA ATPases: Structure and function.* Biochimica et Biophysica Acta (BBA) - Molecular Cell Research. **1823**(1): p. 1.

23. Wang, J., et al., *Nucleotide-dependent conformational changes in a protease-associated ATPase HsIU.* Structure, 2001. **9**(11): p. 1107-16.

24. Smith, G.R., et al., *A link between sequence conservation and domain motion within the AAA+ family.* J Struct Biol, 2004. **146**(1-2): p. 189-204.

25. Weibezahn, J., et al., *Characterization of a trap mutant of the AAA+ chaperone ClpB.* J Biol Chem, 2003. **278**(35): p. 32608-17.

26. Ogura, T., S.W. Whiteheart, and A.J. Wilkinson, *Conserved arginine residues implicated in ATP hydrolysis, nucleotide-sensing, and inter-subunit interactions in AAA and AAA+ ATPases.* J Struct Biol, 2004. **146**(1-2): p. 106-12.

27. Song, H.K., et al., *Mutational studies on HslU and its docking mode with HslV.* Proc Natl Acad Sci U S A, 2000. **97**(26): p. 14103-8.

28. Carmo-Silva, A.E. and M.E. Salvucci, *The activity of Rubisco's molecular chaperone, Rubisco activase, in leaf extracts.* Photosynth Res. **108**(2-3): p. 143-55.

29. Lorimer, G.H., M.R. Badger, and T.J. Andrews, *The activation of ribulose-1,5-bisphosphate carboxylase by carbon dioxide and magnesium ions. Equilibria, kinetics, a suggested mechanism, and physiological implications.* Biochemistry, 1976. **15**(3): p. 529-36.

30. Andersson, I. and A. Backlund, *Structure and function of Rubisco.* Plant Physiol Biochem, 2008. **46**(3): p. 275-91.

31. Whitney, S.M., R.L. Houtz, and H. Alonso, *Advancing our understanding and capacity to engineer nature's CO2-sequestering enzyme, Rubisco.* Plant Physiol. **155**(1): p. 27-35.

32. Mueller-Cajar, O., M. Stotz, and A. Bracher, *Maintaining photosynthetic CO2 fixation via protein remodelling: the Rubisco activases.* Photosynth Res. **119**(1-2): p. 191-201.

33. Cleland, W.W., et al., *Mechanism of Rubisco: The Carbamate as General Base.* Chem Rev, 1998. **98**(2): p. 549-562.

34. Parry, M.A., et al., *Rubisco regulation: a role for inhibitors.* J Exp Bot, 2008. **59**(7): p. 1569-80.

35. Andralojc, P.J., et al., *2-Carboxy-D-arabinitol 1-phosphate (CA1P) phosphatase: evidence for a wider role in plant Rubisco regulation.* Biochem J. **442**(3): p. 733-42.

36. Seemann, J.R., J. Kobza, and B.D. Moore, *Metabolism of 2-carboxyarabinitol 1-phosphate and regulation of ribulose-1,5-bisphosphate carboxylase activity.* Photosynth Res, 1990. **23**(2): p. 119-30.

37. Berry, J.A., et al., *Isolation, identification, and synthesis of 2-carboxyarabinitol 1-phosphate, a diurnal regulator of ribulose-bisphosphate carboxylase activity.* Proc Natl Acad Sci U S A, 1987. **84**(3): p. 734-8.

38. Ellis, R.J., *The most abundant protein in the world.* Trends in Biochemical Sciences, 1979. **4**(11): p. 241-244.

39. Somerville, C.R., A.R. Portis, and W.L. Ogren, *A Mutant of Arabidopsis thaliana Which Lacks Activation of RuBP Carboxylase In Vivo.* Plant Physiol, 1982. **70**(2): p. 381-7.

40. Salvucci, M.E., A.R. Portis, Jr., and W.L. Ogren, *A soluble chloroplast protein catalyzes ribulosebisphosphate carboxylase/oxygenase activation in vivo.* Photosynth Res, 1985. **7**(2): p. 193-201.

41. Robinson, S.P. and A.R. Portis, Jr., *Adenosine triphosphate hydrolysis by purified rubisco activase.* Arch Biochem Biophys, 1989. **268**(1): p. 93-9.

42. Robinson, S.P. and A.R. Portis, *Ribulose-1,5-bisphosphate carboxylase/oxygenase activase protein prevents the in vitro decline in activity of ribulose-1,5-bisphosphate carboxylase/oxygenase.* Plant Physiol, 1989. **90**(3): p. 968-71.

43. Robinson, S.P., et al., *Purification and assay of rubisco activase from leaves.* Plant Physiol, 1988. **88**(4): p. 1008-14.

44. Salvucci, M.E. and S.J. Crafts-Brandner, *Mechanism for deactivation of Rubisco under moderate heat stress.* Physiologia Plantarum, 2004. **122**(4): p. 513-519.

45. Salvucci, M.E. and S.J. Crafts-Brandner, *Relationship between the heat tolerance of photosynthesis and the thermal stability of rubisco activase in plants from contrasting thermal environments.* Plant Physiol, 2004. **134**(4): p. 1460-70.

46. Crafts-Brandner, S.J. and M.E. Salvucci, *Rubisco activase constrains the photosynthetic potential of leaves at high temperature and CO2.* Proc Natl Acad Sci U S A, 2000. **97**(24): p. 13430-5.

47. Stotz, M., et al., *Structure of green-type Rubisco activase from tobacco.* Nat Struct Mol Biol. **18**(12): p. 1366-70.

48. van de Loo, F.J. and M.E. Salvucci, *Activation of ribulose-1,5-biphosphate carboxylase/oxygenase (Rubisco) involves Rubisco activase Trp16.* Biochemistry, 1996. **35**(25): p. 8143-8.

49. Esau, B.D., G.W. Snyder, and A.R. Portis, Jr., *Differential effects of N- and C-terminal deletions on the two activities of rubisco activase.* Arch Biochem Biophys, 1996. **326**(1): p. 100-5.

50. Barta, C., et al., *Structural changes associated with the acute thermal instability of Rubisco activase.* Arch Biochem Biophys. **499**(1-2): p. 17-25.

51. Wang, Z.Y., R.T. Ramage, and A.R. Portis, Jr., *Mg2+ and ATP or adenosine 5'-[gamma-thio]-triphosphate (ATP gamma S) enhances intrinsic fluorescence and induces aggregation which increases the activity of spinach Rubisco activase.* Biochim Biophys Acta, 1993. **1202**(1): p. 47-55.

52. Li, C., D. Wang, and A.R. Portis, Jr., *Identification of critical arginine residues in the functioning of Rubisco activase.* Arch Biochem Biophys, 2006. **450**(2): p. 176-82.

53. Blayney, M.J., S.M. Whitney, and J.L. Beck, *NanoESI mass spectrometry of Rubisco and Rubisco activase structures and their interactions with nucleotides and sugar phosphates.* J Am Soc Mass Spectrom. **22**(9): p. 1588-601.

54. Lilley, R.M. and A.R. Portis Jr, *ATP Hydrolysis Activity and Polymerization State of Ribulose-1,5-Bisphosphate Carboxylase Oxygenase Activase (Do the Effects of Mg2+, K+, and Activase Concentrations Indicate a Functional Similarity to Actin?).* Plant Physiol, 1997. **114**(2): p. 605-613.

55. Hong, P., S. Koza, and E.S. Bouvier, *Size-Exclusion Chromatography for the Analysis of Protein Biotherapeutics and their Aggregates.* J Liq Chromatogr Relat Technol. **35**(20): p. 2923-2950.

56. Elson, E.L. and D. Magde, *Fluorescence correlation spectroscopy. I. Conceptual basis and theory.* Biopolymers, 1974. **13**(1): p. 1-27.

57. Magde, D., E.L. Elson, and W.W. Webb, *Fluorescence correlation spectroscopy. II. An experimental realization.* Biopolymers, 1974. **13**(1): p. 29-61.

58. Magde, D., E. Elson, and W.W. Webb, *Thermodynamic Fluctuations in a Reacting Systemâ€"Measurement by Fluorescence Correlation Spectroscopy.* Physical Review Letters, 1972. **29**(11): p. 705-708.

59. Jameson, D.M., J.A. Ross, and J.P. Albanesi, *Fluorescence fluctuation spectroscopy: ushering in a new age of enlightenment for cellular dynamics.* Biophys Rev, 2009. **1**(3): p. 105-118.

60. Muller, J.D., Y. Chen, and E. Gratton, *Fluorescence correlation spectroscopy.* Methods Enzymol, 2003. **361**: p. 69-92.

61. Lakowicz, J. and N. Thompson, *Fluorescence Correlation Spectroscopy*, in *Topics in Fluorescence Spectroscopy*. 1999, Springer US. p. 337-378.

62. Abney, J.R., et al., *Chromatin dynamics in interphase nuclei and its implications for nuclear structure.* J Cell Biol, 1997. **137**(7): p. 1459-68.

63. Hemmerich, P., et al., *Dynamics of inner kinetochore assembly and maintenance in living cells.* J Cell Biol, 2008. **180**(6): p. 1101-14.

64. Boxer, S.G., *Molecular transport and organization in supported lipid membranes.* Curr Opin Chem Biol, 2000. **4**(6): p. 704-9.

65. Kahya, N. and P. Schwille, *Fluorescence correlation studies of lipid domains in model membranes.* Mol Membr Biol, 2006. **23**(1): p. 29-39.

66. Berland, K.M., P.T. So, and E. Gratton, *Two-photon fluorescence correlation spectroscopy: method and application to the intracellular environment.* Biophys J, 1995. **68**(2): p. 694-701.

67. Lukacs, G.L., et al., *Size-dependent DNA mobility in cytoplasm and nucleus.* J Biol Chem, 2000. **275**(3): p. 1625-9.

68. Wachsmuth, M., W. Waldeck, and J. Langowski, *Anomalous diffusion of fluorescent probes inside living cell nuclei investigated by spatially-resolved fluorescence correlation spectroscopy.* J Mol Biol, 2000. **298**(4): p. 677-89.

69. Rajagopalan, S., F. Huang, and A.R. Fersht, *Single-Molecule characterization of oligomerization kinetics and equilibria of the tumor suppressor p53.* Nucleic Acids Res. **39**(6): p. 2294-303.

70. Krouglova, T., J. Vercammen, and Y. Engelborghs, *Correct diffusion coefficients of proteins in fluorescence correlation spectroscopy. Application to tubulin oligomers induced by Mg2+ and Paclitaxel.* Biophys J, 2004. **87**(4): p. 2635-46.

71. Bulseco, D.A., et al., *Chapter 21 - Fluorescence Correlation Spectroscopy: Molecular Complexing in Solution and in Living Cells*, in *Methods in Cell Biology*, Academic Press. p. 489-524.

72. Hink, M.A., M. Postma, and P.M. Conn, *Chapter 11 - Monitoring Receptor Oligomerization by Line-Scan Fluorescence Cross-Correlation Spectroscopy*, in *Methods in Cell Biology*, Academic Press. p. 197-212.

73. Ohta, S., et al., *The interaction of Hsp104 with yeast prion Sup35 as analyzed by fluorescence cross-correlation spectroscopy.* Biochemical and Biophysical Research Communications. **442**(1-2): p. 28-32.

74. Salvucci, M.E., *Potential for interactions between the carboxy- and amino-termini of Rubisco activase subunits.* FEBS Lett, 2004. **560**(1-3): p. 205-9.

75. Chen, Y., et al., *The photon counting histogram in fluorescence fluctuation spectroscopy.* Biophys J, 1999. **77**(1): p. 553-67.

76. Perroud, T.D., et al., *Photon counting histogram for one-photon excitation.* Chemphyschem, 2003. **4**(10): p. 1121-3.

77. Terada, N., et al., *Size Distribution of Linear and Helical Polymers in Actin Solution Analyzed by Photon Counting Histogram.* Biophysical Journal, 2007. **92**(6): p. 2162-2171.

78. Mandel, L., *Fluctuations of photon beams and their correlations.* Proc. Phys. Soc. , 1958. **72**: p. 1037-1048.

79. Muller, J.D., Y. Chen, and E. Gratton, *Resolving heterogeneity on the single molecular level with the photon-counting histogram.* Biophys J, 2000. **78**(1): p. 474-86.

CHAPTER 2

MATERIALS AND METHODS

Protein expression, purification, labeling and the characterization work was done at the laboratory of Dr. Rebekka Wachter, and the methods were generously provided by her.

2.1 Preparation of Recombinant Rca and Labeling

Cloning, Expression and Purification of 6His-Tagged and Untagged Cotton β-Rca

Plasmid DNA, either pET-23a(+) or pET151/dTOPO, both containing a cotton short form β-Rca with C-terminal Ala-Cys insertion [1], was purified from TOP10 competent cells (Invitrogen) with the QIAprep Spin Miniprep Kit using manufacturers protocol. The correct sequence of individual transformants was verified by DNA sequencing.

Purified plasmid DNA (0.5-1.0 μL) was mixed with 50 μL of thawed competent cells (Rosetta (DE3) pLysS or BL21* (DE3)) and incubated on ice for 30 minutes. Next, the solution was heat shocked for 45 sec at 42C and immediately placed on ice for 2 minutes. 0.5mL of RT SOC media was added and the entire mixture was shook at 250 rpm, 37C for 1 hour. 20% of the mixture was spread on the agar plates containing appropriate amount of antibiotics and left for overnight at 37C incubator. Next day, single colonies of Rosetta (DE3) pLysS containing the pET-23a(+) plasmid with a Gh SF $RCA_{(1\text{-}378CA379)}$ insertion or containing the pET151/dTOPO plasmid with the same insert were used to inoculate 25 mL cultures of LB + carb + cam (100 μg/mL carbenicillin and 34 μg/mL chloroamphenicol (additionally for Rosetta only)) and grown overnight at

37°C, 250 rpm. From each overnight culture, 5 mL was transferred into 6 separate 2.8L fernbach flasks contain 1 L of LB + carb or/and cam and grown at 37°C, 250 rpm to an OD_{600} ~ 0.6. At this point the cultures were quickly cooled on ice to ~ room temperature. Protein expression was then induced with the addition of 100 mg of Isopropyl β-D-1-thiogalactopyranoside (IPTG) to each culture. Protein induction was continued at 20°C, 200 rpm for ~ 8 hours at which point the cells were harvested by centrifugation and the pellets frozen at -80°C for storage.

Cell pellets were thawed, resuspended and lysed by sonication as described above. Cell lysate was pelleted at 15 K for 30 minutes at 4°C. Supernatant was passed through a 0.8 μm syringe filter prior to loading on a Hi-Trap Ni-NTA column (GE Healthcare). The 5 mL column was washed with 5 column volumes (CVs) of 50 mM imidazole-containing buffer followed by a 5 CV 100 mM imidazole wash. His-tagged activase was eluted with a 25ml 500 mM imidazole wash. The pooled 500 mM imidazole fractions were dialyzed overnight to remove the imidazole while simultaneously being digested with rTEV protease. The sample was dialyzed overnight at 10°C against 1 L of 25 mM Tris pH 8.0, 300 mM NaCl, 0.1 mM ADP, 0.1 mM DTT and 1 mM EDTA. Digested activase was reapplied to the column where it eluted at 20 mM imidazole.

Protein was concentrated to a volume of ~ 2.5 mL in Centriprep concentrators (Millipore). The buffer was exchanged into 25 mM HEPES pH 8.0, 250 mM KCl, 5 mM $MgCl_2$, 2 mM ADP and 10% glycerol using a PD-10 column (GE Healthcare),. Protein concentration was determined by the Bradford method, with typical yields of 3-4 mg/L cell culture. Recombinant cotton β-Rca-378AC was also expressed in *E. coli* without an

affinity tag, and purified by classical procedures as described previously [2]. All Rca preparations were flash-frozen and stored at -80°C.

Dye Conjugation Methodology

Cotton Rca was labeled with alexa 546 C_5- maleimide fluorophore (Invitrogen) using the method outlined in [1]. In a typical labeling reaction, 28 μM of 236 μl Rca was mixed with 50 mM potassium phosphate buffer pH 7.2, 3μl of 500 mM ADP, and 54 μl 1.93 mM alexa dye. Maleimide groups rapidly and selectively react with thiols, forming stable covalent thioester bonds. The mixture was incubated overnight at 4°C. In control reactions, 50 mM dithiothreitol (DTT) were added prior to the addition of reagent. To remove excess label, an equal volume of saturated ammonium sulfate (300 μL) was added to precipitate activase. After 30 min incubation at 4^0C, the pellets were collected by centrifugation, (Eppendorf Centrifuge 5418; 5min, 12000 rpm). The pellets were suspended in 170 μl buffer containing of 25 mM HEPES pH 7.5, 250 mM KCl, 1 mM ADP, and 10% glycerol. Desalting was done by passing the protein through gel filtration using a spin column (Sephadex G50-fine, 2ml bed volume, centrifugation for 2 min at 400 *g*). Aliquots of 6 μL 30-60 μM Rca were prepared by flash freezing and stored at -80^0C. The composition of the 1X buffer used for the study is 25 mM HEPES pH 7.6, 250 mM KCl, 2 mM ADP, 5 mM $MgCl_2$ and 10% glycerol.

HPLC, Spectrophotometric and Mass Spectrometric Analysis of Labeled Protein

Compounds stick to reverse phase HPLC columns in high aqueous mobile phase and are eluted from RP HPLC columns with high organic mobile phase which are separated based on their hydrophobic character (Waters 1525 Micro binary pump HPLC

system equipped with a Waters 2489 dual absorbance detector) on a C18 analytical column (Vydac) using a water/acetonitrile gradient containing 0.1% trifluoroacetic acid. Protein was monitored by optical density (O.D.) 280 nm, and alexa by O.D. 550 nm. All protein eluted at 53 min, whereas free alexa eluted at 47.5 min. Absorbance spectrum of the peak fraction was measured (650-250 nm, UV2401-PC spectrophotometer, Schimadzu) using 50 % acetonitrile/TFA as a blank. The concentrations were calculated from the absorbance values at wavelengths: 556 nm for alexa (ε_{556} = 104,000 $M^{-1}cm^{-1}$) and 280 nm for Rca (ε_{280} = 44,350 $M^{-1}cm^{-1}$, calculated from the sequence). A correction was applied to the concentration of Rca for free dye contributions. This was done by applying correction factor 0.146 at O.D. 556 nm using the formula O.D. 280 - (O.D. 556 * 0.146). The correct molecular weight of the protein was verified by obtaining MALDI spectra on a Voyager DE STR mass spectrometer (fig. 2.1.1).

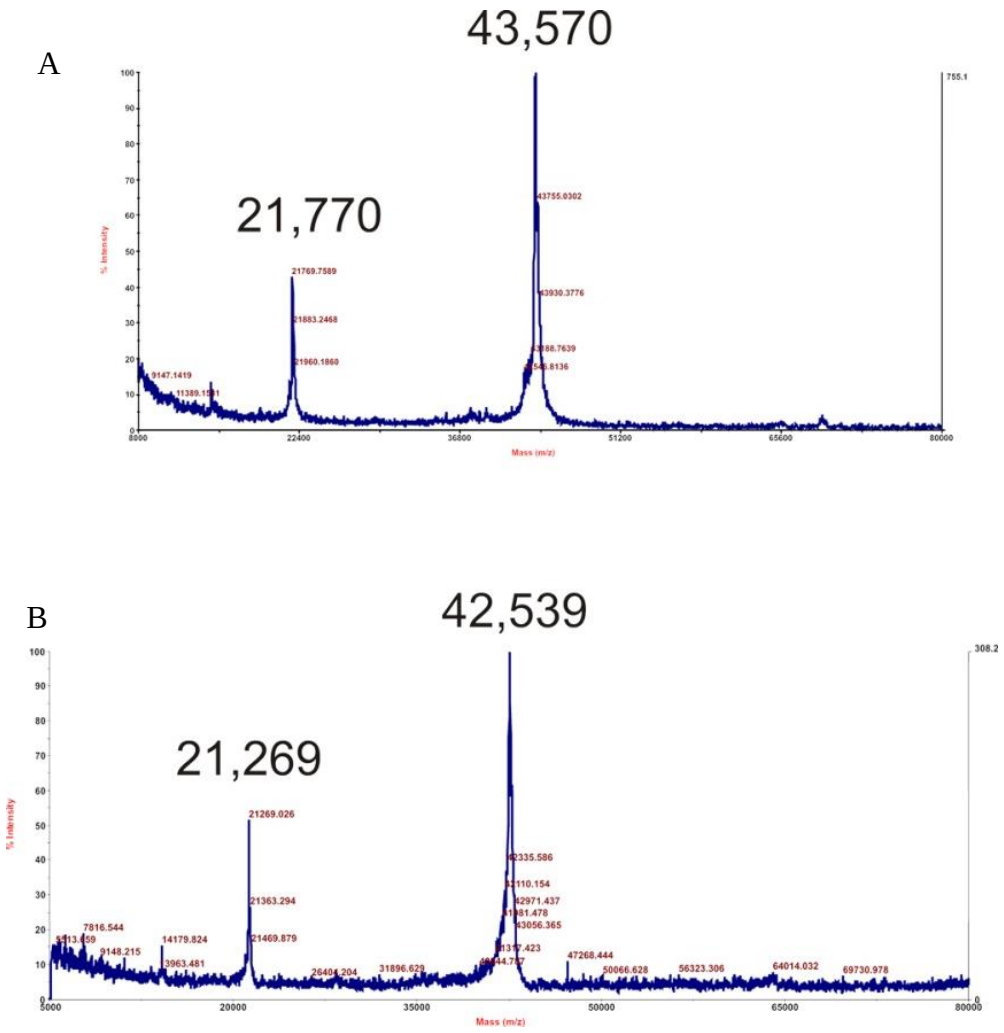

Figure 2.1.1 MALDI Spectra of wt β-Rca. Spectra were collected on labeled and unlabeled Rca preparations, and compared to their theoretical values. (A) Labeled protein spectra exhibit main peaks with m/z = 43,570 (z=1), and m/z = 21,770 (z=2). The calculated mass is 43,493 g/mol. (B) Unlabeled protein spectra exhibit main peaks with m/z = 42,539 (z=1), and m/z = 21,269 (z=2). The calculated mass is 42,459 g/mol. The error of the instrument is estimated to be about 90 Da for a protein of this size.

Cloning, Expression and Purification of 6His-Tagged and Untagged Cotton β-Rca D173N

A blunt-ended PCR product consisting of 1144 base pairs was amplified from a pET23a (+) expression plasmid containing full-length cotton beta-Rca with a C-terminal Ala-Cys insert after residue 378 of the 380-residue protein. The mutant catalyzes ATP hydrolysis and promotes activation of Rubisco. The reaction was described in a previously published article. Addition mutation of aspartic acid into asparagine located in 173 sequences was performed in order to block the enzymatic activity of the Rca by damaging the ATP hydrolysis rather than binding of the nucleotide. The 50 µL PCR reaction contained 20 ng plasmid, 0.625 U Pfu Turbo DNA polymerase (Stratagene), 1X Cloned Pfy DNA polymerase reaction buffer (Stratagene), 125 µM of each dNTP (Invitrogen) and 5 pmol of forward and reverse primers (Integrated DNA Technologies) with the following sequences respectively. Blunt-ended PCR product amplification, directional "TOPO" cloning of the blunt-ended PCR product into a linear pET151/D-TOPO vector (Invitrogen) and subsequent transformation in one shot TOP 10 competent (Invitrogen) were carried out according to manufacturer's recommendations. Seven champion ^{TM} pET directional TOPO expression vectors (Invitrogen) provides a vector that carries a T7lac promoter for high-level expression. Plasmid was prepared from individual transformant colonies using the QIAprep spin miniprep kit (Qiagen) and the correct insert was verified by sequencing at the Arizona State University School of Life Sciences DNA Laboratory.

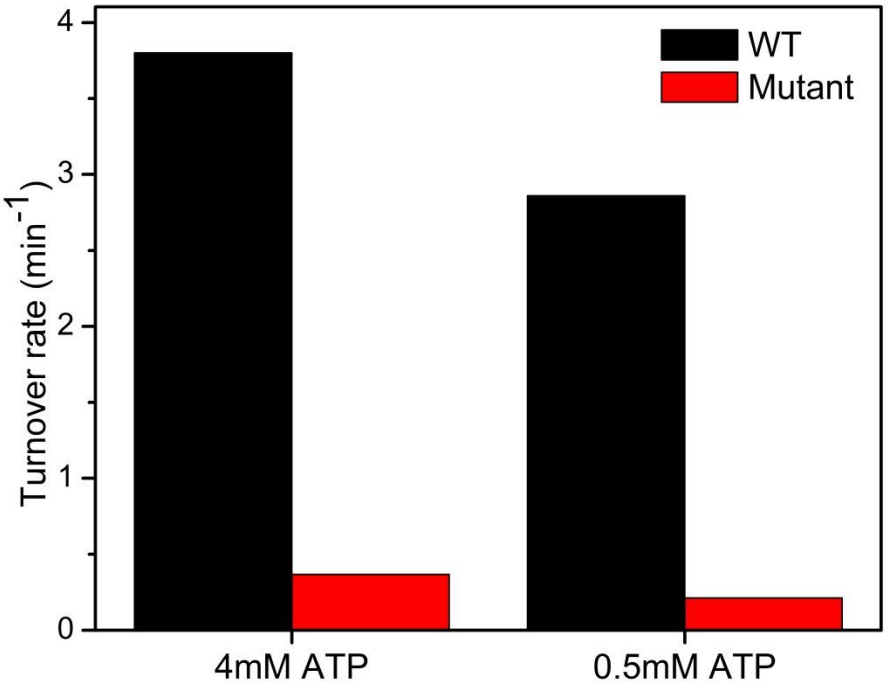

WT	**3.8**	**2.86**
D173N	**0.368**	**0.212**

Figure 1.1.2. Comparison of wt and D173N Rca ATP-ase Activity. Kinetic activity assay was performed on D173N mutant and wt-like with two ATP concentrations: 4mM and 0.5mM.

Expression of β-Rca D173N

The pET151/D-TOPO vectors containing the cotton β-Rca wt insert were transformed into *E. coli* BL21 star (DE3) (Invitrogen). The DE3 means this strain contains the lambda DE3 lysogen which carries the gene for T7 RNA polymerase under the control of the lacUV5 promoter. IPTG is required to induce expression of the T7 RNA polymerase. Single colonies were cultured overnight in 25 mL of Luria-Bertani (LB) media supplemented with 100 μg/mL carbenicillin, then used to inoculate 1 L LB plus 100 μg/mL carbenicillin. Growth was continued at 250 rpm and 37°C until the OD_{600} reached ~ 0.6. The cultures were then cooled to ~ 25°C, 100 mg of isopropyl-β-D-thio-galactoside (IPTG) was added to each flask and growth continued at 200 rpm and 25°C. After 8 hours, the cultures were harvested by centrifugation (20 min, 600 rpm) and the cell pellets frozen at -80°C. Thawed cell paste was re-suspended in 50 mL of 25 mM Tris-HCl pH 8.0, 10 mM imidazole pH 8.0, 10% glycerol, ~19 mg hen egg white lysozyme, 1 mM phenylmethanesulfonylfluoride (PMSF), 2 mM DTT, 0.1 mM ADP, 1mM EDTA, stirred for 30 min at 4^0C. Next, the mixture was disrupted by sonication, and then 500 mM NaCl was added. The lysate was pelleted by centrifugation, and the supernatant was passed through a 1.2 μm syringe filter and loaded onto a Ni-NTA column (Qiagen). Rca was purified using an imidazole buffer step gradient (25 mM Tris-HCl pH 8.0, 500 mM NaCl, 2 mM DTT and 0.1 mM ADP, plus variable amounts of imidazole). After washing with 10 mM and 80 mM imidazole buffer, His-tagged Rca was eluted from the column with 35 mL of 200 mM imidazole buffer and in addition with 35 mL of 500 mM imidazole buffer. Protein fractions were pooled, 1.2 mg of tobacco

etch virus protease (TEV) was added to remove the 6His-tag, and the sample was dialyzed overnight at 4°C against 1 L of 25 mM Tris-HCl pH 8.0, 100 mM NaCl, 1 mM ADP, 2 mM DTT and 0.1 mM EDTA. The dialysate was reapplied to a Ni-NTA column (Qiagen), and TEV-cleaved Rca was collected in the flow-through and by washing with 20 mM imidazole. Protein was concentrated in Centriprep centrifugal concentrators (Millipore) to a volume of ~ 2.5 mL. The buffer was exchanged into 25 mM HEPES pH 7.5, 250 mM KCl, 2 mM ADP (or 2mM ATP), 5 mM $MgCl_2$ and 10% glycerol using a PD-10 column (GE Healthcare). Additionally, purifications were performed where no $MgCl_2$ was added to the buffer. Protein concentration was determined using the Bradford method, with typical yields of 1.6 mg of protein per liter of cell culture. The concentration was 110.0 μM ± 9.1 (n = 9)

Dye Conjugation Methodology

Cotton β-Rca D173N was covalently labeled with the alexa 546 C_5- maleimide fluorophore (Invitrogen). A typical reaction consisted of 100 μM Rca, 3 μl 500 mM ADP, 3μl 125 mM KCl, and 350 μM Alexa dye (stock prepared in 50 mM HEPES pH 7.2), to provide a final volume of 300 μl in 50 mM HEPES pH 7.2. Samples were incubated overnight at 4°C. To remove excess label, 300 μl saturated ammonium sulfate was added, the mixture was incubated for 30 min at 4°C, and the pellet was collected by centrifugation in an micro-centrifuge at 12,000 rpm. Pellet was suspended in 170 μl of 25 mM HEPES pH 7.5, 250 mM KCl, 2 mM ADP, 5 mM $MgCl_2$ and 10% glycerol, and desalted by passing the sample twice through a gel filtration spin column (Sephadex G50-fine, 2 ml bed volume, 400 gm centrifugation for 2 min). 5 μl aliquots (48.3 μM ± 6.2 (n

= 6) Rca subunit concentration) were flash-frozen in 1X sample buffer and stored at -80 °C. 1X sample buffer consisted of 25 mM HEPES pH 7.5, 250 mM KCl, 2 mM ADP, 5mM $MgCl_2$, and 10% glycerol. The molar ratio of alexa: Rca was 1.03 (n = 2).

Similar preparation was performed substituting nucleoside diphosphate into nucleoside triphosphate. 5 µl aliquots (91.53 µM ± 5.6 (n = 6) Rca subunit concentration) were flash-frozen in 1X sample buffer and stored at -80 °C. 1X sample buffer consisted of 25 mM HEPES pH 7.5, 250 mM KCl, 2 mM ATP, 5 mM $MgCl_2$, and 10% glycerol. The molar ratio of alexa: Rca was 0.94 (n = 2) (see appendix II for spectroscopic data figs. A.2.1-3).

Non-Affinity Protein Expression and Purification of wt β-Rca in Presence of ATP-γ-S

Recombinant cotton β-Rca wt was also expressed in *E. coli* without an affinity tag, and purified by traditional procedures as described previously. Rca preparations were flash-frozen and stored at -80°C until further use. Samples were labeled with alexa 546 fluorophore by previously published technique. The only change applied here was the alteration of the nucleotide into an analog: ATP-γ-S. For unlabeled preparations, the samples were buffer exchanged using Sephadex G50 gel filtration column and finally 2 mM analog was added to the sample.

HPLC, Spectrophotometric and Mass Spectrometric Analysis of Labeled Protein

Alexa-labeled D173N Rca samples were analyzed by reverse-phase HPLC (Agilent Technologies 1260 Infinity Quaternary LC system, Agilent Technologies 1100 Series Diode-Array detector) on a C18 analytical column (Phenomenex Prodigy) using a linear water/acetonitrile gradient with 0.1% trifluoroacetic acid. Before injecting any

samples the pump was primed and the instrument was run for 15 min in a solvent A (0.1% TFA, water). The method was applied without any injection (empty injection) to check for any carryovers from previous runs. If the baseline is clean the buffer injection was applied and again the same method was used for a baseline chromatogram. Finally the sample was injected; protein was monitored by O.D. 280 nm, O.D. 220nm, and Alexa by O.D. 550 nm. All protein eluted at 36.5 min, whereas free alexa eluted at 40.5 min. The protein fraction was collected and its absorbance spectrum determined (650 - 250 nm, UV2401-PC spectrophotometer, Schimadzu) using 50 % acetonitrile/TFA as a blank. The column was washed with dd water and stored in 50% water and 50% ACN (without any TFA). The spectrum was utilized to calculate the molar alexa: protein ratio. The concentration of alexa was determined from the O.D. 556 nm (ε_{556} = 104,000 $M^{-1}cm^{-1}$) and the concentration of Rca from the O.D. 280 nm after correction for dye contributions. To this end, the O.D. 556 was multiplied by the correction factor 0.1134 and the resulting value subtracted from the O.D. 280. The Rca extinction coefficient was calculated from the protein's sequence (ε_{280} = 44,350 $M^{-1}cm^{-1}$). To verify the correct molecular weight of labeled protein, MALDI spectra were collected on a Voyager DE STR mass spectrometer. Spectra were collected on labeled and unlabeled Rca preparations, and compared to their theoretical values. Labeled protein spectra exhibit main peaks with m/z = 44,185 (z = 1), and m/z = 22,077 (z = 2). The calculated mass is 44,230 g/mol. Unlabeled protein spectra exhibit main peaks with m/z = 43,190 (z = 1), and m/z = 21,607 (z = 2). The calculated mass is 43,237 g/mol. The error of the instrument is estimated to be about 90 Da for a protein of this size (relevant results are shown in the appendix).

2.2 Sample Preparation for FCS and PCH Measurements

WT Rca in Presence of ADP-Mg^{2+}

In a typical experiment, 57 µl 2X sample buffer (50 mM HEPES pH 7.6, 500 mM KCl, 4 mM ADP, 10 mM $MgCl_2$ and 20% glycerol) and 57 µl nanopure water were added to 6 µl labeled Rca (52 µM) to provide a 2.6 µM stock of labeled protein. A 30 µM stock of unlabeled Rca was prepared in a similar manner. All solutions were incubated at 22°C while performing FCS experiments which took less than 2.5 hours to finish. For each experiment, appropriate amounts of labeled and unlabeled Rca were combined in a tube containing 1X buffer to give the desired final protein concentration. For example, to prepare a mix of 50 nM labeled and 5.0 µM unlabeled Rca, 3.8 µl of 2.6 µM labeled Rca stock were combined with 33.3 µl of 30 µM unlabeled Rca stock, and 81.5 µl each of 2X buffer and nanopure water were added (200 µl final volume). To allow for subunit equilibration, each sample was incubated for 10 min at 22°C prior to analysis. All experiments were performed on 50 nM labeled and 0 – 125 µM unlabeled Rca.

D173N Rca in Presence of ATP-Mg^{2+}

In a Typical FCS experiment, 500 µL 2X sample buffer (50 mM HEPES pH 7.6, 500 mM KCl, 4 mM ATP, 10 mM $MgCl_2$, and 20% glycerol) was mixed with 500 µL nano-pure water to obtain the 1X buffer solution used for all the following dilutions. Frozen labeled (86 µM) and unlabeled (75 µM) solutions made in the 1X buffer were taken out of the -80^{0}C freezer and were thawed over ice (4^{0}C) for a few minutes. 2 µL of labeled mutant Rca (86 µM) was added to 84 µL of the 1X buffer solution to provide a 2 µM stock solution of labeled mutant Rca. A 2 µM and a 10 µM stock solution of

unlabeled Rca were prepared in a similar manner. Both the labeled and unlabeled stock solutions were stored on ice (4^0C) while performing FCS experiment. For each experiment, appropriate amount of labeled and unlabeled Rca solutions were mixed in a siliconized low-retention micro-centrifuge tubes containing 1X buffer to give the desired final protein concentration. For example, to prepare a 120 µL mixture of 50 nM labeled and 7.95 µM unlabeled Rca, 3µL of 2 µM labeled Rca stock solution were combined with 95.4 µL of 10 µM unlabeled stock solution and 21.6 µL of 1X ATP buffer. To allow subunit equilibration each sample were incubated for 10 min on ice before performing experiments. All experiments were performed on 50 nM labeled and 0-75 µM unlabeled Rca. Mutant Rca solutions in ADP were also prepared in a similar manner.

Thawed labeled and unlabeled Rca solutions in ATP and in ADP were mixed in a ratio of 3:1, in order to obtain the stock solutions for the nucleotide mixing experiment. The concentrations of the newly prepared stock solutions were calculated from the concentrations of the original stock solutions, and their respective volumes used for mixing. For example, 3 µL of 90.4 µM labeled protein in ATP was mixed with 1 µL of 50 µM labeled protein in ADP to obtain 4 µL of 80.3 µM labeled stock solution in 3:1 ATP: ADP. These newly prepared protein stock solutions were then diluted using the same protocol as mentioned above to prepare the solutions for FCS measurements. The 2X buffer solutions used for the mixture of nucleotide experiments (Fig. 1 C, D) contain 50 mM HEPES pH 7.6, 500 mM KCl, 3 mM ATP, 1 mM ADP 10 mM $MgCl_2$, and 20% glycerol; and the buffer used for low $MgCl_2$ experiment (Fig. 1 E, F) contain 50 mM HEPES pH 7.6, 500 mM KCl, 3 mM ATP, 1 mM ADP, 4.04 mM $MgCl_2$, and 20% glycerol. All incubations were done on ice (at 4^0C).

Mg^{2+} Titration Experiments

A set of four 1X ATP buffer solutions (see above) containing 1.7, 3, 5, and 7 mM total $MgCl_2$ were prepared for the study. 45 µM Rca sample solution was prepared by mixing 50 nM labeled Rca with 44.95 µM unlabeled Rca following similar dilution protocol as mentioned above.

ATP/ADP Titration Experiments

Both labeled and unlabeled stock solutions for this experiment were prepared by mixing appropriate amount of thawed proteins in ATP, and in ADP. For example, 4 µL 60.1 µM labeled stock solution in 1:3 ATP: ADP was prepared by mixing 1 µL of 90.4 µM Rca in ATP with 3 µL of 50 µM Rca in ADP. A 60 µM Rca sample solution was prepared by mixing 50 nM labeled Rca with 59.95 µM unlabeled Rca following similar dilution protocol as mentioned above. Nucleotide composition was varied by changing the dilution buffer. The buffers had all the ingredients in common except their nucleotide composition which is given by the following. 2 mM ATP, 1.5 mM ATP + 0.5 mM ADP, 1 mM ATP + 1 mM ADP, 0.5 mM ATP + 1.5 mM ADP, and 2 mM ADP. All incubations were done on ice.

WT Rca in Presence of ATP-γ-S

Same as protocol 1 except the 1X buffer contained 2 mM ATP-γ-S instead of 2 mM ATP. For the time series experiment, 45 µM wt Rca sample solution was prepared by mixing labeled and unlabeled wt protein following similar dilution protocol as mentioned above. All incubations were done on ice.

2.3 Fluorescence Fluctuation Experiments

Description of the Instrument

Fluorescence fluctuation measurements such as FCS and PCH were carried out using a home built single molecule confocal set up. An oil immersion objective (Olympus PlanApo 100X/1.4NA Oil) was used to focus a 532 nm CW laser (Compass 215 m-10 Coherent GmbH, Germany) few microns above the cover slip. A neutral density filter was used to attenuate the laser power to about 50 µW. The same objective was used to collect the emitted fluorescence light which was latter passed through a 50 µm pinhole to reject out of the focus light. A band pass filter (Omega 3RD560-620) was used to filter the fluorescence light from excitation light and background before the emission is detected using silicon avalanche photodiode (SPCM-AQR-14; Perkin-Elmer, Fremont, CA). The fluorescence signal was correlated using an ALV correlator card (ALV 5000/EPP, ALV-GmbH, Germany). A typical FCS measurement took 10 minutes of data acquisition, while the data for PCH histogramms were acquired using a PCI-6602 acquisition card (National Instruments, Austin, TX) with 10 µs resolution. Perfusion chambers (Grace BioLabs) were used as sample holders, and were pretreated with 0.1 mg/ml BSA (New England BioLabs) to reduce non specific adsorption of Rca on cover glass.

FCS Data Analysis

A detailed description of the theory of FCS can be found in the introduction (chapter 1). For FCS measurements, the instrument was calibrated each day for estimating the confocal volume parameters r_0 and z_0. This was done by measuring the

FCS decays of free TAMRA dye and/or free Alexa-546 dye, and fitting the resulting FCS decay with known diffusion coefficients of either TAMRA (D = 414 $\mu m^2 s^{-1}$, [3, 4]) or alexa dye (D = 341 $\mu m^2 s^{-1}$, [5]) according to eq. 1.4.3 to estimate the confocal parameters. Measurements with Rca were done following calibration and, the calibrated confocal parameters were used to fit the resulting data.

PCH Data Analysis

A detailed description of the theory of PCH can be found in the introduction (chapter 1). PCH histograms were calculated using Matlab, and were fit with a custom made χ^2 minimization routine on Matlab following an algorithm described elsewhere. This routine uses the $\langle N \rangle$ calculated from the amplitude of the FCS auto correlation function as a fixed parameter and optimizes for the brightness, ε. The absolute brightness values were converted to relative brightness scale, by dividing then with the absolute brightness of the free alexa 546 C_5 maleimide dye measured at the same laser power.

Diffusion Coefficients of Monomeric and Oligomeric Species

The absolute diffusion coefficients (D_{app}) obtained from fitting the FCS curves for Rca were converted to a relative scale for easier comparison of the data over a number of trials. In this normalization, all the absolute diffusion coefficients were divided by the diffusion coefficient of the monomer (D_1) measured at 50 nM Rca. This produced a set of D_{app}/D_1 values, which were latter interpreted using theoretical models. For, interpretation of the FCS results a set of D_{app}/D_1 were calculated using a specific association model (see chapter 3 for details). The theoretical diffusion coefficients D_{app} for Rca oligomers were obtained using two different approaches. In the first approach, an

experimental monomeric diffusion coefficient obtained from measurements on 50 nM Rca was used, and the Stokes-Einstein relationship was used to calculate the diffusion coefficients of other higher oligomers. The Stokes-Einstein relationship predicts that for spherical oligomers with constant specific volume, the diffusion coefficient changes as $D_k = D_1/k^{\frac{1}{3}}$, where k = 2,4,6…is the size of the oligomer. The interpretation of our experimental data is not significantly influenced but considering the effects of a non spherical particle on the diffusion coefficient, as explained in detail in the appendix. In an alternative approach, the diffusion coefficients were calculated from the radius of gyration R_g of different oligomeric states form the co ordinates of the reconstructed closed-ring hexamer of tobacco Rca (pdb ID code 3ZW6) [6] as [7]

$$R_g^2 = \frac{1}{N}\sum_{k=1}^{n}(\vec{r} - \vec{r}_{mean})^2 \qquad \text{Eq. 2.3.3}$$

Separate models for the monomer, dimer, trimer and tetramer consisted of the coordinates of one, two, three or four adjacent subunits respectively. The diffusion coefficient, D was calculated from Stokes-Einstein's equation (see chapter 1 eq. 1.4.1) as

$$D = \frac{k_B T}{6\pi\eta}\left(\left(\frac{5}{3}\right)^2 \frac{{R_g}^3}{0.7674} + \frac{3M_w}{4\pi N_A \delta_{water}}\right)^{-\frac{1}{3}} \qquad \text{Eq. 2.3.4}$$

Where, T is taken as 293K, η is the viscosity of the solution (taken as pure water) and k_B is Boltzmann's constant.

The first summand in the parenthesis takes into account that the structural models comprise 76.54 % of the mass of the full length protein, and that the physical radius of a sphere is$(5/3)^{\frac{1}{2}}R_g$ [7]. The contribution of hydration is represented in the second. Here, the M.W. of the protein is given by M_w, N_A is Avogadro's number, δ_{water} is the density

of water, and h is the degree of hydration (typically 0.2-0.6 gm water/gm protein [8]). The hydration was fixed to 0.4, because this parameter has only minimal effect to our calculation and do not affect the data interpretation (see appendix).

References

1. Salvucci, M.E., *Potential for interactions between the carboxy- and amino-termini of Rubisco activase subunits.* FEBS Lett, 2004. **560**(1-3): p. 205-9.

2. Barta, C., A.E. Carmo-Silva, and M.E. Salvucci, *Purification of Rubisco activase from leaves or after expression in Escherichia coli.* Methods Mol Biol. **684**: p. 363-74.

3. Gendron, P.O., F. Avaltroni, and K.J. Wilkinson, *Diffusion coefficients of several rhodamine derivatives as determined by pulsed field gradient-nuclear magnetic resonance and fluorescence correlation spectroscopy.* J Fluoresc, 2008. **18**(6): p. 1093-101.

4. Muller, C.B., et al., *Precise measurement of diffusion by multi-color dual-focus fluorescence correlation spectroscopy.* EPL, 2008. **83**(4): p. 46001.

5. Petrasek, Z. and P. Schwille, *Precise measurement of diffusion coefficients using scanning fluorescence correlation spectroscopy.* Biophys J, 2008. **94**(4): p. 1437-48.

6. Mueller-Cajar, O., M. Stotz, and A. Bracher, *Maintaining photosynthetic CO2 fixation via protein remodelling: the Rubisco activases.* Photosynth Res. **119**(1-2): p. 191-201.

7. Rubinstein, M. and R.H. Colby, *Polymer physics*. 2003, Oxford: Oxford University Press. xi, 440 p.

8. Squire, P.G. and M.E. Himmel, *Hydrodynamics and protein hydration.* Arch Biochem Biophys, 1979. **196**(1): p. 165-77.

RESULTS

3.1 Development of Self-Association Models of Rca

We have investigated the assembly of Rca at pH 7.6 in a buffer containing 2 mM ADP and 5 mM Mg^{2+} using fluorescence fluctuation based methods such as PCH and FCS. For that reason, we produced a fluorescently labeled cotton β-Rca-378AC by conjugating an engineered cysteine residue [1] with a maleimide functionalized alexa-546 fluorophore. The mutant version of the 380 residue Rca was produced by inserting an Ala-Cys after residue 378 [1], which places the label at 20 residues downstream of the C-terminus of the AAA+ X-ray model [2] (see appendix I, fig. A.1.1).

The reported ATP-ase and Rubisco reactivation activity of this variant were 81% and 53% of the wt protein, respectively, although these values went up to 150% and 131% following a chemical modification [1]. Consistent with previous reports [1], MALDI spectra (see chapter 2, fig. 2.1.1) showed a single species with appropriate M.W. Dye to protein molar ratio was found to be 1.04 ± 0.08 (n = 4) from the absorbance scans collected from the HPLC purified denatured protein (see appendix I, fig. A.1.3,4). This part of the work was done in the laboratory of Dr. Rebekka Wachter by Agnieszka Kuriata.

The fundamental working principle of the biophysical techniques used in this study, namely FCS and PCH, is based on the fluctuation in the fluorescence signal under equilibrium conditions. The amplitude of this fluctuation is inversely proportional to the square root of the number of molecules, $\langle N \rangle$, present in the observation volume. Hence, the number of molecules is required to be small in order to have large fluctuation

amplitude relative to the mean intensity. This puts an upper limit of approximately 300 nM on the concentration of the labeled Rca that can be used for this study. In order to access higher concentrations we have mixed unlabeled and labeled Rca while keeping the concentration of labeled Rca constant at 50 nM. This strategy works under the assumption that unlabeled and labeled subunits equilibrate randomly in a mixture to produce oligomers consisting of varying amount of fluorescent subunits. The oligomerization and aggregation of a wide variety of proteins such as tubulin [3], the tumor suppressor p53 [4], barster [5], and α-synuclein [6] have been investigated using this strategy of mixing. Although PCH analysis becomes greatly complicated for such mixtures, the diffusion properties of the oligomers can be estimated using FCS analysis.

Rca Exists as a Monomer at Sub-Micormolar Concentrations:

FCS experiments were carried out on fully labeled Rca at concentrations 50-300 nM. The diffusion coefficients were obtained from fitting the FCS data at each subunit concentration according to eq. 2.3.2 (see chapter 2). The average diffusion coefficient value at 50 nM concentration obtained from fitting ten independent measurements is D_{50nM} = 64.7 ± 3.7 $\mu m^2 s^{-1}$. At other concentrations, the diffusion coefficient values were obtained from an average of four independent experiments and were found to be indistinguishable from D_{50nM} within experimental error (see appendix I, fig. A.1.2). Additionally, a plot of the mean number of particles in the observation volume, obtained from the amplitude of the FCS auto correlation curves as a function of Rca subunit concentration, was also found to be linear, as expected for a monodisperse solution (see appendix I, fig. A.1.2). Oligomerization will result in a decrease in the particle number with increasing subunit concentration resulting in a downward curvature in this plot. This

result tells us that Rca subunits do not form oligomers at concentrations between 50-300 nM, and consequently the oligomeric state of Rca remains unchanged.

In order to find the oligomeric state of Rca at these concentrations, we compared the experimentally determined values with a diffusion coefficient calculated from the R_g value of a single subunit. The R_g value was estimated from the crystallographic model [2], and the monomeric diffusion coefficient was calculated to be 59.1 $\mu m^2 s^{-1}$ at 20^0C (see chapter 2). Self association will always reduce the diffusion coefficient, and since the experimental value is larger than the calculated value, this comparison provides evidence that Rca is monomeric at 50-300 nM concentration range. Presence of monomers as the single assembly state at these concentrations is further supported from the PCH analysis of the data. PCH histograms depend on two parameters, namely the mean number of particles in the observation volume, $\langle N \rangle$, and the molecular brightness (ε). The latter is defined as the average photon count detected per second per molecule and is directly proportional to the number of fluorescent labels present in each molecule. Since each Rca subunit is singly labeled with one fluorophore, ε is expected to increase proportionately with the degree of oligomerization. Thus, under similar conditions, the Rca dimer will be twice as bright as a Rca monomer.

Although there is no analytical solution for PCH equations, the histogram can be calculated numerically form the parameters $\langle N \rangle$, and ε [7]. The ε value at each Rca concentration is obtained by fitting the PCH histogram numerically while fixing the $\langle N \rangle$, at a constant value obtained from the amplitude of their respective auto correlation functions.

For comparing the molecular brightness of Rca solutions with that of the individual labels, the ε value for free dye solution (ε_{FD}) was experimentally determined in an analogous way. Assuming that conjugating the dye with the protein does not change the fluorescence quantum yield and the molar extinction coefficient of the dye, a ratio of the molecular brightness of Rca and that of the free dye ($\varepsilon/\varepsilon_{FD}$) provides a direct measure of the oligomerization state of the protein. These ratios all the Rca concentrations in the range 50-300 nM are plotted in fig. A.1.2 (appendix I). As can be seen from the figure, over the given concentration range the ratios remain constant at an average value of 0.8 within the experimental error. There is a slight reduction in the measured brightness value of the free labels compared to the Rca, this could be explained by a minor decrement in the product of the molar extinction coefficient and the fluorescence quantum yield of the dye upon conjugation to the protein. However, since oligomerization is expected to result in ratios greater than one, the observed ratios are consistent with the monomeric Rca.

Rca Oligomerizes within the 1-10 µM Concentration Range, and Large Complexes Form at Higher Concentrations

We have mixed varying amount of unlabeled protein with 50 nM labeled protein to investigate Rca assembly above 300 nM concentration assuming that a proper subunit equilibration will result in a random distribution of labels over all oligomeric forms. Control experiments performed in support of this notion, on 8 µM Rca under varying equilibration times (0-60 min) showed that the results are independent of the time elapsed between sample preparation of measurement. The FCS curves collected on Rca solutions of concentration above ~550 nM made by mixing 50 nM labeled and 500 nM unlabeled

Rca showed a continuous shift toward the longer time scale (fig. 3.1.1 A), indicating the formation of higher order oligomers whose relative proportions and size varied with total protein concentration. Control experiment done using free Alexa 546 maleimide labels in buffer containing 127 μM of unlabeled Rca showed no measurable change in the diffusion coefficient of the free label, eliminating the possibility that the shifts observed with labeled Rca is a result of the changes in the solution viscosity or index of refraction.

In agreement with previous reports [8, 9], our FCS data indicates the formation of supra-molecular Rca complexes significantly larger then hexamer at subunit concentration above 10 μM. Although Rca solutions are highly polydisperse, a one component simple diffusion model (eq.2.3.2, chapter 2) fits the FCS curves really well, and an apparent diffusion coefficient (D_{app}) can be extracted. This allowed us to calculate the ratio D_{app}/D_1 at each concentration regardless the number of contributing species (fig. 3.1.1, B-D). A scale as red horizontal bars to the right side of the graphs showing the expected ratios of D_{app}/D_1 ($k^{-1/3}$ for k = 1…20) for pure oligomeric forms. A ratio of 0.38 was observed for 100 μM Rca which is substantially smaller than 0.55 expected for k = 6, and therefore indicated the possible formation of large aggregate bearing on the order of ~24 subunits. The influence of non-spherical molecular shapes and different amount of bound water to the relative diffusion coefficient of the protein cannot account for this difference (see appendix I).

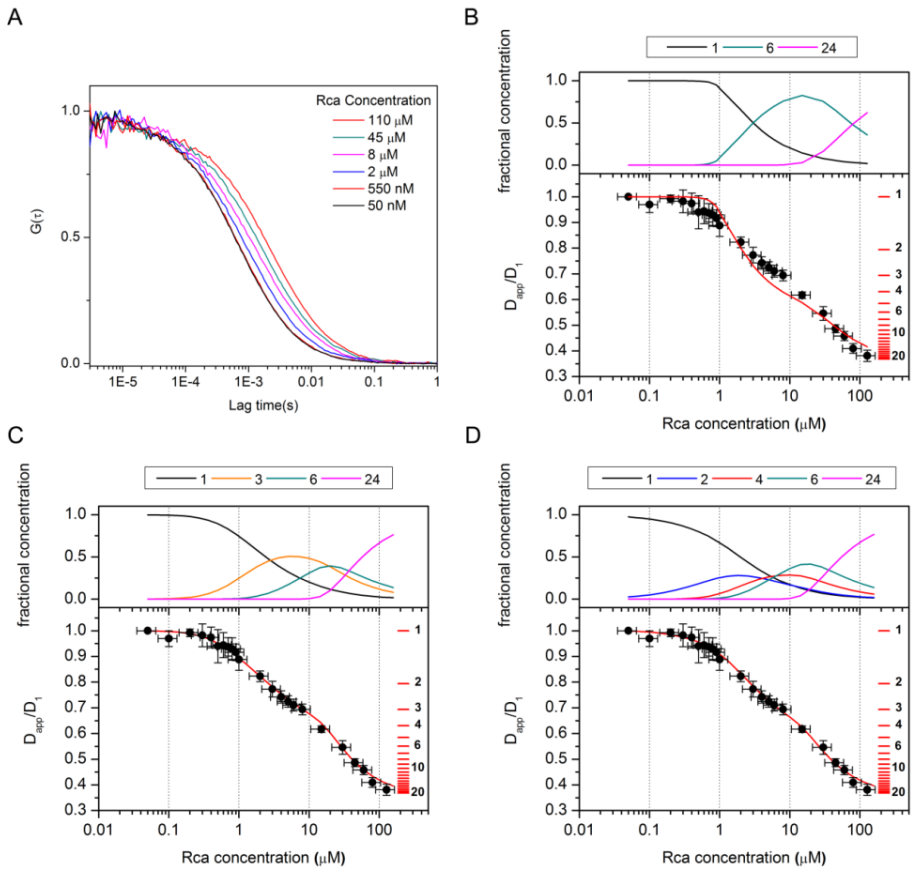

Figure 3.1.1 Rca Assembly Mechanisms. (*A*) Representative FCS decays obtained with 50 nM labeled and increasing concentrations of unlabeled Rca. The concentrations in the inset represent total protein (*labeled and unlabeled*). (*B–D*) Comparison of experimental results and modeling. The solid circles are experimental values of the ratio of the apparent diffusion coefficient at each concentration (D_{app}) and the diffusion coefficient obtained at 50 nM (D_1). The horizontal red lines are placed at values of D_{app}/D_1 ($k^{-1/3}$ for k = 1…20), and represent the expected D_{app}/D_1 values for monomers, dimers, etc. The solid curves were calculated according to Model 1 (panel *B*), Model 2 (panel *C*), and Model 3 (panel *D*) with the K_d values from Table 2.1.1. The concentration profiles above each graph (panels *B–D*) represent the fractional subunit concentrations of the different oligomeric forms assumed to contribute to each model, as calculated from the total Rca concentration and the K_d values in table 3.1.1.

In a similar FCS based method, Rajagopalan et al. [4], investigated the self-assembly of tumor suppressor protein p53. For this protein, the assembly pathway

involved a three state equlibria resulting in tetramers through dimeric intermediate, and in this case the dissociation constants are separated by at least two orders of magnitude. Therefore, the protein solution did not contain any more than two oligomeric forms at any concentrations. Consequently, the graph of diffusion time vs. protein concentration exhibited two clear inflexion points at the monomer-dimer, and at the dimer-tetramer transitions. This permitted the estimation of the K_d directly from this plot without rigorous mathematical modeling [4]. On the other hand, Rca assembly involves a number of intermediates, and we observe a gradual shift in the diffusion constants with protein concentration. Published HPLC data [8-11] also supports this feature. Accordingly, a mathematical model describing the total auto correlation function in terms of the contributions of all oligomeric species at all protein concentrations is required to interpret the FCS data in terms of Rca assembly.

Derivation of the Total Autocorrelation Function to Describe FCS of Polydisperse Solution

The autocorrelation function for a mixture of fluorescent species containing *M* components of well defined diffusion coefficient (D_i) and brightness (ε_i) is given by [12]

$$G(\tau) = \frac{2^{-3/2}\sum_{i=1}^{M} N_i \varepsilon_i^2 g_i(\tau)}{\left(\sum_{i=1}^{M} N_i \varepsilon_i\right)^2} \qquad \text{Eq. 3.1.1}$$

Where

$$g_i = \left(1 + \frac{4D_i\tau}{r_0^2}\right)^{-1}\left(1 + \frac{4D_i\tau}{z_0^2}\right)^{-1/2} \qquad \text{Eq. 3.1.2}$$

is the normalized autocorrelation function of the *i*th species, r_0, z_0 are the radial and the axial semi-axis of the Gaussian observation volume, $\langle N_i \rangle$ is the average number of molecules of the *i*th species in the observation volume. Usually, eq. 3.1.1 depends on the

diffusion coefficients of all the oligomeric species present in the solution and the dissociation constants associated with each oligomeric equilibria.

Regardless of the complexity of eq. 3.1.1, the experimental FCS decays can be fitted with a one component FCS diffusion model (eq. 2.3.2, chapter 2) in order to extract an apparent diffusion coefficient (D_{app}) (see appendix I for a detailed description). This implies that a total autocorrelation function produced by the linear combination of multiple one component decays is experimentally indistinguishable from that obtained for a monodisperse sample. However, it should also be noted that the D_{app} is not the same as the average diffusion coefficient of all the oligomers for the reason that each species contributes as the square of their brightness to the total auto correlation function. For example, the contribution of a dimer carrying two labels to $G(\tau)$ is four times as much as the monomer carrying only one label.

In figs. 3.1.1, B-D, the D_{app} obtained from fitting the experimental FCS curves to eq. 2.3.2 were converted to a relative scale by taking the ratio of D_{app} with the diffusion coefficient of a monomer D_1 measured at 50 nM Rca. The error bars in the plot represent standard deviations of at least four independent measurements. For the purpose of developing a theoretical assembly model which can explain the experimental D_{app}/D_1 ratios, eq. 3.1.1 needs to be adjusted so that the brightness is expressed in terms of the oligomeric state of the protein and the number of labeled subunits in each assembly state. The brightness ε_i of each oligomer is proportional to the number of labeled subunits present in the oligomeric species. For a protein oligomer containing k subunits, we can rewrite eq. 3.1.1 as

$$G(\tau) = \frac{2^{-3/2}\sum_k \sum_{n=0}^{k} n^2 N_{k,n} g_k(\tau)}{\left(\sum_k \sum_{n=0}^{k} n N_{k,n}\right)^2} \quad \text{Eq. 3.1.3}$$

Where $N_{k,n}$ is the mean number of particles in the observation volume containing k subunits, out of which n subunits are fluorescently labeled, and $g(\tau)$ is the normalized autocorrelation function as defined in eq. 3.1.2. Yu et al.[13] discussed a model analogous to eq. 3.1.3 for the purpose of analyzing FCS decays of micelles containing a variable number of fluorophores, but in this work only the autocorrelation amplitudes were examined by the authors. A single diffusion coefficient was used for all the micelles. As a result of mixing labeled and unlabeled proteins in a given oligomeric particle, the labeled subunits gets randomly distributed according to binomial distribution. Therefore, the probability that an oligomer of size k containing n labeled subunits is given by,

$$p_{k,n} = \binom{k}{n} f^n (1-f)^{k-n} = \frac{k!}{n!(k-n)!} f^n (1-f)^{k-n} \quad \text{Eq. 3.1.4}$$

Where f is the fraction of fluorescently labeled subunits, which is given by the ratio of the concentration of the labeled protein (C_L) to the total protein concentration in a mixture; $f = C_L/(C_L + C_U)$. The $N_{k,n}$ value is then given by $p_{k,n}N_k$, where $N_k = \sum_{n=0}^{k} N_{k,n}$ is the mean number of particle in the observation volume of size k, containing up to n labeled subunits. We can express N_k in terms of the molar concentrations as $C_k V_{conf} N_A$, where C_k is the concentration of the oligomer containing k subunits, $V_{conf} = \left(\frac{\pi}{2}\right)^{3/2} r_0^2 z_0$, is the effective observation volume expressed in liter, and N_A is the Avagadro's number. The C_k values are determined from the total protein concentration

$(C_L + C_U)$ and the dissociation constants associated with different oligomerization equiliabria.

To this point, the total autocorrelation function, expressed in terms of the concentrations of the labeled and unlabeled Rca $(C_L + C_U)$, concentrations (C_k) and the diffusion coefficient of each oligomeric states (D_k) present in the solution, and the optical parameters (r_0, and z_0) of the observation volume, can be written as,

$$G(\tau) = \frac{\sum_k \sum_{n=0}^{k} n^2 \binom{k}{n} f^n (1-f)^{k-n} C_k \left(1+\frac{4D_k\tau}{r_0^2}\right)^{-1} \left(1+\frac{4D_k\tau}{z_0^2}\right)^{-1/2}}{\left(\frac{\pi}{2}\right)^{3/2} r_0^2 z_0 N_{AV} * \left(\sum_k \sum_{n=0}^{k} n \binom{k}{n} f^n (1-f)^{k-n} C_k\right)^2} \qquad \text{Eq. 3.1.5}$$

We estimated the values for D_k from the x-ray structure of tobacco Rca (see chapter 2), and this leaves C_k as the only unknown parameter in eq. 3.1.5, with its values depending on the dissociation constants (K_ds), and the total Rca concentration. Therefore, a previous knowledge of the oligomeric proportions of Rca at different concentrations and the mechanism through which each oligomers are formed is essential in order to explain the FCS results. Since this information is limited for Rca, different Rca assembly models can be tested for their consistency with the experimental data (table. 3.1.1). For this purpose, at first, we assumed different assembly models each involving a set of oligomers in equilibrium. The type of oligomers involved in each model was chosen by assuming a set of k values. We also assumed a set of K_d values associated with different equilibrium processes in a select model. In the next step we used these K_d values to calculate the concentration of each oligomeric species (C_k) as a function of the total concentration of Rca $(C_L + C_U)$. Subsequently, the C_k values were fed into eq. 3.1.5 in order to predict a theoretical auto correlation function at each Rca concentration. Analogous to the treatment of the experimental FCS curves, each theoretical FCS curves were fitted with

eq. 2.3.2 (see chapter 2), and a calculated D_{app} is extracted that explains the FCS decay of a multi-component solution. The relative apparent diffusion coefficient (D_{app}/D_1) values corresponding to the assumed mechanism were then plotted (fig. 3.1.1, *B-D*, solid red lines) against the total protein concentration $(C_L + C_U)$, and compared to the experimental data. The dissociation constants are then modified iteratively up to the point when the calculated D_{app}/D_1 values matched the experimental results within error bars.

Explanation of Experimental FCS Results in Terms of Alternative Assembly Mechanisms of Rca.

To this date the Rca assembly mechanism is only poorly characterized, however there is some information available on subunit stoichiometry. Dimeric forms of Rca has been observed using SE-HPLC in the laboratory of Dr. Rebekka Wachter (unpublished results), and hexameric forms of Rca has also been reported recently by mass spectrometry and EM [2, 14, 15]. In addition, the classic AAA+ domains are well known to form hexameric structures. These observations, all together strongly support the presence of a hexamer as an intermediate in the Rca assembly. For this reason, we have included a hexamer as an intermediate in the assembly models; we have used to describe the experimental FCS results. We considered three different assembly models; Model1 (monomer-hexamer-24 mer), Model 2 (monomer-trimer-hexamer-24 mer), and Model 3 (monomer- dimer-tetramer-hexamer-24 mer) (Table 3.1.1). In figs. 3.1.1, B-D, we have plotted the calculated D_{app}/D_1 values based on these models together with our experimental date. We have also provided the fractional concentrations $kC_k/\sum_k kC_k$ of each oligomers calculated from the predicted K_d values (top panels above each graph).

Table 3.1.1. Optimized Dissociation Constants for ADP Mediated Assembly. Dissociation constants (K_d) for each assembly step were obtained by modeling according to eq. 3.1.5. Model 1 is judged to be inconsistent with experiment, whereas Models 2 and 3 provide good fits to the data.

Model	Equilibria	$K_d$values
1	$6Rca \rightleftharpoons Rca_6$	50 μM^5
	$4Rca_6 \rightleftharpoons Rca_{24}$	10^3 μM^3
2	$3Rca \rightleftharpoons Rca_3$	5 μM^2
	$2Rca_3 \rightleftharpoons Rca_6$	5 μM
	$4Rca_6 \rightleftharpoons Rca_{24}$	35 μM^3
3	$2Rca \rightleftharpoons Rca_2$	3.5 μM
	$2Rca_2 \rightleftharpoons Rca_4$	1 μM
	$Rca_4 + Rca_2 \rightleftharpoons Rca_6$	1 μM
	$4Rca_6 \rightleftharpoons Rca_{24}$	25 μM^3

The calculations, done using model 1 and eq. 3.1.5, predicts a sharp decrease in the D_{app}/D_1 values as shown by the red curve in Fig. 2.1.6, B, which is calculated using K_{d1} = 50μM^5 K_{d2} = 10^3 μM^3. However, the experimental values (fig. 3.1.1, B, solid circles) decrease rather smoothly at the low concentration range which indicates the formation of intermediate species. Although a better fit to the experimental data at very low concentration values can be obtained by reducing K_{d1} value, but this adjustment would result in a drop in the D_{app}/D_1 values to ~0.6 around 1 μM Rca, whereas the

experimental value is ~0.9 at the same concentration. Therefore, Model 1 is regarded as inconsistent with the experimental data.

The smooth decrease of the observed D_{app}/D_1 values can only be interpreted theoretically in terms of intermediate oligomeric states; and therefore we have included a trimer as an intermediate in our next model 2. The theoretical D_{app}/D_1 values calculated using this model was found to be very compatible with the observed results and a best match can be obtained by using the dissociation constants of 5 μM^2, 5 μM, and 35 μM^3 for K_{d1}, K_{d2}, and K_{d3} respectively (table 3.1.1 and fig. 3.1.1, C). We estimated the uncertainties in dissociation constants by evaluating the range of K_{d1} values that produce results consistent with experimental values. The results of these tests are shown in figure A.1.9 A (appendix I); as can be seen from the figure, K_{d1} values within the range 3.5-10 μM^2 produces a good match with the experimental data within the experimental error. The adjusted values for K_{d2} and K_{d3} corresponding to the lower and the upper limit of K_{d1} were K_{d2} = 15 μM and K_{d3} = 2 μM^3 for K_{d1} = 3.5 μM^2, and K_{d2} = 1.3 μM and K_{d3} = 70 μM^3 for K_{d1} = 10 μM^2. This shows that a trimeric intermediate alone can explain the FCS results adequately.

Although Model 2 provides an adequate description of the experimental data, we have also considered an additional model based on our previous observation of dimeric intermediates form the SE-HPLC data. In this third model we replaced the trimer with a dimer and a tetrameric intermediates and observed that D_{app}/D_1 values calculated using K_{d1} = 3.5 μM, K_{d2} = 1 μM, K_{d3} = 1 μM, and K_{d4}= 25 μM^3 are in very good agreement with the observations (fig. 3.1.1, D). Owing to the incorporation of an additional intermediate and hence an extra adjustable parameter, model 3 is more flexible compared

to other models, and wide combination of K_d*'s* produce equally good fit to the experimental data. For example, in fig. A.1.9 B (appendix I), the experimental data can be fit really well with the ones calculated using K_{d1} values within the range 2-20 μM with subsequent modification of other K_d*'s* (K_{d2} = 2 μM, K_{d3} = 1 μM, and K_{d4} = 20 μM^3 for K_{d1} = 2μM, and K_{d2} = 0.03 μM, K_{d3} = 2 μM, and K_{d4} = 8 μM^3 for K_{d1} = 20 μM).

The corresponding concentration profiles obtained for this set of dissociation constants display more variations then model 2. This is because of the fact that our observations can be adequately explained by one less intermediate species (model 2). We did not observe a clear plateau even at the highest concentration we measured. This indicates the presence of higher oligomeric states in equilibrium with the assemblies of approximately 24 subunits. A precise determination of the M.W. of these larger oligomeric states is not possible and for that reason we suggest that hexameric Rca from assemblies of higher order oligomers incorporating as many as 24-mers (fig. 3.1.2). Admittedly, owing to the uncertainties inherent in our experiments, the distinction between 18 and 24-mers is hardly possible (fig. 3.1.1, B-D red horizontal lines), yet we cannot exclude that fact that larger species are formed by continuous addition of dimmers to smaller oligomers ($Rca_k + Rca_2 = Rca_{k+2}$) leading to the growth of Rca in a spiral arrangement, as seen in the Rca AAA+ crystal structure [2] (fig. 3.1.2).

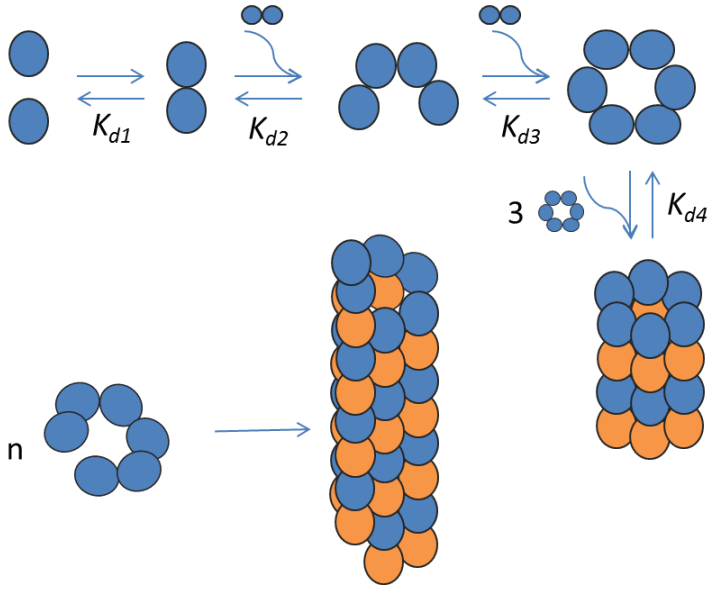

Figure 3.1.2. Schematic Representation of the Rca Assembly Model. This model is consistent with experimental results: It consists of a dimer and a tetramer as intermediates before the formation of a hexamer. Higher order assemblies are formed as stacking of hexameric rings.

3.2 Nucleotide Effects on the Rca Oligomeric Equlibria

In the previous section of this chapter, we proposed a self-association model of wt Rca and estimated associated thermodynamic dissociation constants. We found that the assembly of Rca is non-cooperative in presence of ADP-Mg^{2+}, and involves multiple intermediates. Our experimental data also suggested that Rca ultimately grows in a spiral arrangement at high μM concentrations, consistent with other observations.

In a successive approach toward a complete description of the thermodynamics of Rca self-assembly, we produced a functionally impaired mutant version of Rca and investigated its self assembly in presence of ATP-Mg^{2+}, a mixture of nucleotides, and have also examined the effect of Mg^{2+} binding upon the assembly of Rca. Rca belongs to the AAA family of the ATP-ases, and it hydrolyzes ATP at a turnover rate of 3.8 min^{-1} (fig. 2.1.2, chapter 2) in presence of 4 mM ATP, making it difficult to characterize the assembly in presence of ATP using the wt protein. For this reason, we produced a mutant version of the recombinant protein by changing the aspartic acid residue with an asparagine residue at position 173 in the Walker B motif of the AAA domain [16]. The ATP-ase activity of this mutant protein (D173N) was measured and was found to be 0.368 turnovers/min in presence of 4 mM ATP (fig. 2.1.2, chapter 2).

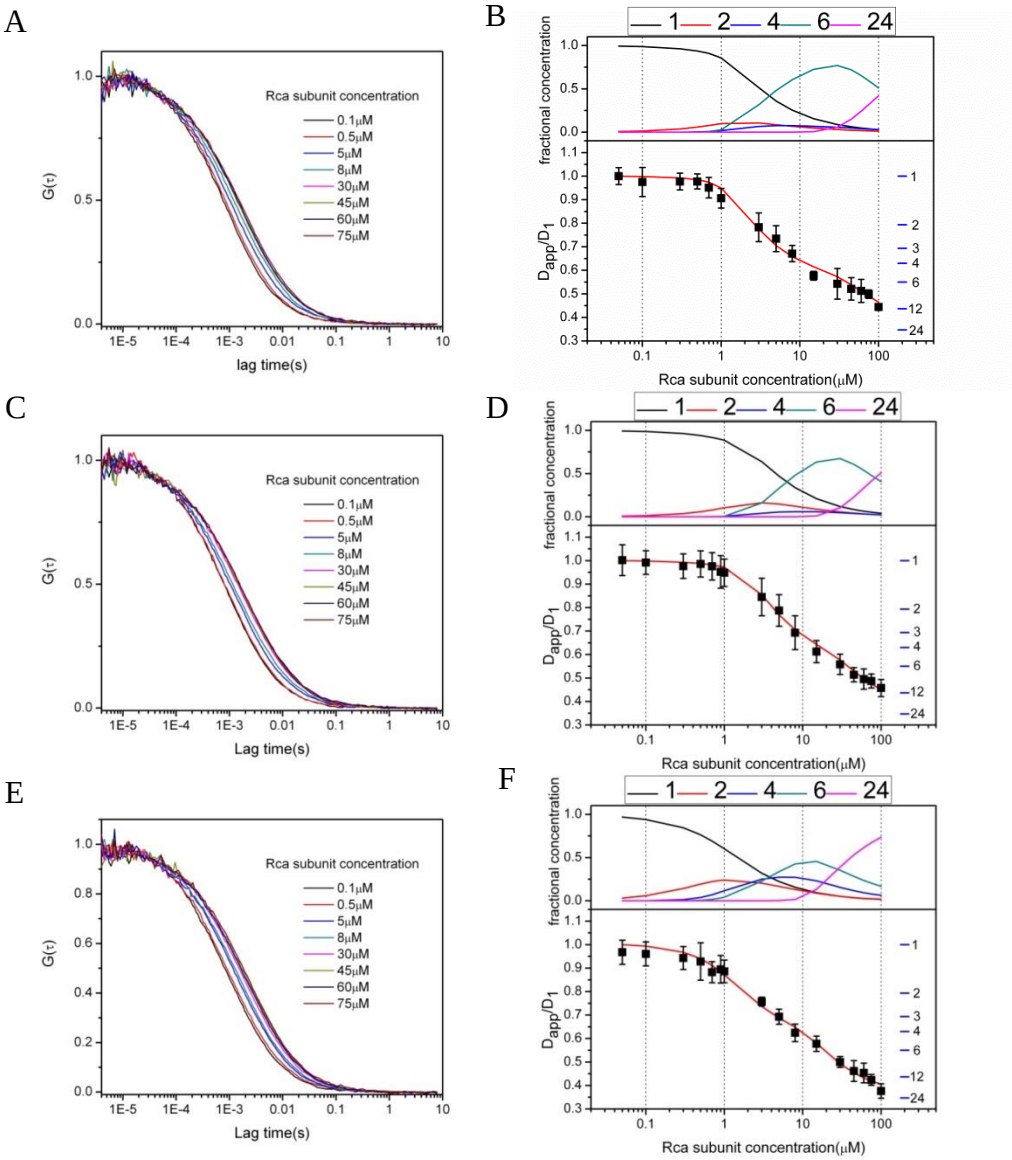

Figure 3.2.1 Rca Assembly Mechanisms Under Different Nucleotide Conditions: Representative FCS decays obtained using 50 nM labeled Rca and increasing amount of unlabeled Rca in presence of 2 mM ATP, and 5 mM Mg^{2+} (A), 1.5 mM ATP, 0.5 mM ADP, and 5 mM Mg^{+2} (C), and 1.5 mM ATP, 0.5 mM ADP, and 2.02 mM Mg^{2+} (E). The concentrations in the inset of the figures correspond to the total subunit concentration (labeled + unlabeled) (B, D, and F). Comparison of the experimental (black squares) and the calculated (red line) results according to the model in fig. 3.2.2. The solid squares are the experimental values of the relative apparent diffusion coefficient (D_{app}/D_1) obtained by taking the ratio of the apparent diffusion coefficient at each Rca subunit concentration (D_{app}), and the diffusion coefficient obtained at 50 nM (D_1). The horizontal blue lines are placed at values of $D_{app}/D_1 = k^{-1/3}$ for k = 1-4, 6, 12, and 24; which represent the

expected D_{app}/D_1 values for monomers, dimers, etc. The solid red curves calculated according to the model using K_d values given in Table 3.2.1 to match the experimental Rca assembly in presence of 2 mM ATP, and 5 mM Mg^{2+} (B), 1.5 mM ATP, 0.5 mM ADP, and 5 mM Mg^{2+} (D), and 1.5 mM ATP, 0.5 mM ADP, and 2.02 mM Mg^{2+} (F). The top panel in each figure shows the evolution of the fractional concentration of each oligomeric species as they appear in the model, which were calculated from the total Rca concentration and the K_d values.

FCS experiments were done by mixing labeled and unlabeled protein while the concentration of the labeled protein held constant at 50 nM, and the amount of unlabeled protein were varied to access a wide concentration range without compromising the sensitivity of the technique. A more comprehensive rationale behind the use of this technique is given in the previous section. FCS experiments were performed over the concentration range 50 nM-100 µM in terms of total Rca subunit concentration. At each Rca subunit concentration, the measured FCS curve is fitted with the one component FCS diffusion equation (Eq. 3.2.1) and apparent diffusion coefficient (D_{app}) is extracted.

$$G = G(0)\left(1+\frac{4D\tau}{r_0^2}\right)^{-1}\left(1+\frac{4D\tau}{z_0}\right)^{-\frac{1}{2}} \qquad \text{Eq. 3.2.1}$$

The diffusion coefficient obtained using 50 nM fully labeled Rca was 53 ± 2 $\mu m^2/s$. The measured diffusion coefficient was also found to be unchanged within experimental error for concentrations up to 700 nM total Rca. This suggests that the oligomerization state of Rca remains unchanged at these concentration ranges. Moreover, this value is very close to the diffusion coefficient (59.1 $\mu m^2/s$) calculated for an Rca monomer based on a crystallographic model [2]. This suggests that Rca monomer dominates at sub-µM concentrations. Although it is important to mention that the measured diffusion coefficient is slightly lower than the calculated value, it can be attributed to the inherent

uncertainties of the experimental determination. Nevertheless, we compared the number of particle in the excitation volume and average fluorescence intensity of the mutant protein with the wt protein in presence of ADP and found matching results (see appendix II for a detailed analysis). This analysis rules out the possibility of any mutation induced changes in the assembly pathway of the protein.

The apparent diffusion coefficient measured at each concentration is then divided by the average monomeric diffusion coefficient at 50 nM ($D_1 = D_{50nM}$ = 53 μm^2/s) to represent the results in a relative scale of diffusion coefficients (D_{app}/D_1). The experimental data is plotted in fig. 3.2.1 (black squares). The error bars represent the standard deviation of at least three separate determinations. A scale of expected relative diffusion coefficients (D_{app}/D_1) for oligomers of size k = 1-4, 6, 12, and 24 is shown as the blue horizontal bars to the right of the plot. This plot shows how Rca subunits associate to form oligomers of different order in a concentration dependent manner, a noticeable plateau arises in the 30-75 μM concentration range, indicating the significant stabilization of a particular oligomeric state. An average of relative diffusion coefficient (D_{app}/D_1) values of these concentration points is found to be 0.54, which is very close to the expected value for a hexamer (0.55), as can be read from the scale (blue horizontal bars). This observation is in striking difference with the reported self-association equilibria of the wt-Rca in presence of ADP-Mg^{2+}, where a continuous assembly into higher oligomers was observed (larger than hexamers) with no indication of a clear plateau (fig. 3.1.1).

To this end, we interpreted our experimental FCS results in terms Rca assembly model discussed in the previous section. A detailed theoretical description of the model

can be found there, but in a nutshell, the assembly model is constructed as the following. The self-association of monomeric subunits can be thought to take place in steps involving three intermediates such as a dimer, a tetramer, and a hexamer leading to a large aggregate roughly the order of a 24-mer. The corresponding dissociation constants pertinent to each equilibria are then given by K_{d1-4} respectively (table 3.1.1). The concentrations of individual oligomeric species are obtained by solving these equations using a set of K_d values. As a result of mixing labeled and unlabeled Rca for our experiments, the relative fractions of individual oligomeric units bearing n labeled subunits (where n is $1:k$; k being the number of subunit in a given oligomer) are calculated from the binomial distribution function (eq. 3.1.4) assuming complete randomization of subunit equilibrium.

$$p_{k,n} = \binom{k}{n} f^n (1-f)^{k-n} = \frac{k!}{n!(k-n)!} f^n (1-f)^{k-n} \qquad \text{Eq. 3.1.4}$$

The number of particles inside the excitation volume, $N_{k,n}$ corresponding to k-th oligomer bearing n labeled subunits is then calculated from their respective total concentrations.

Radius of gyration of each oligomeric species is obtained from the reconstituted crystal structure of tobacco activase and was later adjusted to account for hydration (see chapter 2). The diffusion coefficients (D_k) of each oligomeric species are calculated using the Stokes-Einstein equation assuming a spherical model (see chapter 2, eq. 2.3.4). Finally, a theoretical FCS curve is generated according to (eq. 3.1.5) from the parameters calculated above, which is then fit with the one component diffusion model (eq. 2.3.2, chapter 2) to extract a theoretical apparent diffusion coefficient. The ratio of theoretical apparent diffusion coefficients and the theoretical monomeric diffusion coefficient (as

calculated from the crystal structure [2]) gives the theoretical relative diffusion coefficient which was then compared with the experimental results. The same procedure was repeated for all Rca concentrations, and the K_d values were manually altered until a close match with the experimental result was found (red line in fig 3.2.1 A) concentration profile showing fractional concentrations of all the oligomeric species is also calculated for the optimized K_d value and is plotted in the top panel of (fig 3.2.1)

The optimized set of K_d values corresponding to the red line in fig 3.2.1, based on this model assembly is found to be K_{d1} = 15 µM, K_{d2} = 0.5 µM, K_{d3} = 0.05 µM, and K_{d4} = 3000 µM^3. We have also estimated upper (K_{d1} = 25µM, K_{d2} = 0.5 µM, K_{d3} = 0.05 µM, and K_{d4} = 5000 µM^3, and lower (K_{d1} = 5 µM, K_{d2} = 1 µM, K_{d3} = 0.08 µM, and K_{d4} = 1000 µM^3 bounds of K_d values which also produce well fit to the experimental data within the experimental error. The results of these calculations are given in the appendix II (fig. A.2.5 A, and B). The nature of the K_d values, in particular K_{d3} for tetramer-hexamer equilibrium and K_{d4} for hexamer to 24-mer equilibrium offer important insights. The low K_{d3} (0.05 µM) value suggests that the hexamers are less likely to dissociate and the extra stability might be attributed to formation of a closed ring structure. This is further supported by the very high K_{d4} (3000 µM^3) value which reflects that the formation of higher order oligomers are largely suppressed in presence of ATP. Such closed ring Rca hexamers were also reported before using a functionally impaired Rca (R294V) mutant in presence of slowly hydrolysable ATP analogue ATP-γ-S [2, 15].

ADP is known to bind to Rca tighter then ATP and as a result [15], it would remain bound to Rca after its formation as a product of hydrolysis of ATP by the ATP-ase enzyme Rca. This may bring a change in the active oligomeric structure of Rca, and

influence its functionality. It is proposed that the differential ATP/ADP ratio in the stromata plays a critical role behind the regulation of the activity of Rca between the light and the dark phases of photosynthesis [17, 18].

In order to understand the regulation of Rca activity, we investigated the association pathway of Rca in presence of a mixture of ADP, and ATP at a physiologically relevant proportion of 1: 3, and in presence of 5 mM Mg^{2+} ion. Owing to the fast ATP-ase turnover rate of wt Rca, the same mutant (D173N) Rca was used for this study. Using the same experimental method, and theoretical interpretation of the resulting data (fig. 3.2.1 C) as discussed above, we estimated a set of dissociation constants (table 3.2.1) associated with different oligomerization equilibria as per our self-association model. The values for the dissociation coefficient corresponding to the red line in fig. 3.2.1 C are K_{d1} = 15 µM, K_{d2} = 2 µM, K_{d3} = 0.09 µM, K_{d4} = 1000 μM^3. A comparison of the K_d values with those for the ATP only case indicates nearly identical stability of the different oligomeric species, indicating no change in the oligomeric stoichiometry in presence of high ATP levels. As an estimation of error in the set of dissociation coefficients, we have also calculated an upper and a lower limit of K_d values like the ATP only case (see appendix II fig A.2.5 B).

Table 3.2.1: Optimized Dissociation Constants: Dissociation constants (K_d) for Rca self-association at different nucleotide condition were obtained by modeling according to the model 3 (fig. 3.1.2)

Nucleotide condition	K_{d1}(μM)	K_{d2}(μM)	K_{d3}(μM)	K_{d4}(μM^3)
2 mM ATP, and 5 mM Mg^{2+}	15	0.5	0.05	3000
1.5 mM ATP, and 0.5 mM ADP, and 5 mM Mg^{2+}	15	2	0.09	1000
1.5 mM ATP, 0.5 mM ADP, and 2.02 mM Mg^{2+}	3	0.5	0.5	20

To this end, we further investigated the influence of Mg^{2+} binding on the self-association equilibria and relative stability of different oligomeric forms of Rca in presence of mixture of nucleotides at aforementioned proportions. Each Rca monomer is known to have two Mg^{2+} binding sites, while the first binding site is easily saturated at low ionic strength, a complete saturation of the second binding site can only be achieved at 5 mM total Mg^{2+} concentration. The binding of the second Mg^{2+} is also required for ATP-ase activity of Rca as shown by other studies. In addition to it binding with the protein, Mg^{2+} also binds to the nucleotides, and the binding is rather stronger than its binding with the protein. The dissociation constants for the ADP and ATP complexes are 0.028 mM and 0.241 mM respectively. The amount of free Mg^{2+} available to the protein can then be calculated by solving a set of equations (see appendix II). A plot of the

concentration of the free Mg^{2+} as a function of the total Mg^{2+} can also be found there (fig. A.2.4, appendix II).

In order to investigate the influence of Mg^{2+} ions on Rca self-assembly, at first we carried out a Mg^{2+} titration experiment at a single chosen Rca concentration. The total concentration of the Rca chosen for this titration experiment was 45 µM (0.05 µM labeled + 44.95 µM unlabeled) and the protein solution was prepared in buffers containing different concentrations of Mg^{2+} followed by incubation on ice and FCS data acquisition (see chapter 2). The rationale behind choosing this concentration is that it lies in the susceptible hexameric plateau region in figure 3.2.1 B, which is known to be the functionally active oligomeric from for most of the proteins belonging to this class of the ATP-ases. The apparent diffusion coefficient extracted from each of the FCS curves collected at each Mg^{2+} concentrations are plotted in fig. 3.2.1 A as a function of free Mg^{2+} concentration (see above). The error bars in the figure represent the standard deviation of three independent determinations.

As can be seen from the figure, the apparent diffusion coefficient of the protein increases as the concentration of the free Mg^{2+} available to bind to the protein increases, and it reaches a plateau at about 3 mM free Mg^{2+} or 5 mM total Mg^{2+} concentration. The diffusion coefficient obtained for the lowest ionic strength condition is characteristic of a large oligomeric complex, whereas the highest diffusion coefficient measured at 5 mM free Mg^{2+} is very close to the theoretical diffusion coefficient of hexameric Rca. This result indicates that the binding of the second Mg^{2+} is crucial to the stability of a possible closed ring hexameric complex. The same conclusion can be inferred from an inspection of the set of dissociation coefficients (K_{d1} = 3 µM, K_{d2} = 0.5 µM, K_{d3} = 0.5 µM, K_{d4} =

20 μM^3) obtained from the analysis of the plot (fig. 3.2.1 F) of relative apparent diffusion coefficient (D_{app}/D_1) against the full concentration range. The experimental data (D_{app}/D_1) were collected in an analogous way (see above) for mutant Rca in presence of 15 mM ATP, 0.5 mM ADP, and 2.02 mM Mg^{2+}. Noticeably, there is a tenfold increase in the K_{d3} (tetramer-hexamer equilibria), and fifty-fold decrease in the K_{d4} (hexamer-24mer equilibria), relative to the high Mg^{2+} condition (table 3.2.1 row 3). The change in the dissociation constants depending on the free Mg^{2+} ion concentration suggests that the formation of a stable hexameric form is facilitated in the presence of high Mg^{2+} ion concentration; otherwise Rca forms larger aggregates due to non availability of free Mg^{2+} ion to saturate its second Mg^{2+} binding site.

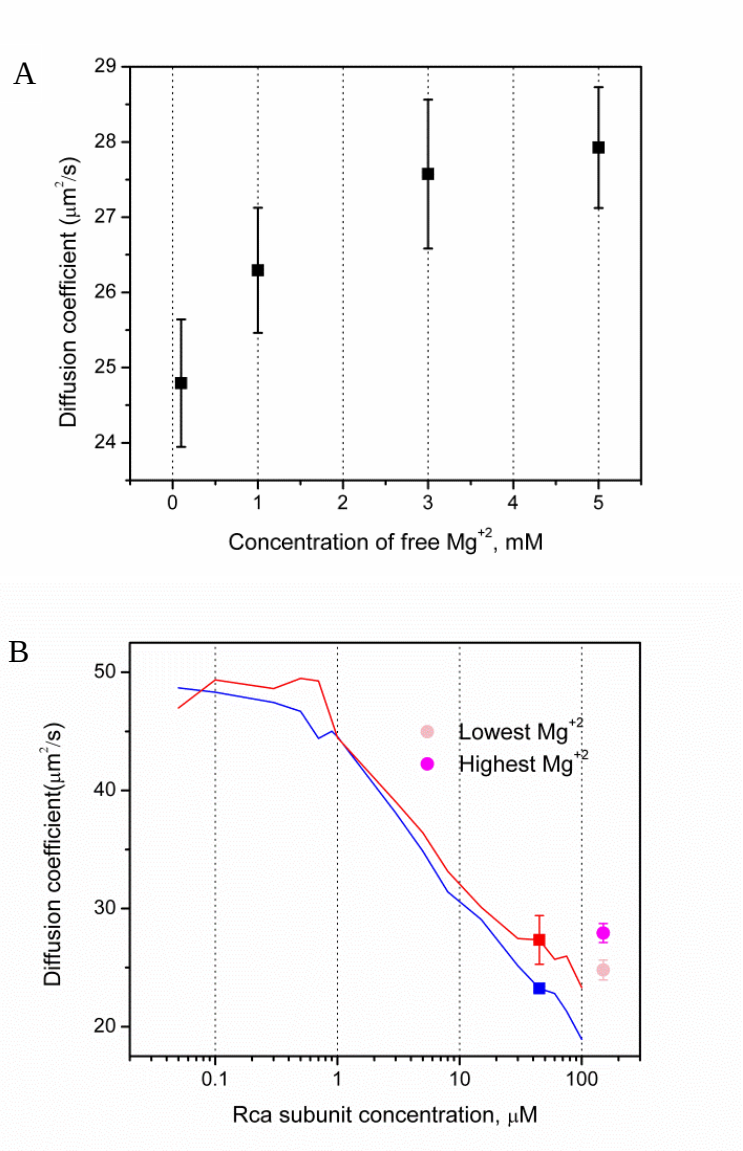

Figure 3.2.3 Mg^{2+} Titration Results: (A) The measured apparent diffusion coefficient (D_{app}) of 45 µM Rca (44.95 µM unlabeled + 0.05 µM labeled protein) in presence of 1.5 mM ATP, 0.5 mM ADP, and increasing concentration of Mg^{2+} ion. The error bars represent standard deviation of experimental determinations. (B) A comparison of the apparent diffusion coefficient (D_{app}) values from the titration experiments with the full range self-association data (*fig 1 B, and F*) of Rca in 2 mM ATP, and 5 mM Mg^{2+} (solid red line); and in 1.5 mM ATP, 0.5 mM ADP, and 2.02 mM Mg^{2+} (solid blue line). The data is plotted in absolute apparent diffusion coefficient (D_{app}) scale for easy comparison with titration data (magenta circles). The titration points are plotted against an arbitrary concentration value to distinguish them from the full range Rca assembly curves (red and blue lines). Only the lowest (light magenta), and the highest (dark magenta) titration points are shown for clarity. The 45 µM points belonging to the full range Rca assembly curves are highlighted as solid squares in respective colors.

References:

1. Salvucci, M.E., *Potential for interactions between the carboxy- and amino-termini of Rubisco activase subunits.* FEBS Lett, 2004. **560**(1-3): p. 205-9.

2. Stotz, M., et al., *Structure of green-type Rubisco activase from tobacco.* Nat Struct Mol Biol. **18**(12): p. 1366-70.

3. Krouglova, T., J. Vercammen, and Y. Engelborghs, *Correct diffusion coefficients of proteins in fluorescence correlation spectroscopy. Application to tubulin oligomers induced by Mg2+ and Paclitaxel.* Biophys J, 2004. **87**(4): p. 2635-46.

4. Rajagopalan, S., F. Huang, and A.R. Fersht, *Single-Molecule characterization of oligomerization kinetics and equilibria of the tumor suppressor p53.* Nucleic Acids Res. **39**(6): p. 2294-303.

5. Sahoo, B., et al., *Protein aggregation probed by two-photon fluorescence correlation spectroscopy of native tryptophan.* J Chem Phys, 2008. **129**(7): p. 075103.

6. Chakraborty, M., et al., *Protein oligomerization monitored by fluorescence fluctuation spectroscopy: self-assembly of rubisco activase.* Biophys J. **103**(5): p. 949-58.

7. Chen, Y., et al., *The photon counting histogram in fluorescence fluctuation spectroscopy.* Biophys J, 1999. **77**(1): p. 553-67.

8. Portis, A.R., Jr., *Rubisco activase - Rubisco's catalytic chaperone.* Photosynth Res, 2003. **75**(1): p. 11-27.

9. Barta, C., et al., *Structural changes associated with the acute thermal instability of Rubisco activase.* Arch Biochem Biophys. **499**(1-2): p. 17-25.

10. Wang, Z.Y., R.T. Ramage, and A.R. Portis, Jr., *Mg2+ and ATP or adenosine 5'-[gamma-thio]-triphosphate (ATP gamma S) enhances intrinsic fluorescence and induces aggregation which increases the activity of spinach Rubisco activase.* Biochim Biophys Acta, 1993. **1202**(1): p. 47-55.

11. Li, C., D. Wang, and A.R. Portis, Jr., *Identification of critical arginine residues in the functioning of Rubisco activase.* Arch Biochem Biophys, 2006. **450**(2): p. 176-82.

12. Lakowicz, J. and N. Thompson, *Fluorescence Correlation Spectroscopy*, in *Topics in Fluorescence Spectroscopy*. 1999, Springer US. p. 337-378.

13. Yu, L., et al., *Determination of critical micelle concentrations and aggregation numbers by fluorescence correlation spectroscopy: aggregation of a lipopolysaccharide.* Anal Chim Acta, 2006. **556**(1): p. 216-25.

14. Mueller-Cajar, O., et al., *Structure and function of the AAA+ protein CbbX, a red-type Rubisco activase.* Nature. **479**(7372): p. 194-9.

15. Blayney, M.J., S.M. Whitney, and J.L. Beck, *NanoESI mass spectrometry of Rubisco and Rubisco activase structures and their interactions with nucleotides and sugar phosphates.* J Am Soc Mass Spectrom. **22**(9): p. 1588-601.

16. Hanson, P.I. and S.W. Whiteheart, *AAA+ proteins: have engine, will work.* Nat Rev Mol Cell Biol, 2005. **6**(7): p. 519-529.

17. Zhang, N., et al., *Light modulation of Rubisco in Arabidopsis requires a capacity for redox regulation of the larger Rubisco activase isoform.* Proc Natl Acad Sci U S A, 2002. **99**(5): p. 3330-4.

18. Zhang, N., P. Schurmann, and A.R. Portis, Jr., *Characterization of the regulatory function of the 46-kDa isoform of Rubisco activase from Arabidopsis.* Photosynth Res, 2001. **68**(1): p. 29-37.

CHAPTER 4

DISCUSSION

Identification of the functional quaternary structure of any protein is often the crucial first step toward a comprehensive understanding of the protein's mechanistic enzymology. How the protein's building blocks are assembled into large functional machines, identification of the transient intermediates, and their evolution as a function of concentration as well as other cellular factors such as presence of nucleotides, ionic strength, and pH poses the biggest experimental challenge toward enzymologists.

Here, we developed a fluorescence fluctuation based method to monitor the association of protein subunits into different oligomeric structures and applied the method to investigate the self-association of Rca. Our methodology tests successfully on this experimentally challenging protein, Rca, which not only forms highly polydisperse solutions, but is also very aggregation prone. We are also able to access a wide concentration range from low nM to high μM by strategically mixing a small fixed quantity of fluorescently marked protein with varying concentrations of unlabeled protein.

We anticipate that this methodology, together with rigorous statistical and mathematical analysis of the experimental data to predict thermodynamic assembly models, will be useful for protein self-association studies, particularly for those involving a dynamic equlibria of fast subunit exchange. We have applied this method to investigate the self-association of Rca which had been intractable over many years [1, 2]. We also looked into the important aspect of the effect of the effect of nucleotides (ATP/ADP) on

the self-association pathway and the overall oligomeric stoichiometry of Rca. We developed an association model based on the oligomeric size estimates obtained from FCS measurements presented here. Our results are consistent with the previously observed ploydisperse nature of Rca in solutions and the concentration-dependent change in the oligomeric stoichiometry.

In the present work, we have investigated the self-assembly of cotton β-Rca in the presence of ADP-Mg^{2+} at pH = 7.6. The results from our FCS and PCH experiments show that Rca exists essentially as a monomer at subunit concentrations below 0.5 μM. This is in agreement with the EM images obtained for amorphous particles at 0.5-1 μM tobacco Rca R293V with Mg^{2+}-ADP [3]. At the highest concentration end (100μM), we observed the formation of high M.W. oligomers comprising roughly of 24 subunits. Since our data show a continuous assembly without any noticeable plateau over any measured concentration range, the size of the intermediate oligomeric states cannot be preciously estimated from the FCS data alone. Therefore, to explain our experimental data, we used prior information from other sources and previously published results. Growing experimental evidence in support of hexameric Rca [3-5], and association models for other AAA+ ATP-ase proteins provide compelling reasons in support of a stepwise assembly model with a hexamer as the focus oligomeric state.

Closed ring Rca hexamers were observed from EM images for a functionally impaired tobacco R294V variant Rca in presence of ATP [3], whereas a spiral hexameric model is supported form the crystal structure of a truncated tobacco Rca [3]. The functional form of the AAA+ classic clade protein that takes part in the ATP-ase cycle are generally hexameric, although spiral structures have also been crystallized alongside

hexamers. The AAA+ domain of FtSH, for example, forms a hexmer when it is associated with the protease [6], whereas a helical arrangement is observed in absence of the protease domain [7]. A related AAA+ protein ClpA assembles through dimmers and tetramers [8, 9] and provides strong rationale for considering dimeric and tetrameric intermediates for the self- association model of Rca according to Model3. However, unlike Rca, the intermediates of the Mg^{2+}-ATP mediated association of ClpA forms stable isolable complexes with K_d values of ~1 nM and below 0.17 nM [8] for dimer-tetramer, and tetramer-hexamer association respectively.

Our FCS data for Rca self association, however, shows a continuous assembly, and the average oligomeric sizes passes well below the theoretical hexameric limit requiring the consideration of a high M.W. oligomer in all our assembly models to explain the experimental data. We included a high M.W. oligomer comprising 24 subunits as the terminal oligomeric species in all the three different assembly models we considered (table 3.1.1). The models differ in the number of intermediate oligomeric states between a monomer and a 24-mer. We find that our data is consistent with the presence of at least one intermediate (Model2) or more likely two intermediates (Model3) before the formation of hexamers form monomers. In other words, this suggests that the non-cooperative self-association of Rca. Our data also fits equally well with both the models 2, and 3, and a distinction between the models require information based on other sources, such as the early biochemical studies on Rca, and the known association pathways for proteins belonging to the same family of proteins.

For Rca, the presence of a dimer has been routinely observed using SE-HPLC, and given that the formation of dimmers from two monomers are more statistically

probable then the formation of trimer from three monomers. Also, the self-association pathway of another related protein ClpA proceeds through the formation of dimeric and tetrameric intermediates as mentioned above. With these arguments, we can predict Model 3 as the favored self-association model of Rca, and draw our conclusions based on this model. According to this model, the fractional concentration profiles of the oligomers show that different oligomeric species dominate at different concentration ranges.

In presence of ADP, this model predicts a rise of hexamers at 1 µM (fig. 3.1.1 D) with a dominant population at 10-30 µM concentration. Tetramers, on the other hand, are significantly populated at concentrations between 5-20 µM. The model predicts the start of the rise of high M.W. oligomer (greater then hexamer) at ~15 µM, which becomes the dominant population above 40 µM. Given the inherent experimental uncertainties, FCS alone cannot distinguish the intermediate oligomeric states between a hexamer and a 24-mer which may be present at the high concentration regime, and hence they were not included in the model. At this point, the mechanism of the formation high M.W. species remains uncertain. They can either form as stack of toroidal rings (fig. 3.2.2 A) which has been observed for the Hsp104 protein, or grow as the pseudo hexameric spirals (fig. 3.2.2 B).

In either case, a simple distinction between the two structure is not possible form our FCS data. However, the observed continuous association at higher concentrations makes the pseudo spiral model stand out, because its unbound symmetry allows the growth in one direction by sequential addition of dimmers. In support of this notion, we can argue that the modeled K_d values for the dimer-tetramer and the tetramer-hexamer step are both of same magnitude, and are equal to ~1 µM (table 3.1.1). In other words,

this means that the addition of a dimer to either a dimer or to a tetramer is energetically equivalent. The spiral growth mechanism (fig. 3.2.2 B) also explains the observed broad size distribution by SE-HPLC [1, 2].

We observed a similar stepwise assembly of Rca in the presence of ATP, and the experimental FCS results were interpreted in the light of the same association model (Model 3). The data suggests a monomer being the dominant species at low concentrations up to ~1 µM (fig. 3.2.1 B), and a rather steeper transition from monomers to hexamers. The rise of the hexamers starts at about 0.9 µM, which quickly evolves as the predominant population beyond 5 µM, and stays as such through the highest measured concentration at 100 µM (fig. 3.2.1 B). This result is consistent with an earlier observation of hexameric rings of tobacco R294V Rca in presence of ATP [3]. The maximum population of hexamers was observed at ~30 µM which is about 77% of all the oligomers combined. The corresponding numbers for ADP only case were ~15 µM, and 40% respectively (fig. 3.1.1 D) which is even lower than the fraction of hexamers obtained (~50%) at 100 µM Rca in presence of ATP (fig. 3.2.1 B).

On the other hand, the population of large oligomers (greater then hexamers) are significantly suppressed by the presence of ATP binding of Rca, as can be inferred from the ~120 fold increase in the dissociation coefficient (K_{d4}) for the hexamer to 24-mer equlibria compared to the ADP only case (tables 3.1.1, and 3.2.1). Large oligomers also appear late at ~30 µM, and their maximum concentration stays below 42% at the highest measured concentration. The corresponding figures for ADP case are 15 µM and 74% respectively. This remarkable shuttling of the population of hexamers and large

oligomers between ATP and ADP offers a critical insight to what might be the active oligomeric state and regulation of Rca.

The physiological role of Rca is accomplished during the light phase of photosynthesis, where the stromatal ATP levels are high, and the activity of Rca is up regulated, whereas during the dark phase of photosynthesis, the ADP levels rise and the activity is down regulated [10, 11]. Our results suggest that this regulation of Rca activity might be accomplished by the oligomeric switch between hexamer and large aggregates. Further support in favor of this argument come from the nucleotide titration experiment (fig. 5.1). In this experiment, the diffusion coefficient measured for 60 μM Rca under five different ATP/ADP conditions show that Rca maintains a low oligomeric state in presence of ATP, and the average oligomeric size increases sharply as ATP is completely replaced by ADP.

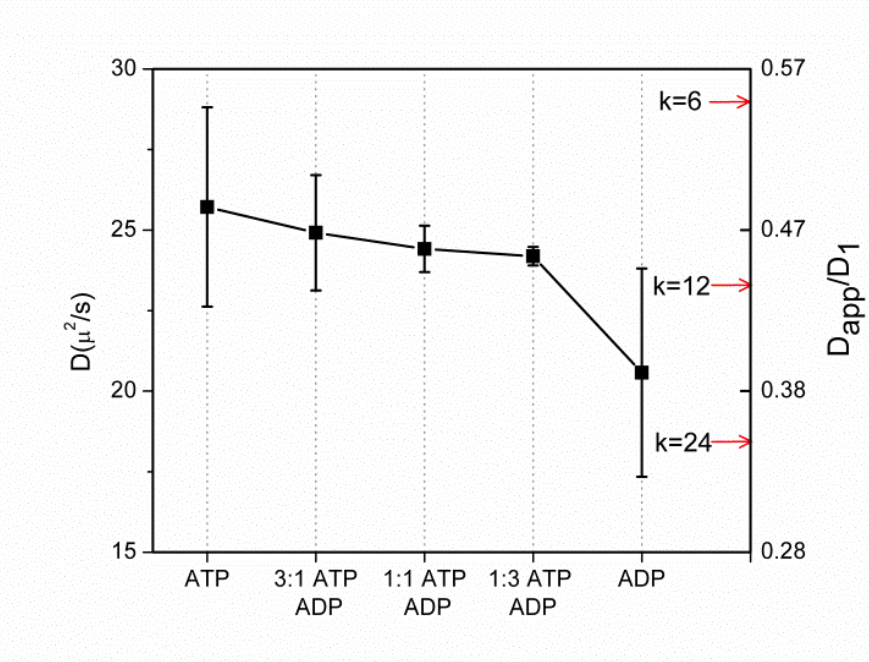

Figure 5.1. Nucleotide Titration Results. The apparent diffusion coefficients (D_{app}, *black squares*) measured for 60μM mutant (D173N) Rca under different nucleotide conditions as outlined in the X-axis of the graph above. The error bars represent the experimental standard deviations of at least three identical determinations. The relative apparent diffusion coefficients (D_{app}/D_1) scale is provided in the right hand Y-axis; the values corresponding to a hexamer ($k = 6$), a dodecamer ($k = 12$), and for a 24-mer ($k = 24$) are indicated with red arrows.

The results from this titration experiment also provide justification for using the mutant D173N protein despite of its residual ability to hydrolyze ATP (see chapter 2). It is clear from the titration results that the presence of ADP in large proportion (66%) cannot significantly influence the course of Rca self association. Our full range self association data in presence of a mixture of ATP/ADP at the ratio of 3:1 also resemble the ATP only measurements, and rule out the possibility that slow hydrolysis of ATP by the mutant can significantly influence the association pathway.

The Mg^{2+} titration experiments show that Rca hexamers do not form in low Mg^{2+} concentration, and a critical concentration of Mg^{2+} is required for hexamers to form. This

result supports the well known fact that ATP-ase proteins such as kinesin are only functional in presence of ATP-Mg^{2+} complex, the binding of Mg^{2+} is critical to the hydrolysis of ATP by the ATP-ases. We estimated that a critical concentration of 3 mM free Mg^{2+} , or 5 mM total Mg^{2+} is required for the formation of hexamers. A full range assembly study done by FCS are also in support of this fact, and it shows that at concentrations lower than the critical free Mg^{2+} concentration, the association resembles more like the ADP induced assembly.

In essence, using the results presented in this manuscript we are able to highlight the self association pathway of Rca, and provide a strong lead to toward the regulation of Rca activity during different photosynthetic phases. At the same time our estimates of the thermodynamic constants associated with different oligomeric equlibria provide valuable information toward proper characterization of the active assembly state(s) of Rca in future activase research.

References

1. Portis, A.R., Jr., *Rubisco activase - Rubisco's catalytic chaperone.* Photosynth Res, 2003. **75**(1): p. 11-27.

2. Barta, C., et al., *Structural changes associated with the acute thermal instability of Rubisco activase.* Arch Biochem Biophys. **499**(1-2): p. 17-25.

3. Stotz, M., et al., *Structure of green-type Rubisco activase from tobacco.* Nat Struct Mol Biol. **18**(12): p. 1366-70.

4. Mueller-Cajar, O., et al., *Structure and function of the AAA+ protein CbbX, a red-type Rubisco activase.* Nature. **479**(7372): p. 194-9.

5. Blayney, M.J., S.M. Whitney, and J.L. Beck, *NanoESI mass spectrometry of Rubisco and Rubisco activase structures and their interactions with nucleotides and sugar phosphates.* J Am Soc Mass Spectrom. **22**(9): p. 1588-601.

6. Bieniossek, C., B. Niederhauser, and U.M. Baumann, *The crystal structure of apo-FtsH reveals domain movements necessary for substrate unfolding and translocation.* Proc Natl Acad Sci U S A, 2009. **106**(51): p. 21579-84.

7. Niwa, H., et al., *Hexameric ring structure of the ATPase domain of the membrane-integrated metalloprotease FtsH from Thermus thermophilus HB8.* Structure, 2002. **10**(10): p. 1415-23.

8. Kress, W., H. Mutschler, and E. Weber-Ban, *Assembly pathway of an AAA+ protein: tracking ClpA and ClpAP complex formation in real time.* Biochemistry, 2007. **46**(21): p. 6183-93.

9. Veronese, P.K., R.P. Stafford, and A.L. Lucius, *The Escherichia coli ClpA molecular chaperone self-assembles into tetramers.* Biochemistry, 2009. **48**(39): p. 9221-33.

10. Zhang, N., P. Schurmann, and A.R. Portis, Jr., *Characterization of the regulatory function of the 46-kDa isoform of Rubisco activase from Arabidopsis.* Photosynth Res, 2001. **68**(1): p. 29-37.

11. Zhang, N., et al., *Light modulation of Rubisco in Arabidopsis requires a capacity for redox regulation of the larger Rubisco activase isoform.* Proc Natl Acad Sci U S A, 2002. **99**(5): p. 3330-4.

12. Parke, C.L., et al., *ATP hydrolysis in Eg5 kinesin involves a catalytic two-water mechanism.* J Biol Chem. **285**(8): p. 5859-67.

REFERENCES

Chapter 1

1. Goodsell, D.S. and A.J. Olson, *Structural symmetry and protein function.* Annu Rev Biophys Biomol Struct, 2000. **29**: p. 105-53.

2. Hashimoto, K., et al., *Caught in self-interaction: evolutionary and functional mechanisms of protein homooligomerization.* Phys Biol. **8**(3): p. 035007.

3. Blundell, T., et al., *Insulin: The Structure in the Crystal and its Reflection in Chemistry and Biology by*, in *Advances in Protein Chemistry*. 1972, Academic Press. p. 279-402.

4. Lumry, R. and S. Rajender, *Enthalpy-entropy compensation phenomena in water solutions of proteins and small molecules: a ubiquitous property of water.* Biopolymers, 1970. **9**(10): p. 1125-227.

5. Evans, P.R., *Structural aspects of allostery.* Current Opinion in Structural Biology, 1991. **1**(5): p. 773-779.

6. Perutz, M.F., *Mechanisms of cooperativity and allosteric regulation in proteins.* Q Rev Biophys, 1989. **22**(2): p. 139-237.

7. Srere, P.A., *Why are enzymes so big?* Trends in Biochemical Sciences, 1984. **9**(9): p. 387-390.

8. Kurland, C.G., *Translational accuracy and the fitness of bacteria.* Annu Rev Genet, 1992. **26**: p. 29-50.

9. Parker, J., *Errors and alternatives in reading the universal genetic code.* Microbiol Rev, 1989. **53**(3): p. 273-98.

10. Crick, F.H.C. and J.D. Watson, *Virus Structure: General Principles*, in *Ciba Foundation Symposium - Steroid Hormones and Enzymes (Book II of Colloquia on Endocrinology)*. 2008, John Wiley & Sons, Ltd. p. 5-18.

11. Wolynes, P.G., *Symmetry and the energy landscapes of biomolecules.* Proc Natl Acad Sci U S A, 1996. **93**(25): p. 14249-55.

12. Stossel, T.P., *From signal to pseudopod. How cells control cytoplasmic actin assembly.* J Biol Chem, 1989. **264**(31): p. 18261-4.

13. Mitchison, T. and M. Kirschner, *Dynamic instability of microtubule growth.* Nature, 1984. **312**(5991): p. 237-242.

14. Mitchison, T.J., *Microtubule dynamics and kinetochore function in mitosis.* Annu Rev Cell Biol, 1988. **4**: p. 527-49.

15. Crick, F.H.C. and J.D. Watson, *Structure of Small Viruses.* Nature, 1956. **177**(4506): p. 473-475.

16. Cohen-Krausz, S. and S. Trachtenberg, *The Flagellar Filament Structure of the Extreme Acidothermophile Sulfolobus shibatae B12 Suggests that Archaeabacterial Flagella have a Unique and Common Symmetry and Design.* Journal of Molecular Biology, 2008. **375**(4): p. 1113-1124.

17. Hulmes, D.J., *The collagen superfamily--diverse structures and assemblies.* Essays Biochem, 1992. **27**: p. 49-67.

18. Hanson, P.I. and S.W. Whiteheart, *AAA+ proteins: have engine, will work.* Nat Rev Mol Cell Biol, 2005. **6**(7): p. 519-529.

19. Neuwald, A.F., et al., *AAA+: A class of chaperone-like ATPases associated with the assembly, operation, and disassembly of protein complexes.* Genome Res, 1999. **9**(1): p. 27-43.

20. Iyer, L.M., et al., *Evolutionary history and higher order classification of AAA+ ATPases.* J Struct Biol, 2004. **146**(1-2): p. 11-31.

21. Vale, R.D., *AAA proteins. Lords of the ring.* J Cell Biol, 2000. **150**(1): p. F13-9.

22. Erdmann, R., *AAA ATPases: Structure and function.* Biochimica et Biophysica Acta (BBA) - Molecular Cell Research. **1823**(1): p. 1.

23. Wang, J., et al., *Nucleotide-dependent conformational changes in a protease-associated ATPase HsIU.* Structure, 2001. **9**(11): p. 1107-16.

24. Smith, G.R., et al., *A link between sequence conservation and domain motion within the AAA+ family.* J Struct Biol, 2004. **146**(1-2): p. 189-204.

25. Weibezahn, J., et al., *Characterization of a trap mutant of the AAA+ chaperone ClpB.* J Biol Chem, 2003. **278**(35): p. 32608-17.

26. Ogura, T., S.W. Whiteheart, and A.J. Wilkinson, *Conserved arginine residues implicated in ATP hydrolysis, nucleotide-sensing, and inter-subunit interactions in AAA and AAA+ ATPases.* J Struct Biol, 2004. **146**(1-2): p. 106-12.

27. Song, H.K., et al., *Mutational studies on HslU and its docking mode with HslV.* Proc Natl Acad Sci U S A, 2000. **97**(26): p. 14103-8.

28. Carmo-Silva, A.E. and M.E. Salvucci, *The activity of Rubisco's molecular chaperone, Rubisco activase, in leaf extracts.* Photosynth Res. **108**(2-3): p. 143-55.

29. Lorimer, G.H., M.R. Badger, and T.J. Andrews, *The activation of ribulose-1,5-bisphosphate carboxylase by carbon dioxide and magnesium ions. Equilibria, kinetics, a suggested mechanism, and physiological implications.* Biochemistry, 1976. **15**(3): p. 529-36.

30. Andersson, I. and A. Backlund, *Structure and function of Rubisco.* Plant Physiol Biochem, 2008. **46**(3): p. 275-91.

31. Whitney, S.M., R.L. Houtz, and H. Alonso, *Advancing our understanding and capacity to engineer nature's CO2-sequestering enzyme, Rubisco.* Plant Physiol. **155**(1): p. 27-35.

32. Mueller-Cajar, O., M. Stotz, and A. Bracher, *Maintaining photosynthetic CO2 fixation via protein remodelling: the Rubisco activases.* Photosynth Res. **119**(1-2): p. 191-201.

33. Cleland, W.W., et al., *Mechanism of Rubisco: The Carbamate as General Base.* Chem Rev, 1998. **98**(2): p. 549-562.

34. Parry, M.A., et al., *Rubisco regulation: a role for inhibitors.* J Exp Bot, 2008. **59**(7): p. 1569-80.

35. Andralojc, P.J., et al., *2-Carboxy-D-arabinitol 1-phosphate (CA1P) phosphatase: evidence for a wider role in plant Rubisco regulation.* Biochem J. **442**(3): p. 733-42.

36. Seemann, J.R., J. Kobza, and B.D. Moore, *Metabolism of 2-carboxyarabinitol 1-phosphate and regulation of ribulose-1,5-bisphosphate carboxylase activity.* Photosynth Res, 1990. **23**(2): p. 119-30.

37. Berry, J.A., et al., *Isolation, identification, and synthesis of 2-carboxyarabinitol 1-phosphate, a diurnal regulator of ribulose-bisphosphate carboxylase activity.* Proc Natl Acad Sci U S A, 1987. **84**(3): p. 734-8.

38. Ellis, R.J., *The most abundant protein in the world.* Trends in Biochemical Sciences, 1979. **4**(11): p. 241-244.

39. Somerville, C.R., A.R. Portis, and W.L. Ogren, *A Mutant of Arabidopsis thaliana Which Lacks Activation of RuBP Carboxylase In Vivo.* Plant Physiol, 1982. **70**(2): p. 381-7.

40. Salvucci, M.E., A.R. Portis, Jr., and W.L. Ogren, *A soluble chloroplast protein catalyzes ribulosebisphosphate carboxylase/oxygenase activation in vivo.* Photosynth Res, 1985. **7**(2): p. 193-201.

41. Robinson, S.P. and A.R. Portis, Jr., *Adenosine triphosphate hydrolysis by purified rubisco activase.* Arch Biochem Biophys, 1989. **268**(1): p. 93-9.

42. Robinson, S.P. and A.R. Portis, *Ribulose-1,5-bisphosphate carboxylase/oxygenase activase protein prevents the in vitro decline in activity of ribulose-1,5-bisphosphate carboxylase/oxygenase.* Plant Physiol, 1989. **90**(3): p. 968-71.

43. Robinson, S.P., et al., *Purification and assay of rubisco activase from leaves.* Plant Physiol, 1988. **88**(4): p. 1008-14.

44. Salvucci, M.E. and S.J. Crafts-Brandner, *Mechanism for deactivation of Rubisco under moderate heat stress.* Physiologia Plantarum, 2004. **122**(4): p. 513-519.

45. Salvucci, M.E. and S.J. Crafts-Brandner, *Relationship between the heat tolerance of photosynthesis and the thermal stability of rubisco activase in plants from contrasting thermal environments.* Plant Physiol, 2004. **134**(4): p. 1460-70.

46. Crafts-Brandner, S.J. and M.E. Salvucci, *Rubisco activase constrains the photosynthetic potential of leaves at high temperature and CO2.* Proc Natl Acad Sci U S A, 2000. **97**(24): p. 13430-5.

47. Stotz, M., et al., *Structure of green-type Rubisco activase from tobacco.* Nat Struct Mol Biol. **18**(12): p. 1366-70.

48. van de Loo, F.J. and M.E. Salvucci, *Activation of ribulose-1,5-biphosphate carboxylase/oxygenase (Rubisco) involves Rubisco activase Trp16.* Biochemistry, 1996. **35**(25): p. 8143-8.

49. Esau, B.D., G.W. Snyder, and A.R. Portis, Jr., *Differential effects of N- and C-terminal deletions on the two activities of rubisco activase.* Arch Biochem Biophys, 1996. **326**(1): p. 100-5.

50. Barta, C., et al., *Structural changes associated with the acute thermal instability of Rubisco activase.* Arch Biochem Biophys. **499**(1-2): p. 17-25.

51. Wang, Z.Y., R.T. Ramage, and A.R. Portis, Jr., *Mg2+ and ATP or adenosine 5'-[gamma-thio]-triphosphate (ATP gamma S) enhances intrinsic fluorescence and induces aggregation which increases the activity of spinach Rubisco activase.* Biochim Biophys Acta, 1993. **1202**(1): p. 47-55.

52. Li, C., D. Wang, and A.R. Portis, Jr., *Identification of critical arginine residues in the functioning of Rubisco activase.* Arch Biochem Biophys, 2006. **450**(2): p. 176-82.

53. Blayney, M.J., S.M. Whitney, and J.L. Beck, *NanoESI mass spectrometry of Rubisco and Rubisco activase structures and their interactions with nucleotides and sugar phosphates.* J Am Soc Mass Spectrom. **22**(9): p. 1588-601.

54. Lilley, R.M. and A.R. Portis Jr, *ATP Hydrolysis Activity and Polymerization State of Ribulose-1,5-Bisphosphate Carboxylase Oxygenase Activase (Do the Effects of Mg2+, K+, and Activase Concentrations Indicate a Functional Similarity to Actin?).* Plant Physiol, 1997. **114**(2): p. 605-613.

55. Hong, P., S. Koza, and E.S. Bouvier, *Size-Exclusion Chromatography for the Analysis of Protein Biotherapeutics and their Aggregates.* J Liq Chromatogr Relat Technol. **35**(20): p. 2923-2950.

56. Elson, E.L. and D. Magde, *Fluorescence correlation spectroscopy. I. Conceptual basis and theory.* Biopolymers, 1974. **13**(1): p. 1-27.

57. Magde, D., E.L. Elson, and W.W. Webb, *Fluorescence correlation spectroscopy. II. An experimental realization.* Biopolymers, 1974. **13**(1): p. 29-61.

58. Magde, D., E. Elson, and W.W. Webb, *Thermodynamic Fluctuations in a Reacting Systemâ€"Measurement by Fluorescence Correlation Spectroscopy.* Physical Review Letters, 1972. **29**(11): p. 705-708.

59. Jameson, D.M., J.A. Ross, and J.P. Albanesi, *Fluorescence fluctuation spectroscopy: ushering in a new age of enlightenment for cellular dynamics.* Biophys Rev, 2009. **1**(3): p. 105-118.

60. Muller, J.D., Y. Chen, and E. Gratton, *Fluorescence correlation spectroscopy.* Methods Enzymol, 2003. **361**: p. 69-92.

61. Lakowicz, J. and N. Thompson, *Fluorescence Correlation Spectroscopy*, in *Topics in Fluorescence Spectroscopy*. 1999, Springer US. p. 337-378.

62. Abney, J.R., et al., *Chromatin dynamics in interphase nuclei and its implications for nuclear structure.* J Cell Biol, 1997. **137**(7): p. 1459-68.

63. Hemmerich, P., et al., *Dynamics of inner kinetochore assembly and maintenance in living cells.* J Cell Biol, 2008. **180**(6): p. 1101-14.

64. Boxer, S.G., *Molecular transport and organization in supported lipid membranes.* Curr Opin Chem Biol, 2000. **4**(6): p. 704-9.

65. Kahya, N. and P. Schwille, *Fluorescence correlation studies of lipid domains in model membranes.* Mol Membr Biol, 2006. **23**(1): p. 29-39.

66. Berland, K.M., P.T. So, and E. Gratton, *Two-photon fluorescence correlation spectroscopy: method and application to the intracellular environment.* Biophys J, 1995. **68**(2): p. 694-701.

67. Lukacs, G.L., et al., *Size-dependent DNA mobility in cytoplasm and nucleus.* J Biol Chem, 2000. **275**(3): p. 1625-9.

68. Wachsmuth, M., W. Waldeck, and J. Langowski, *Anomalous diffusion of fluorescent probes inside living cell nuclei investigated by spatially-resolved fluorescence correlation spectroscopy.* J Mol Biol, 2000. **298**(4): p. 677-89.

69. Rajagopalan, S., F. Huang, and A.R. Fersht, *Single-Molecule characterization of oligomerization kinetics and equilibria of the tumor suppressor p53.* Nucleic Acids Res. **39**(6): p. 2294-303.

70. Krouglova, T., J. Vercammen, and Y. Engelborghs, *Correct diffusion coefficients of proteins in fluorescence correlation spectroscopy. Application to tubulin oligomers induced by Mg2+ and Paclitaxel.* Biophys J, 2004. **87**(4): p. 2635-46.

71. Bulseco, D.A., et al., *Chapter 21 - Fluorescence Correlation Spectroscopy: Molecular Complexing in Solution and in Living Cells*, in *Methods in Cell Biology*, Academic Press. p. 489-524.

72. Hink, M.A., M. Postma, and P.M. Conn, *Chapter 11 - Monitoring Receptor Oligomerization by Line-Scan Fluorescence Cross-Correlation Spectroscopy*, in *Methods in Cell Biology*, Academic Press. p. 197-212.

73. Ohta, S., et al., *The interaction of Hsp104 with yeast prion Sup35 as analyzed by fluorescence cross-correlation spectroscopy.* Biochemical and Biophysical Research Communications. **442**(1-2): p. 28-32.

74. Salvucci, M.E., *Potential for interactions between the carboxy- and amino-termini of Rubisco activase subunits.* FEBS Lett, 2004. **560**(1-3): p. 205-9.

75. Chen, Y., et al., *The photon counting histogram in fluorescence fluctuation spectroscopy.* Biophys J, 1999. **77**(1): p. 553-67.

76. Perroud, T.D., et al., *Photon counting histogram for one-photon excitation.* Chemphyschem, 2003. **4**(10): p. 1121-3.

77. Terada, N., et al., *Size Distribution of Linear and Helical Polymers in Actin Solution Analyzed by Photon Counting Histogram.* Biophysical Journal, 2007. **92**(6): p. 2162-2171.

78. Mandel, L., *Fluctuations of photon beams and their correlations.* Proc. Phys. Soc. , 1958. **72**: p. 1037-1048.

79. Muller, J.D., Y. Chen, and E. Gratton, *Resolving heterogeneity on the single molecular level with the photon-counting histogram.* Biophys J, 2000. **78**(1): p. 474-86.

Chapter 2

1. Salvucci, M.E., *Potential for interactions between the carboxy- and amino-termini of Rubisco activase subunits.* FEBS Lett, 2004. **560**(1-3): p. 205-9.

2. Barta, C., A.E. Carmo-Silva, and M.E. Salvucci, *Purification of Rubisco activase from leaves or after expression in Escherichia coli.* Methods Mol Biol. **684**: p. 363-74.

3. Gendron, P.O., F. Avaltroni, and K.J. Wilkinson, *Diffusion coefficients of several rhodamine derivatives as determined by pulsed field gradient-nuclear magnetic resonance and fluorescence correlation spectroscopy.* J Fluoresc, 2008. **18**(6): p. 1093-101.

4. Muller, C.B., et al., *Precise measurement of diffusion by multi-color dual-focus fluorescence correlation spectroscopy.* EPL, 2008. **83**(4): p. 46001.

5. Petrasek, Z. and P. Schwille, *Precise measurement of diffusion coefficients using scanning fluorescence correlation spectroscopy.* Biophys J, 2008. **94**(4): p. 1437-48.

6. Mueller-Cajar, O., M. Stotz, and A. Bracher, *Maintaining photosynthetic CO2 fixation via protein remodelling: the Rubisco activases.* Photosynth Res. **119**(1-2): p. 191-201.

7. Rubinstein, M. and R.H. Colby, *Polymer physics*. 2003, Oxford: Oxford University Press. xi, 440 p.

8. Squire, P.G. and M.E. Himmel, *Hydrodynamics and protein hydration.* Arch Biochem Biophys, 1979. **196**(1): p. 165-77.

Chapter 3

1. Salvucci, M.E., *Potential for interactions between the carboxy- and amino-termini of Rubisco activase subunits.* FEBS Lett, 2004. **560**(1-3): p. 205-9.

2. Stotz, M., et al., *Structure of green-type Rubisco activase from tobacco.* Nat Struct Mol Biol. **18**(12): p. 1366-70.

3. Krouglova, T., J. Vercammen, and Y. Engelborghs, *Correct diffusion coefficients of proteins in fluorescence correlation spectroscopy. Application to tubulin oligomers induced by Mg2+ and Paclitaxel.* Biophys J, 2004. **87**(4): p. 2635-46.

4. Rajagopalan, S., F. Huang, and A.R. Fersht, *Single-Molecule characterization of oligomerization kinetics and equilibria of the tumor suppressor p53.* Nucleic Acids Res. **39**(6): p. 2294-303.

5. Sahoo, B., et al., *Protein aggregation probed by two-photon fluorescence correlation spectroscopy of native tryptophan.* J Chem Phys, 2008. **129**(7): p. 075103.

6. Chakraborty, M., et al., *Protein oligomerization monitored by fluorescence fluctuation spectroscopy: self-assembly of rubisco activase.* Biophys J. **103**(5): p. 949-58.

7. Chen, Y., et al., *The photon counting histogram in fluorescence fluctuation spectroscopy.* Biophys J, 1999. **77**(1): p. 553-67.

8. Portis, A.R., Jr., *Rubisco activase - Rubisco's catalytic chaperone.* Photosynth Res, 2003. **75**(1): p. 11-27.

9. Barta, C., et al., *Structural changes associated with the acute thermal instability of Rubisco activase.* Arch Biochem Biophys. **499**(1-2): p. 17-25.

10. Wang, Z.Y., R.T. Ramage, and A.R. Portis, Jr., *Mg2+ and ATP or adenosine 5'-[gamma-thio]-triphosphate (ATP gamma S) enhances intrinsic fluorescence and induces aggregation which increases the activity of spinach Rubisco activase.* Biochim Biophys Acta, 1993. **1202**(1): p. 47-55.

11. Li, C., D. Wang, and A.R. Portis, Jr., *Identification of critical arginine residues in the functioning of Rubisco activase.* Arch Biochem Biophys, 2006. **450**(2): p. 176-82.

12. Lakowicz, J. and N. Thompson, *Fluorescence Correlation Spectroscopy*, in *Topics in Fluorescence Spectroscopy*. 1999, Springer US. p. 337-378.

13. Yu, L., et al., *Determination of critical micelle concentrations and aggregation numbers by fluorescence correlation spectroscopy: aggregation of a lipopolysaccharide.* Anal Chim Acta, 2006. **556**(1): p. 216-25.

14. Mueller-Cajar, O., et al., *Structure and function of the AAA+ protein CbbX, a red-type Rubisco activase.* Nature. **479**(7372): p. 194-9.

15. Blayney, M.J., S.M. Whitney, and J.L. Beck, *NanoESI mass spectrometry of Rubisco and Rubisco activase structures and their interactions with nucleotides and sugar phosphates.* J Am Soc Mass Spectrom. **22**(9): p. 1588-601.

16. Hanson, P.I. and S.W. Whiteheart, *AAA+ proteins: have engine, will work.* Nat Rev Mol Cell Biol, 2005. **6**(7): p. 519-529.

17. Zhang, N., et al., *Light modulation of Rubisco in Arabidopsis requires a capacity for redox regulation of the larger Rubisco activase isoform.* Proc Natl Acad Sci U S A, 2002. **99**(5): p. 3330-4.

18. Zhang, N., P. Schurmann, and A.R. Portis, Jr., *Characterization of the regulatory function of the 46-kDa isoform of Rubisco activase from Arabidopsis.* Photosynth Res, 2001. **68**(1): p. 29-37.

Chapter 4

1. Portis, A.R., Jr., *Rubisco activase - Rubisco's catalytic chaperone.* Photosynth Res, 2003. **75**(1): p. 11-27.

2. Barta, C., et al., *Structural changes associated with the acute thermal instability of Rubisco activase.* Arch Biochem Biophys. **499**(1-2): p. 17-25.

3. Stotz, M., et al., *Structure of green-type Rubisco activase from tobacco.* Nat Struct Mol Biol. **18**(12): p. 1366-70.

4. Mueller-Cajar, O., et al., *Structure and function of the AAA+ protein CbbX, a red-type Rubisco activase.* Nature. **479**(7372): p. 194-9.

5. Blayney, M.J., S.M. Whitney, and J.L. Beck, *NanoESI mass spectrometry of Rubisco and Rubisco activase structures and their interactions with nucleotides and sugar phosphates.* J Am Soc Mass Spectrom. **22**(9): p. 1588-601.

6. Bieniossek, C., B. Niederhauser, and U.M. Baumann, *The crystal structure of apo-FtsH reveals domain movements necessary for substrate unfolding and translocation.* Proc Natl Acad Sci U S A, 2009. **106**(51): p. 21579-84.

7. Niwa, H., et al., *Hexameric ring structure of the ATPase domain of the membrane-integrated metalloprotease FtsH from Thermus thermophilus HB8.* Structure, 2002. **10**(10): p. 1415-23.

8. Kress, W., H. Mutschler, and E. Weber-Ban, *Assembly pathway of an AAA+ protein: tracking ClpA and ClpAP complex formation in real time.* Biochemistry, 2007. **46**(21): p. 6183-93.

9. Veronese, P.K., R.P. Stafford, and A.L. Lucius, *The Escherichia coli ClpA molecular chaperone self-assembles into tetramers.* Biochemistry, 2009. **48**(39): p. 9221-33.

10. Zhang, N., P. Schurmann, and A.R. Portis, Jr., *Characterization of the regulatory function of the 46-kDa isoform of Rubisco activase from Arabidopsis.* Photosynth Res, 2001. **68**(1): p. 29-37.

11. Zhang, N., et al., *Light modulation of Rubisco in Arabidopsis requires a capacity for redox regulation of the larger Rubisco activase isoform.* Proc Natl Acad Sci U S A, 2002. **99**(5): p. 3330-4.

12. Parke, C.L., et al., *ATP hydrolysis in Eg5 kinesin involves a catalytic two-water mechanism.* J Biol Chem. **285**(8): p. 5859-67.

APPENDIX I

SUPPLEMENTAL INFORMATION TO CHAPTER 3 SECTION 1

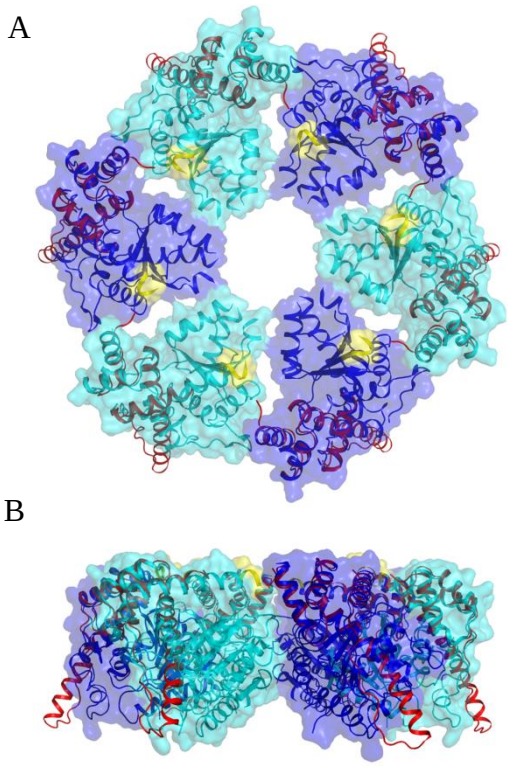

Figure A.1.1. A Model of the Closed Ring Tobacco Rca Apo-AAA+ Hexamer (alternating cyan and blue protomers; PDB ID 3ZW6) from cryo electron microscopy data with the creosote recognition domain x-ray structure (red; residues 250-351; PDB ID 3THG) superimposed. Shown in yellow are the locations of the Tobacco AAA+ fragment C-termini. **A)** View down the 6-fold axis of the hexameric model. **B)** Side-on-view with the model rotated up 90°.

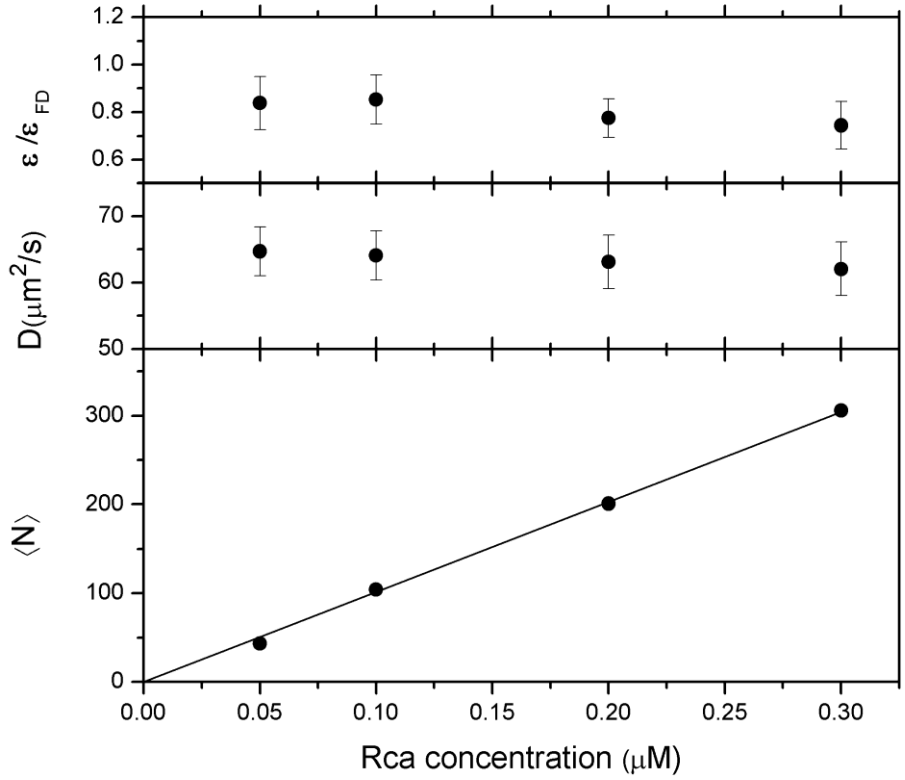

Figure A.1.2: Rca is a Monomer Below 300 nM. Top: ratio of the molecular brightness measured in experiments with labeled Rca (ε) and free Alexa 546 dye (ε_{FD}) as a function of Rca concentration. Middle: Diffusion coefficients obtained from fitting the FCS decays measured with labeled Rca in the 50-300 nM range. Bottom: mean number of diffusing particles obtained from the amplitude of the FCS decays measured with labeled Rca. Put together, these results are consistent with a monomeric form of Rca.

Analytical Data on Alexa-labeled Rca Preparations.

The labeling efficiency of Alexa-derivatized Rca was estimated from the reverse phase HPLC analysis (fig. A.1.3). The absorbance scans of the collected eluting fractions are given in fig. A.1.4. MALDI spectra showing the molar masses of the labeled and the control in presence of DTT are shown in fig. A.1.5. See chapter 2 for experimental details.

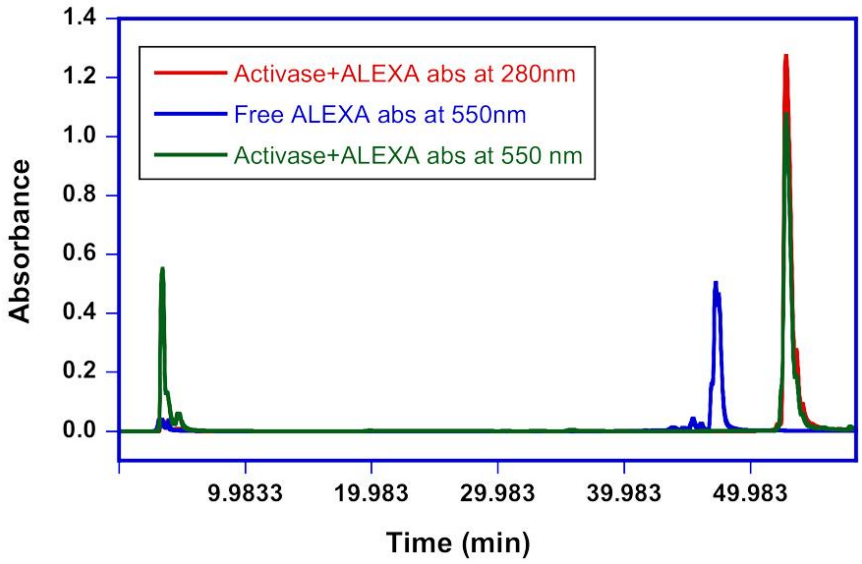

Figure A.1.3. HPLC Chromatograms of the wt Protein. Reverse-phase HPLC chromatograms of alexa-labeled Rca monitored at 280 nm (red) and at 550 nm (green), and free alexa dye (blue). The chromatograms indicate that labeled Rca preparations do not contain any traces of free alexa dye.

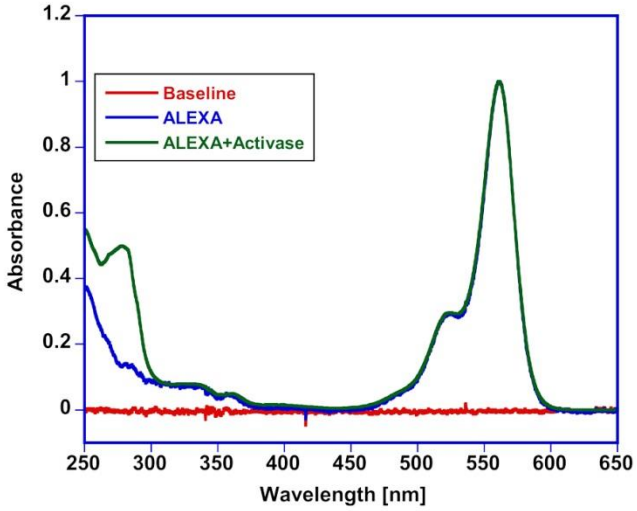

Figure A.1.4. Absorbance Spectra of the wt Protein. The 55-min peak eluting from the HPLC column (labeled protein) was collected and analyzed by absorbance. The molar ratio of Alexa: Rca in covalently labeled preparations was determined by absorbance as described in the Methods section.

Diffusion Coefficient of the Monomer and Oligomers

Effect of Molecular Shape.

Our assumption was that the different oligomeric states of Rca were approximately spherical. Here, in this section we evaluated the effect of molecular shape on the values of the relative diffusion coefficient (D_{app}/D_1) by modeling the protein as an ellipsoid. For a non-spherical particle such as an ellipsoid, the diffusion coefficient is smaller the spherical particle of same volume, and the ratio of the diffusion coefficient of a sphere to the ellipsoid is given by eq. A.1.1. In this equation, the parameter p is the ration of the axial and equatorial semi axis of the molecule and the parameter ξ which is also known as the Perrin factor, is given by equation A.1.2.

$$\frac{D_{sphere}}{D_{ellipsoid}} = \frac{p^{2/3}\xi}{\text{atan}\,\xi} \qquad \text{(Oblate ellipsoid)} \qquad \text{Eq. A.1.1}$$

$$\xi = \frac{\sqrt{|p^2 - 1|}}{p} \qquad \text{Eq. A.1.2}$$

The diffusion coefficient calculated considering Rca as an oblate ellipsoid with an axial ratio p = 0.42 as suggested by the hexameric structure published by Stotz *et al.* is equal to 94% of the value for a sphere of same volume ($D_{sphere}/D_{ellipsoid}$ = 1.07, eqs. A.1.1 and A.1.2). This proves that the influence of the molecular shape is on the absolute diffusion coefficients are indeed small and will be negligible in the relative diffusion coefficient values.

Effect of Hydration Water.

We analysed the effect of hydration on the diffusion coefficients, because the radius of gyration of the protein changes depending on the extent of hydration, *h*, which ranges for 0.2-0.6 gm of water per gram of protein affecting the diffusion coefficient. The relationship between the volume of the hydrated protein(V_h) and the volume of the dry protein molecule is given by

$$V_h = V_{dry} + V_{water} = \frac{4}{3}\pi R^3 + \frac{M_w}{N_{av}\delta_{water}} h \qquad \text{Eq. A.1.3}$$

Where V_{water} is the volume of hydration water, R and M_w are the radius and the molecular weight of the dry protein, N_{av} is the Avagadro's number, the density of water is δ_{water}, and h is the hydration factor.

A ratio of the diffusion coefficient can be obtained for two values of hydration water (h_1 and h_2) and is given by,

$$\frac{D(h_1)}{D(h_2)} = \left(\frac{V_h(h_2)}{V_h(h_1)} \right)^{1/3} \qquad \text{Eq. A.1.4}$$

Using R = 6.35 10^{-7} cm for the hexamer (as described in chapter 2) and M_w = 257.3 kDa, we obtain

$$\frac{D(h=0.6)}{D(h=0.2)} = 0.96$$

This show only 4% change in the absolute values of the diffusion coefficients for different amounts of bound water. Assuming same degree of hydration for different oligomers of the protein, we can claim that this effect is negligible in the relative diffusion coefficient values.

Comparison between Different Estimates of the Diffusion Coefficients.

In this section, we compare the diffusion coefficients for different oligomeric states calculated form two different approaches, as mentioned in chapter 2. In the first approach, we used Stokes-Einstein's relationship and calculated the diffusion coefficients relative to the experimental monomeric diffusion coefficient (D_1 = 64.7 $\mu m^2 s^{-1}$) measured at 50nM Rca. While in the second approach we estimated the diffusion coefficients using reconstituted models for monomer, dimer, trimer and tetramer from the published hexameric crystal structure of tobacco Rca.

A comparison of the ratios D_k/D_1 (k = 2,3,4..) obtained using these two methods are given below.

Table A.1.1 Comparison between Different Estimates of the Diffusion Coefficients

	Method 1 ($D_k = D_1/k^{1/3}$)	**Method 2** **(from structural data)**
D_2/D_1	0.79	0.80
D_3/D_1	0.69	0.66
D_4/D_1	0.63	0.59
D_6/D_1	0.55	0.54

There is however, significant approximation in both our approaches. It is therefore, critical to show that none of these approximations used for the analysis influence our interpretation of the data.

In the fig, we have shown that the values calculated using either approaches overlap very well with each other as well as the experimental data, and do not influence our interpretation of the experimental data.

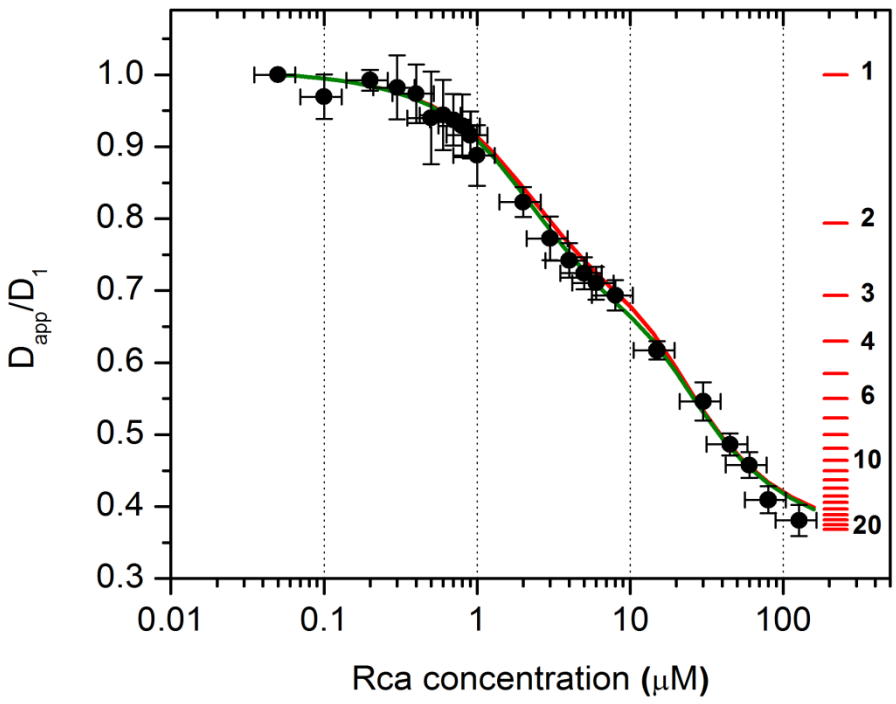

Figure A.1.5. Diffusion Coefficient Estimates from Different Approximations. Results of modeling according to model 3 using K_{d1} = 3.5 μM, K_{d2} = 1 μM K_{d3} = 1 μM and K_{d4} = 25 μM^3. The line in green is identical to the one presented in Figure 3D in the manuscript, and has been calculated using the diffusion coefficients calculated from the structure of the reconstructed closed-ring hexamer of tobacco Rca. The line in red has been calculated using $D_k = D_1/k^{1/3}$ with a value of D_1 equal to the diffusion coefficient determined at 50 nM Rca.

FCS Analysis of Polydisperse Samples.

The rationale behind fitting multi component FCS curves with a one component equation lies in the resolvability of the of the FCS decay for multi component solutions. Meseth et al.[12] have shown that the FCS decay of a two component solution can only be distinguished experimentally from a one component FCS if the diffusion times of the two species differ by a factor of 1.6. Even though this value depends on a variety of experimental factors, it provides a sound alternative approach to analyze FCS of polydisperse solutions. Following this approach, one obtains an apparent good fit using a one component model with an intermediate diffusion time when it becomes impossible to resolve mixtures. In support of this approximation, we performed FCS simulation using sim-FCS software (developed by Enrico Gratton) and found that the FCS decays of a mixture containing monomer, dimer etc. can't be resolved form a monodisperse sample with an intermediate diffusion coefficient. We set an FCS simulation for a sample containing dimmers, tetramers, and hexamers at 1/3 fractional concentration each. This simulation represents a condition close to what we expect for the Rca at 10 μM. Additionaly, because the concentration of the labeled Rca is much smaller than the unlabeled Rca, the probability that an oligomer will contain more than one labeled subunit is negligibly small, and it is reasonable to assume that the brightness of different oligomeric species are same. We further assumed Stokes-Einstein relationship to calculate the diffusion coefficients of different oligomers with respect to the diffusion coefficient of the dimer set at $D_2 = 52\ \mu^2/s$.

In fig. A.1.8 A, we plotted the result of the simulation (black line) fitted with a one component model (red line and residuals below). The recovered apparent diffusion

coefficient is 40.7 μ^2/s. Next, we performed a simulation assuming a monodisperse solution of diffusion coefficient 40.7 μ^2/s (Fig. A.1.8 B black line) and fitted with a one component model (red line and residuals below). The recovered diffusion coefficient, 40.3 μ^2/s, is very close to our input. Interestingly, the quality of the fits as judged by the residuals and the χ^2 are not significantly different. These simulations show that FCS is not sensitive to the minute differences in diffusion coefficient, and thus all our FCS decays can be fitted with one component model.

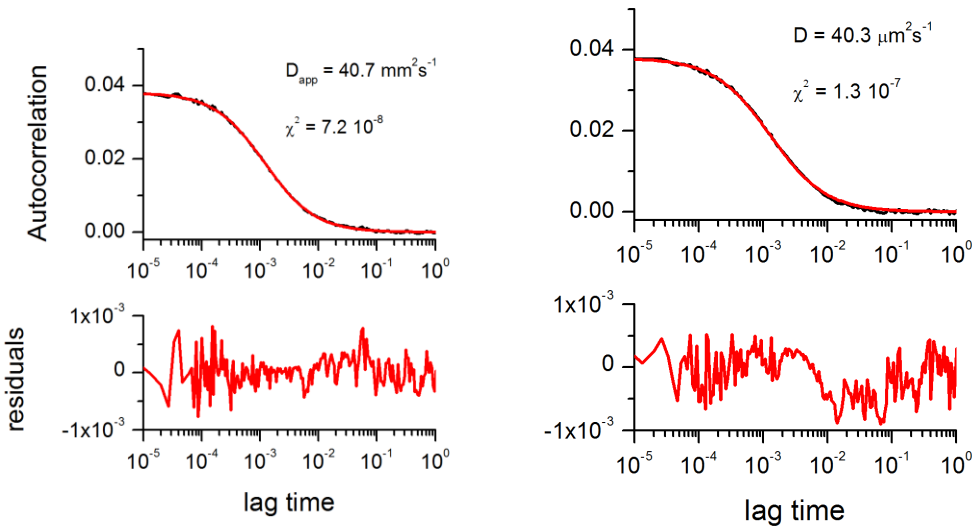

Figure A.1.6. Simulated FCS Decays. Simulated FCS decays of a mixture of dimer, tetramer and hexamer (A) and a monodisperse sample (B) with the same diffusion coefficient as the apparent diffusion of the mixture. The mixture (fractional concentration of each component = 1/3) produces an FCS decay that can be fitted with a one-component model to give an apparent diffusion coefficient of 40.7 $\mu m^2 s^{-1}$. The quality of the fit, judged by the residuals and χ^2 value, is excellent, and certainly not worse than the fit obtained for the monodisperse sample.

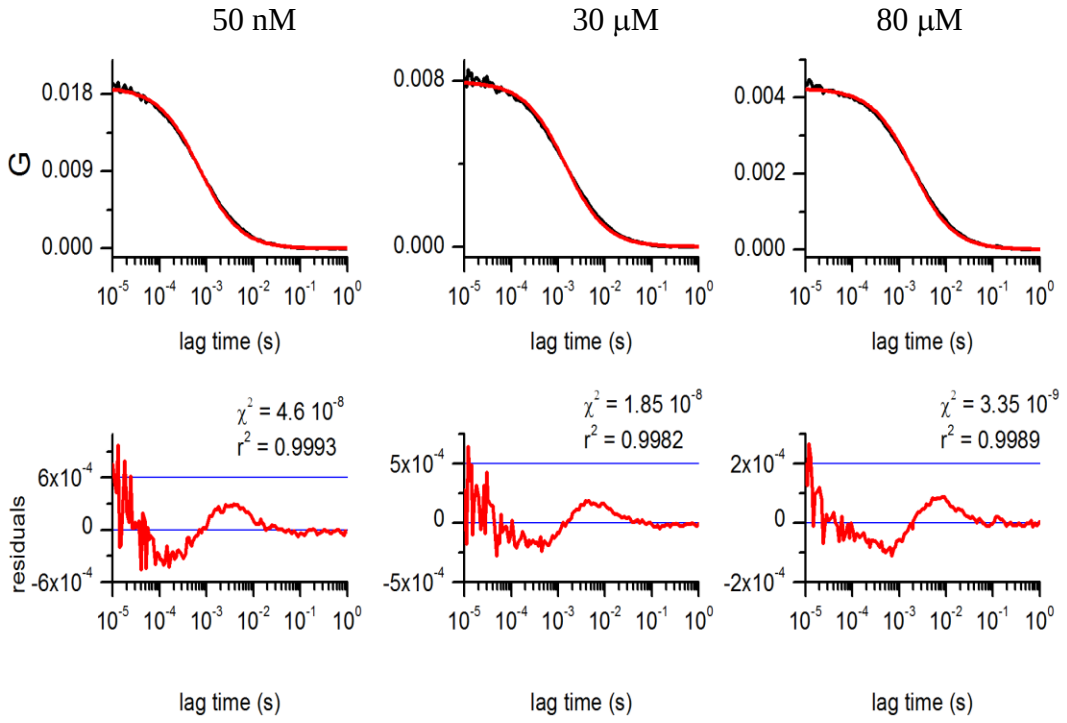

Figure A.1.7. Representative Experimental FCS Decays. Experimental FCS curves (black lines) fitted with a one component model (red lines). The apparent diffusion coefficients extracted from these fits were used to construct figure 3.1.1 in the manuscript. The value of χ^2 is calculated as the residual sum of squares divided by the degrees of freedom (N-2, where N is the size of the lag time vector). R^2 is the coefficient of determination. The qualities of the fits are similar at low and high concentrations, where we believe Rca is monomeric (50 nM) or highly polydisperse (high μM).

Uncertainties in the Determination of the Dissociation Constants.

For the second and the third model, we estimated the range of values of K_{d1} (first step in the assembly) that predict D_{app}/ D_1 values within the experimental error bars. We then optimized other K_d values while keeping K_{d1} at a fixed value. These estimates were only done by arbitrary visual inspection.

For the second model, a nice fit to the experimental data was obtained for K_{d1} in the range 3.5-10 μM^2 (fig. A.1.5). The optimized K_{d2} and K_{d3} values within this fixed bound of K_{d1} were (K_{d2} = 15 μM, K_{d3} = 2 μM^3 for K_{d1} = 3.5 μM^2, and K_{d2} = 1.3 μM, K_{d3} = 70 μM^3 for K_{d1} = 10 μM^2). Concentration profiles calculated these sets of Kd values are plotted in the top panel of each figure. For the third model, a nice fit to the experimental data was obtained for K_{d1} in the range 2.0-20 μM (Fig. S9B). Due to additional intermediate states in this model, this range is larger than in the case of model 2. The optimized K_{d2}- K_{d4} values within this fixed bound of K_{d1} were (K_{d2} = 2 μM, K_{d3} = 1 μM, K_{d4} = 20 μM^3 for K_{d1} = 2 μM, and K_{d2} = 0.03 μM, K_{d3} = 2 μM, K_{d4} = 8 μM^3 for K_{d1} = 20 μM).

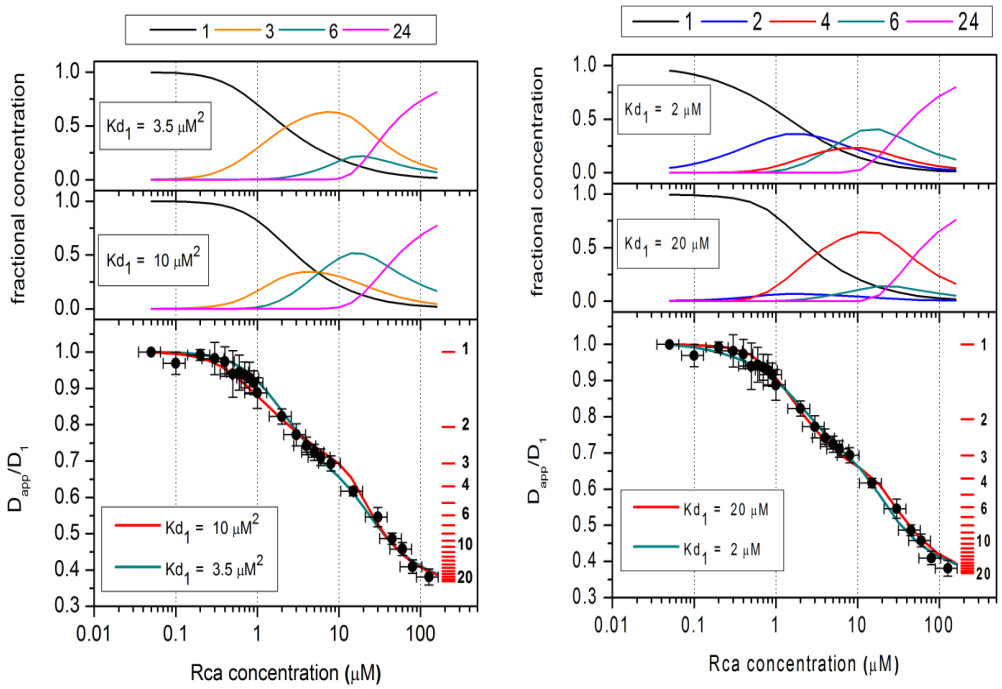

Figure A.1.8. Uncertainties in the determinations of the dissociation coefficients. Results of modeling according to models 2 (panel A) and 3 (panel B). The solid circles are the results of experiments, and the red and green solid lines behind them are the results of modeling. **A:** model 2 using K_{d1} = 3.5 μM^2, K_{d2} = 15 μM and K_{d3} = 2 μM^3 (green) and K_{d1} = 10 μM^2, K_{d2} = 1.3 μM and K_{d3} = 70 μM^3 (red). **B:** model 3 using K_{d1} = 2 μM, K_{d2} = 2 μM, K_{d3} = 1 μM and K_{d4} = 20 μM^3 (green) and K_{d2} = 20 μM, K_{d3} = 0.03 μM, K_{d4} = 2 μM^3 for K_{d1} = 0.8 μM. The concentration profiles shown on top of graphs A and B show the fractional concentrations calculated using these sets of K_d values.

APPENDIX II

SUPPLEMENTAL INFORMATION TO CHAPTER 3 SECTION 2

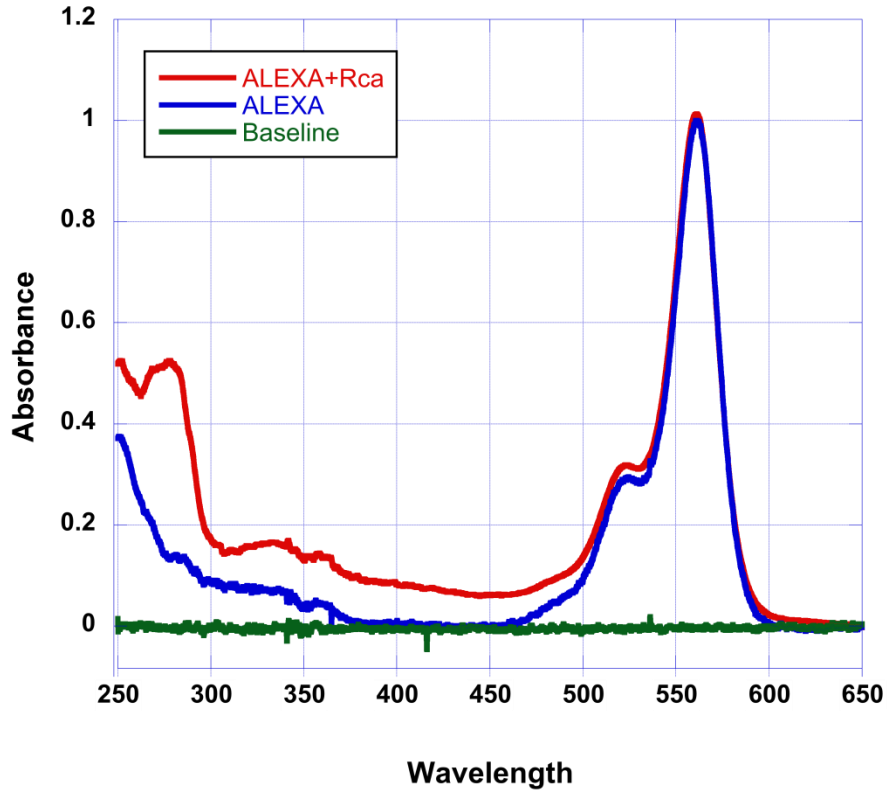

Figure A.2.1. Absorbance spectra of the mutant protein. The peak eluting from the HPLC column (labeled protein) was collected and analyzed by absorbance. The molar ratio of Alexa:Rca was calculated using Beer-Lambert Law.

A

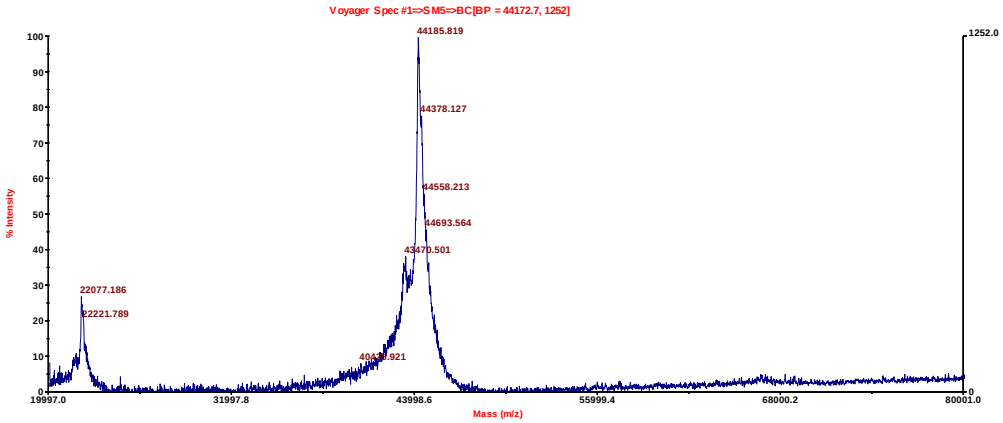

B

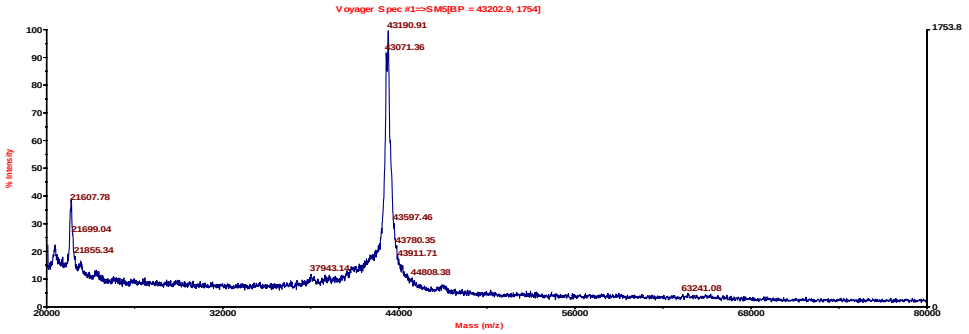

Figure A.2.2. MALDI spectra of the mutant protein. Spectra were collected on labeled and unlabeled Rca preparations, and compared to their theoretical values. (A) Labeled protein preparation. (B) Unlabeled protein spectra preparation. The error of the instrument is estimated to be about 100 Da for a protein of this size.

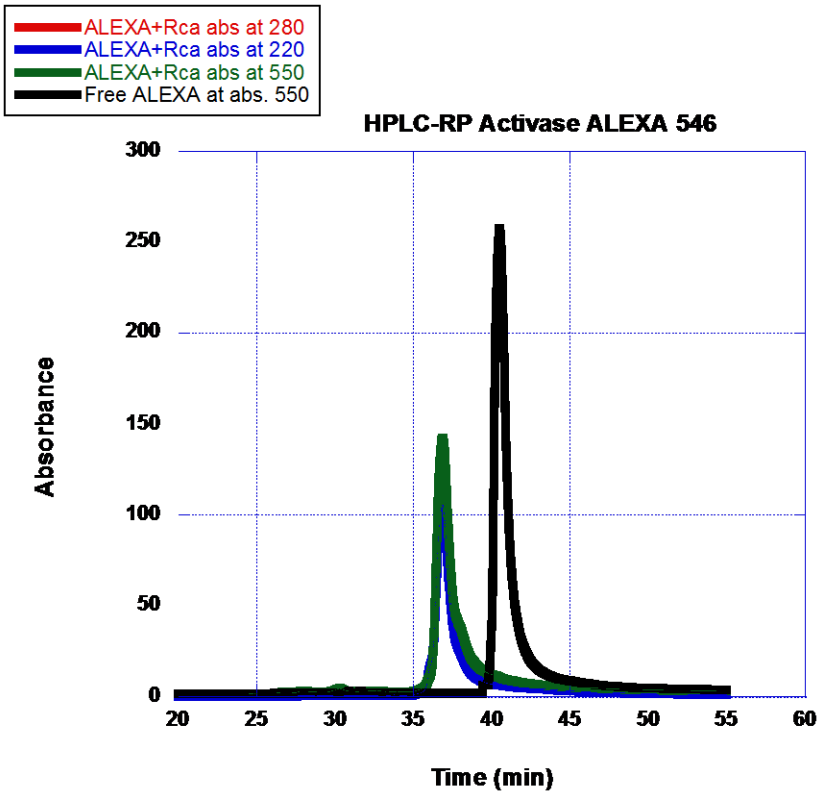

Figure A.2.3. HPLC Chromatograms of the Mutant Protein. Reverse-phase HPLC chromatograms of Alexa-labeled Rca monitored at 280 nm (red), at 220 nm (blue), at 550 nm (green), and free Alexa dye (black). The chromatograms indicate that labeled Rca preparations do not contain any free Alexa dye.

D173N is Still Monomeric Despite of the Lower Diffusion Coefficient Measured at 50nm Concentration

The average molecular brightness can be approximated by dividing the average intensity by the average number of particles in the excitation volume ($I/\langle N \rangle$). The average molecular brightness is also a measure of the oligomeric state of the protein (see chapter 2). A comparison of the molecular brightness values between wt and the mutant protein at the same concentration (50 nM) shows that the average oligomeric size of the mutant protein is same as wt protein. Since, the wt protein is monomeric at 50 nM (see fig. A.1.2), the mutant Rca is also monomeric at 50nM concentration.

Table A.2.1: Number Intensity Comparison between wt and the Mutant Rca. The number of molecules obtained from the amplitude of the FCS curves for both the mutant and the wt protein and the average fluorescence intensity for 50nM protein solutions are given in the table below.

Sample	$\langle N \rangle$	Intensity (I)	$I/\langle N \rangle$
WT Rca in ADP	76	118	1.55
D173N Rca in ADP	71	117	1.64
WT Rca in ADP	45	37	0.08
D173N Rca in ADP	83	59	0.071
WT Rca in ADP	32	100	3.22
D173N Rca in ADP	28	95	3.39

Calculation of Free Mg^{2+} as a Function of the Total Mg^{2+} in the Buffer

K_d ADP binding to Mg^{2+} = 0.241 mM

K_d ATP binding to Mg^{2+} = 0.028 mM

Five equilibria reactions were considered to calculate the free Mg^{2+}, ADP-Mg^{2+}, and ATP-Mg^{2+} concentrations.

$$[Mg^{2+}]_{total} = [Mg^{2+}]_{free} + [ADP\text{-}Mg^{2+}] + [ATP\text{-}Mg^{2+}] \quad \text{Eq. A.2.1}$$

$$[ADP]_{total} = [ADP]_{free} + [ADP\text{-}Mg^{2+}] \quad \text{Eq. A.2.2}$$

$$[ATP]_{total} = [ATP]_{free} + [ATP\text{-}Mg^{2+}] \quad \text{Eq. A.2.3}$$

$$K_{d,\,ADP} = ([ADP]_{free}\ [Mg^{2+}]_{free})/\ [ADP\text{-}Mg^{2+}] \quad \text{Eq. A.2.4}$$

$$K_{d,\,ATP} = ([ATP]_{free}\ [Mg^{2+}]_{free})/\ [ATP\text{-}Mg^{2+}] \quad \text{Eq. A.2.5}$$

Where, the free and total concentration of each species is denoted as subscripts. We solved this system of equations for with known values of $[ADP]_{total}$ = 0.5 mM, and $[ATP]_{total}$ = 1.5 mM, and different $[Mg^{2+}]_{total}$ concentrations to obtain a set of $[Mg^{2+}]_{free}$ values. The result is plotted in fig. A.2.4

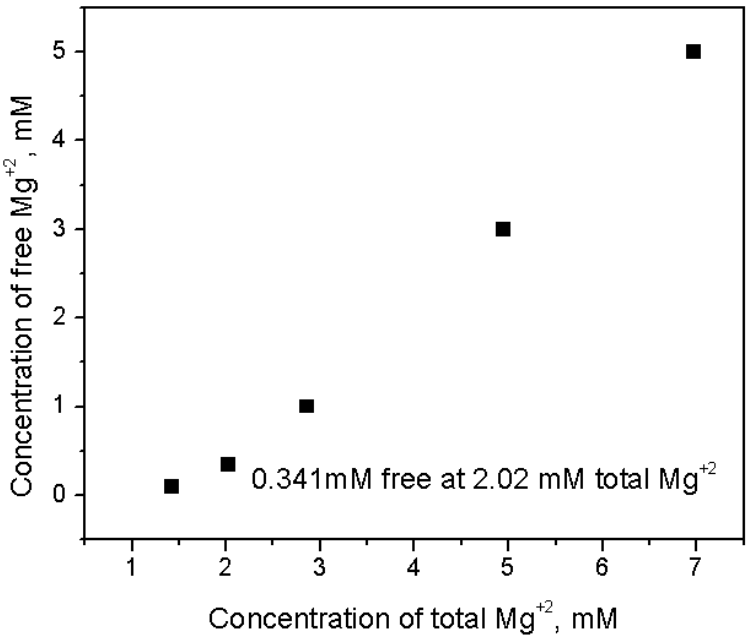

Figure A.2.4. Calculated Free Mg^{2+} Concentration vs. Total Mg^{2+} Concentration Plot.

Estimation of Error in the Calculated Dissociation Coefficients

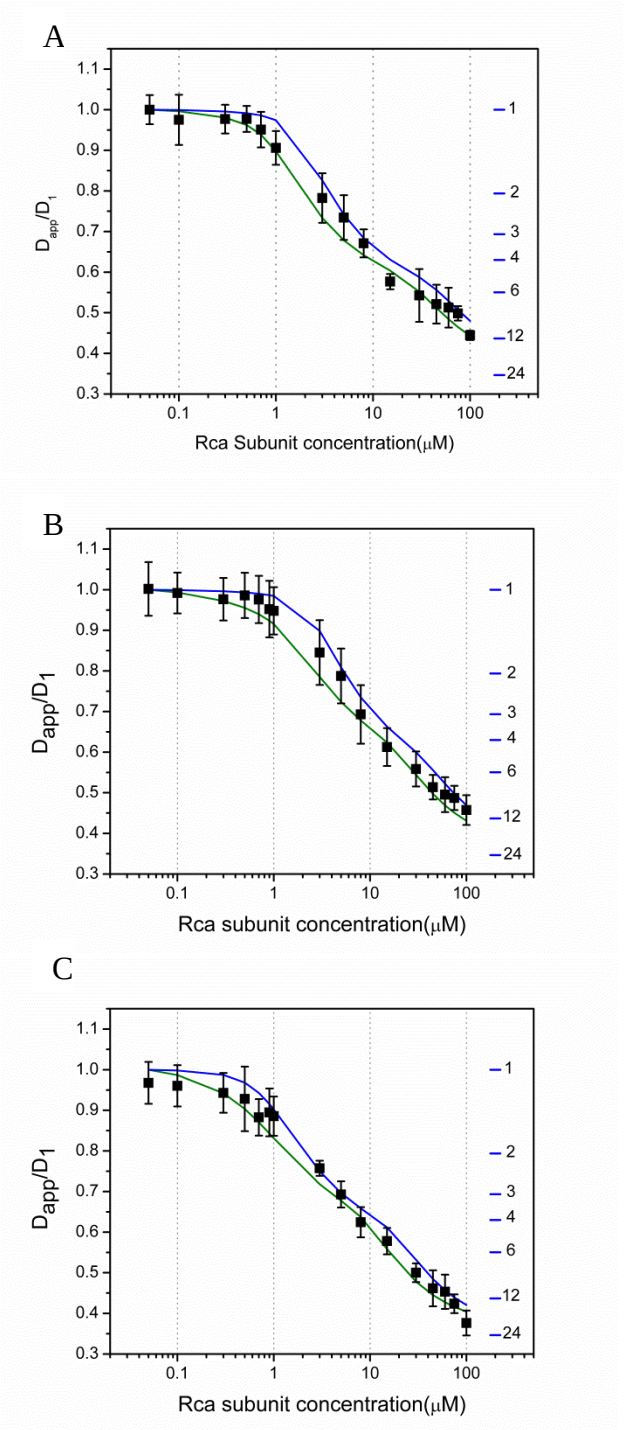

Blue line: (K_{d1} = 25μM, K_{d2} = 0.5 μM, K_{d3} = 0.05 μM, and K_{d4} = 5000 μM^3)
Green line: (K_{d1} = 5 μM, K_{d2} = 1 μM, K_{d3} = 0.08 μM, and K_{d4} = 1000 μM^3

Blue line: (K_{d1} = 30μM, K_{d2} = 1 μM, K_{d3} = 0.01 μM, and K_{d4} = 2000 μM^3)
Green line: (K_{d1} = 2.5 μM, K_{d2} = 5 μM, K_{d3} = 0.2 μM, and K_{d4} = 250 μM^3

Blue line: (K_{d1} = 15μM, K_{d2} = 0.05 μM, K_{d3} = 0.5 μM, and K_{d4} = 8 μM^3)
Green line: (K_{d1} = 1 μM, K_{d2} = 0.8 μM, K_{d3} = 0.5 μM, and K_{d4} = 10 μM^3

Figure A.2.5. Estimation of Error in the Calculated Dissocation Coefficients. The estimated a range of K_d values that describes our experimental within the error bars. The black squares are the experimental data for D173N Rca in presence of (A) 2 mM ATP-5

mM Mg^{2+} (B) 1.5 mM ATP, 0.5 mM ADP-5 mM Mg^{2+}, and (C) 1.5 mM ATP, 0.5 mM ADP-2.02 mM Mg^{2+}. The upper (blue line) and the lower (green line) bounds of K_d values that describe the data within experimental error are given in boxes to the right of each panel.

References:

1. Perrin, F. 1934. The Brownian movement of an ellipsoid. - The dielectric dispersion of ellipsoidal molecules. J Phys-Paris 5:497-511.

2. Stotz, M., O. Mueller-Cajar, S. Ciniawsky, P. Wendler, F. U. Hartl, A. Bracher, and M. Hayer-Hartl. 2011. Structure of green-type Rubisco activase from tobacco. Nat Struct Mol Biol 18:1366-1370.

3. Squire, P. G., and M. E. Himmel. 1979. Hydrodynamics and Protein Hydration. Arch. Biochem. Biophys. 196:165-177.

4. Meseth, U., T. Wohland, R. Rigler, and H. Vogel. 1999. Resolution of fluorescence correlation measurements. Biophys J 76:1619-1631.

PUBLICATIONS

1. **Chakraborty, M**., Kuriata, A.M., Henderson, J.N., Salvucci, M.E., Wachter, R.M. and Levitus, M. "Protein Oligomerization Monitored by Fluorescence Fluctuation Spectroscopy: Self-Assembly of RuBisCO Activase". *Biophys. J. 2012. 103, 949-958. Featured as New and Notable*

2. Kuriata, A.M., **Chakraborty, M**[*]., Henderson, J.N., Salvucci, M.E., Wachter, R.M. and Levitus, M. "The Nucleotide dependent change in the self-association pathway of RubisCO Activase investigated using Fluorescence Correlation Spectroscopy". *Manuscript in preparation, [*]equal contribution as the first author*

3. Binder, J.K., Douma, L., Ranjit, S., Kanno, D., **Chakraborty, M**., Bloom, and L., Levitus, M."Intrinsic stability and oligomerization dynamics of DNA processivity clamps" *Nucl. Acids Res.* (*2014*) *accepted.*